School of Molecular and Life Sciences

Harnessing Direct Current Triboelectricity with Dynamic Schottky Diodes on Silicon

Stuart Paul Ferrie
0000-0001-8988-8293

This thesis is presented for the Degree of
Doctor of Philosophy
of
Curtin University

July 2022

Declaration

To the best of my knowledge I declare that this thesis is my own account of my research and this thesis contains no materials previously published by any other person except where due acknowledgement has been made.

This thesis contains as its main content work which has not previously been submitted for a degree or diploma at any university.

Stuart Paul Ferrie

Date: 5/7/2022

Abstract

Triboelectric nanogenerators (TENGs) are promising emerging power sources with applications from power generation to sensors to as yet emerging technologies like electroculture of plants. This thesis focuses on moving Schottky diode-based TENGs examined by atomic force microscopy (AFM) with modified silicon surfaces. A range of pertinent topics are examined herewith including pyramidally textured surfaces and a range of monolayer-modified surfaces for their applications in TENGs and the presence of copper contamination in these synthesised monolayers.

Pyramidally textured surfaces were studied for their effects on the zero-bias tribocurrent output of a Pt–Si moving Schottky diode by AFM. The pyramids were faceted with Si(111) compared to the Si(100) of the surface surrounding them, ensuring both electrical and topographical contrast. This contrast showed an enhancement of the zero-bias tribocurrent at the boundaries between Si(111) and Si(100) on the Si(111) side. This was attributed to a thinning of the space charge layer due to the concave nature of these boundaries. The largest zero-bias tribocurrents were seen on float zone process lowly doped N-type silicon followed by Czochralski process lowly doped N-type silicon, due to an increase in diffusion length and minority carrier lifetime on float zone process silicon. Minimal currents were observed on highly doped N-type and lowly doped P-type surfaces, agreeing with the mechanism of electron–hole separation and subsequent holes tunneling under the barrier. A size effect of the pyramids was also seen with large pyramids providing higher zero-bias tribocurrents on their edges. This work provides an avenue towards further miniaturisation of these moving Schottky diodes by localising the current to reproducible sites.

To study the effects of organic monolayers and silicon doping on the zero-bias tribocurrent output and friction on TENGs, a set of monolayers to modify silicon were chosen to study with Pt–Si moving Schottky diodes by AFM. Monolayers were prepared by hydrosilylation of hydrogen-terminated Si(111) with 1,8-nonadiyne which was followed by attachment of a series of azides (1-azidobutane, 3-azidopropan-1-ol and 3-azidopropan-1-amine) by a CuAAC reaction to form a 1,2,3-triazole-containing monolayer. These monolayers were studied with x-ray photoelectron spectroscopy (XPS), x-ray reflectometry, cyclic voltammetry and contact angle measurements. These techniques showed expected behaviour of the monolayers and minimal differences between the monolayers on differently doped silicon. Cu contamination was also observed by XPS with much greater surface concentrations of Cu on P-type compared to N-type. Large differences were seen in the friction and zero-bias tribocurrent outputs when studied by conductive AFM with a Pt tip. The measured friction and current were much greater on lowly doped N-type than lowly doped P-type. This suggests an electronic component to the friction in Pt–Si moving Schottky diodes. This effect was magnified on the triazole-containing monolayers. The largest currents were measured on the surfaces with the highest friction coefficients. This work reveals that there is a significant contribution of doping of the underlying silicon on the measured friction of moving Pt–Si Schottky diodes. It also reveals that the backbone of a monolayer can be non-innocent in this electronic component to friction.

As copper contamination had been observed by XPS, a study of the detection of copper by electrochemical methods was attempted. Similar monolayers to previously studied were synthesised, with a focus on those derived from 3-azidopropan-1-amine, as this was seen to trap the most copper by XPS and azidomethylferrocene, which contained a well-characterised redox probe. These surfaces were studied by cyclic voltammetry, electrochemical impedance spectroscopy and open circuit potentiometry. Cyclic voltammetry revealed the presence of copper to vary considerably between surfaces with the same method of preparation, however greater copper was seen on P-type silicon compared to N-type silicon. Electrochemical impedance spectroscopy showed very fast kinetics of electron transfer on P-type silicon compared to N-type. Open circuit potentiometry could not be correlated with the presence of copper in these monolayers, however these monolayers were seen to effectively protect the surfaces from oxidation in all cases.

Acknowledgements

A PhD is a like a marathon. No one gets through the experience alone and there's many people who've helped along the way who I'd like to dearly thank.

I'd like to firstly thank my primary supervisor, Simone Ciampi. Your expertise and support have been invaluable throughout the entire experience. I've really enjoyed working with you and exploring what we can do with silicon that hasn't been explored by anyone before. Our chats have always been valuable to me. I would especially like to thank you for the financial support towards the end of my PhD.

I'd like to thank my co-supervisor, Nadim Darwish. I've enjoyed our time together and again your support and expertise have been invaluable. This whole thesis wouldn't have happened had the research of Malika and you not turned up some unexpected current on a little pyramid.

Another person I must thank is Thomas Becker, who's always been helpful when I've had issues with the AFMs and helped fix some of my accidents in the AFM lab.

I couldn't have done my PhD without the assistance from the Australian Government in the form of the Research Training Program Scholarship.

To my all present and former group members: Yan Vogel, Song Zhang, Jinyang Zhang, Mattia Belotti, Xin Lyu, Harry Morris Rodriguez, Carlos Hurtado Torres, Malika Peiris, Essam Dief, Soraya Rahpeima, Tiexin Li, Luke Bignell, you've been amazing colleagues and I've loved working with you. I've really appreciated all time we've shared together and I'm a better chemist and person for it.

I couldn't have completed my thesis without my friends and family outside of my PhD too, especially those who know the trials and tribulations of a PhD: Josephine Forbes, Matthew Bailes, Daniel Beck, Leesa Smith and Madeleine Barrow.

Finally, I'd like to thank my parents for always being there when I've needed them, even when I couldn't get to see them myself due to the border closures.

Copyright Statement

I have obtained permission from the copyright owners to use any third-party copyright material reproduced in the thesis or to use any of my own published work (e.g. journal articles) in which the copyright is held by another party (e.g. publisher, co-author).

Contents

Declaration i

Abstract ii

Acknowledgements iv

Copyright Statement v

List of Figures x

List of Abbreviations xxi

List of Publications xxiii

  First Author Publications xxiii

  Co-Author Publications xxiii

Chapter 1 Introduction 25

  1.1 Silicon 26

    1.1.1 General properties 26

    1.1.2 Silicon in atomic force microscopy 28

    1.1.3 Preparation of silicon surfaces 29

  1.2 Monolayers 31

    1.2.1 Introduction to monolayers 31

    1.2.2 Silane monolayers on silicon 31

    1.2.3 Carbon-based monolayers on silicon 31

    1.2.4 Synthesis of monolayers 32

    1.2.5 Copper in click reaction 33

    1.2.6 Properties of monolayers 34

  1.3 Friction 34

    1.3.1 Introduction to friction 34

    1.3.2 Mechanisms of friction .... **Error! Bookmark not defined.**

    1.3.3 Friction on monolayers 36

  1.4 Triboelectric nanogenerators 37

1.4.1 Introduction to nanogenerators 37

1.4.2 Mechanisms 41

1.5 Thesis Overview..45

Chapter 2 Materials and Methods..47

2.1 Introduction..47

2.2 Materials 48

2.3 Preparation of surfaces..48

2.3.1 Preparation of pyramidally microtextured silicon surfaces 48

2.3.2 Preparation of azide-modified silicon surfaces for AFM 49

2.3.3 Preparation of azide-modified silicon surfaces for electrochemistry 49

2.4 AFM experiments 50

2.4.1 PF-TUNA for pyramids..50

2.4.2 TUNA LFM for azide modified surfaces..50

2.5 Electrochemical Measurements 51

2.6 Contact angle measurements..52

2.7 X-ray reflectometry..52

2.8 X-ray photoelectron spectroscopy for C, Si, N and O 53

2.9 X-ray photoelectron spectroscopy for Cu..53

Chapter 3 Harnessing silicon facet-dependent conductivity to enhance the direct-current produced by a sliding Schottky diode triboelectric nanogenerator..54

Abstract..55

Graphical Abstract 55

3.1 Introduction..56

3.2 Results and discussion 57

3.3 Conclusion 71

3.4 Acknowledgements..71

Chapter 4 Sliding Silicon-based Schottky diodes: Maximizing Triboelectricity with Surface Chemistry..72

Abstract 73
4.1 Introduction 74
4.2 Results and discussion 76
4.2.1 Surface preparation and characterization 76
4.2.2 Tribocurrent and friction 88
4.3 Conclusions 97
4.4 Acknowledgements 97
Chapter 5 Electrochemical Investigation of Copper in CuAAC Assembled Monolayers 98
Abstract 98
5.1 Introduction 99
5.2 Synthesis of Clicked Monolayers 100
5.3 Cyclic Voltametric Studies of the Prepared Monolayers 100
5.4 Electrochemical Impedance Spectroscopy 107
5.5 Open Circuit Potentiometry 111
5.6 Conclusions 112
Chapter 6 References 116
Appendix A. Attribution statement for “Harnessing silicon facet-dependent conductivity to enhance the direct-current produced by a sliding Schottky diode triboelectric nanogenerator” 129
Appendix B. Attribution statement for “Sliding Silicon-based Schottky diodes: Maximizing Triboelectricity with Surface Chemistry” 130
Chapter 7 Appendix C: Copyright Permissions 131
Figure 1.1 131
Figure 1.2 131
Figure 1.3 132
Figure 1.4 133
Figure 1.7 134
Figure 1.8 135

Figure 1.9 136

Figure 1.10 137

Figure 1.11 141

Figure 1.12 142

Figure 1.13 143

Chapter 3 143

Chapter 4 143

List of Figures

Figure 1.1: Schematic of the crystal structure of silicon. Reproduced under Creative Commons Attribution 3.0 International License from [3] 26

Figure 1.2: Current-voltage curves and SEM images of tungsten probes contacting various facets of a silicon wafer. a) Contacting 100 and 110 facets. b) contacting 112 and 111 facets. c) contacting 111 and 110 facets. d) contacting 110 and 112 facets. Used with permission from [7]. Copyright 2017, Wiley. 28

Figure 1.3: Effects of flexoelectricity by varying the applied tip force on the current-voltage response curve of a Schottky diode formed in AFM. Fitted curves are fitted to classical thermionic emission theory. Used with permission from [13]. Copyright 2021, Elsevier. 29

Figure 1.4: Si(100) surface after 10 s of etching in 40% NH_4F solution after oxide was removed with HF. a) SEM image of flat regions with protuberances. b) Cut along of the line indicated by the two arrows in a). Used with permission from [18]. Copyright 1993, Elsevier. 30

Figure 1.5: Schematic showing the synthesis of monolayers by hydrosilylation on hydride-terminated silicon using a) alkynes and b) alkenes. 32

Figure 1.6: Schematic of the CuAAC reaction 33

Figure 1.7: A) A schematic of the AFM experiment, showing the p-type stripes embedded in n-type silicon. B) Plot of the friction force on each region at +4 V applied bias, showing excess friction on the p-type regions. Inset shows the lack of difference of the adhesion force between the two regions as a function of sample bias. From [54]. Reproduced with permission from AAAS..36

Figure 1.8: Structure and mechanism of polymer-based TENG. a) Structure and current response of a PET-Kapton TENG. b) Mechanism of this polymer-based TENG. Charges are generated at the interface between the two polymer layers by friction, which induces charges in the metallic electrodes which then neutralise and the polymer layers recover, enabling the cycle to begin again. Used with permission from [61]. Copyright 2012, Elsevier B.V. 38

Figure 1.9: a) Topography image from AFM showing three labeled grains of MoS_2. b) Current image from AFM of same region as a), showing a difference in tribocurrent between grains.. c) Current along lines 1 and 2 as shown in b). d-f) I-V curves on each region in a), highlighting the different electrical behaviour between grains. g-i) Equivalent circuits of tip-grain contact corresponding to the grains in a), where C is the capacitance of the depletion region, R_s is the resistance of the surface and D is the Schottky diode. Used with permission from [71]. Copyright 2017, Springer Nature..39

Figure 1.10: Effects of doping and Fermi pinning on TENG output. a) Open circuit voltage output of different dopings of silicon. b) Experimentally and theoretically determined surface potential differences showing Fermi level pinning. c) Removal of surface oxide using HF. d) Open circuit voltage output after HF etching after 10 minutes (removal off oxide) and 21 hours (restoration of oxide layer), demonstrating the inversion of sign due to reduction of Fermi level pinning. e) Energy band diagram of the metal–silicon contact before HF etching. f) Energy band diagram of the same contact after HF etching. Used with permission from [74]. Copyright 2019, Royal Society of Chemistry 40

Figure 1.11: Tribocurrent between Pt and Si with different dopings. a) I-V curve on P-type silicon with band diagram showing the band bending. b) I-V curve on N-type silicon with band diagram. c) Tribocurrent on non-etched surfaces with different dopings. d) Tribocurrent on reactive ion etched surfaces, showing an enhancement in current. Used with permission from [80]. Copyright 2020, Wiley 42

Figure 1.12: Water-silicon TENG. a) Schematic of the experiment, showing the water-silicon TENG. b) Voltage response the motion of the TENG. c) Energy band diagram showing band structure of when water is in contact with the silicon. d) Energy band diagram showing excitation of electron-hole pair. Used with permission from [81]. Copyright 2020, Elsevier. 43

Figure 1.13: Depletion layer establishment and destruction mechanism. a) Quasi-static finite element simulation model structure and physical process. b) Output current along bottom surface with time. c) Electron concentration with time with arrows showing the direction of the current. d) Distribution of the band and Fermi level energies along the A1-B1 line in c). e) Distribution of the band and Fermi level energies along the A2-B2 line in c) Reproduced under Creative Commons Attribution 4.0 International License from [84]. 44

Figure 1.14: Summary of TENG mechanisms. a) Polymer based TENGs, which generate AC based on static charging of surfaces, b) Diode based TENGs which generate DC based on separation of electron-hole pairs, c) Graphite based TENGs which generate DC based on depletion layer establishment and destruction. 45

Figure 3.1: Facet-dependent rectification and zero-bias d.c. currents in an out-of-equilibrium Pt–Si diode. a) 12 × 12 µm AFM topographic (height) map of pyramids protruding from flat lowly doped float zone (FZ) n-type Si(100). b) Height profile along the red dotted line shown in (a). c) Schematic of the AFM experiment, with the platinum tip contacting a monolayer coated oxide-free silicon surface. The blue and red arrow indicate the trace (left to right) and retrace direction (right to left), respectively. d) Peak force error map for the retrace direction, showing the actual variation with respect to the 2 µN set-point in the normal force across the sample. e) Zero-bias (0 V) tunneling AFM (TUNA) current profiles for scans along the trace (blue) and retrace (red) directions over the dotted red line shown in both (a) and (d). f) Values of “leakage” reverse-bias (+0.125 V) current, obtained from static current–potential (I–V) curves sampled at 200 evenly spaced points (58.6 nm spacing) along the red dotted line shown in (a). g) Schematic of the sample to tip bias routing and representative I–V curves sampled at point **1** on Si(100), close to the (100)/(111) boundary at point **2** on Si(111), and at point **3** on Si(111) but further away from the (100)/(111) boundary. Forward currents appear in the negative quadrant, that is, when the Si is biased negative with respect to the tip. Leakage currents are generally lower at the pyramid base, while rectification ratios (not shown) do not track the pyramid profile as forward currents are generally very disperse. Scale bars in (a) and (d) are 2 µm....58

Figure 3.2: SEM imaging of a Si(100) surface with protruding Si(111) pyramids. The substrate is n-type (phosphorus-doped) FZ Si(100) of 8–12 **Ω** cm resistivity. SEM images were recorded using a Zeiss Neon 40EsB FESEM equipped with a Schottky field emission gun operating at 5 kV and a chamber pressure of approximately 4 × 10^{-6} mbar. 58

Figure 3.3: No visible wear tracks. AFM topography (height image) data acquired within one side of a Si(111) pyramid etched on a Si(100) wafer (CZ substrate, 8–12 **Ω** cm, n-type, phosphorus-doped). Data recorded in tapping mode using TESPA-V2 tips after prolonged tribocharging measurements (10 scans in PF-TUNA mode at a Peak Force set-point of 2.000 µN, with line spacing of 58.6 nm). The height image was acquired at a scanning rate of 0.996 Hz. The scale bar is 200 nm and no wear tracks are visible at this scale. Unless otherwise specified, all samples of this study are monolayer-coated (1,8-nonadiyne) hydride-terminated silicon surfaces....60

Figure 3.4: Sustained zero-bias d.c. output after repeated sliding experiments. On the time scale of these experiments, the decline in tribocurrents is negligible. Repeated zero-bias current imaging of Pt–Si sliding diodes on Si(100) substrates (CZ wafers, 8–12 **Ω** cm in resistivity, n-type, phosphorus-doped) etched to expose Si(111) pyramids. a) Height sensor image. b) TUNA current map after 1 scan. c) TUNA current map after six scans. The Peak Force set-point is 2.000 µN, the scan rate 0.894 Hz, and scale bars are 5 µm. Imaging is in PF-TUNA mode ..60

Figure 3.5: Average Peak current (black) and maximum Peak Current (blue) continuously imaged on the same area over a 18h period on a Si(111) pyramid prepared on lowly doped (8–12 **Ω** cm) n-type FZ (100) silicon with a Ga/In eutectic on copper tape back contact with 15 × 15 µm area with 256 sampling points per line over 256 horizontal lines. 61

Figure 3.6: Normal force and current. (a) Topography image of Si(111) pyramids prepared on lowly doped (8–12 Ω cm) n-type FZ (100) silicon with a carbon tape back contact. (b-f) Current images at a scan rate of 20 µm/s. These images are in order of scanning, rather than order of applied force. Peak Force setpoint of (b) 2.0 µN (c) 1.0 µN, (d) 0.5 µN, (e) 1.5 µN and (f) 2.5 µN. Scale bars are 4 µm for all images. g) Graph showing Peak Force setpoint versus average TUNA current across the image and the contact area as calculated by the DMT model as in Section S1. Points are numbered in the order they were imaged. 62

Figure 3.7: Zero-bias current output from sliding diodes on small pyramids. Si(100) CZ samples (8–12 Ω cm resistivity, n-type) etched for 60 min etch in potassium hydroxide solutions, without any isopropyl alcohol, to generate small Si(111) pyramids. The Peak Force set-point is 0.5482 µN, the scan rate 1.00 Hz, and scale bars are 100 nm. Images acquired in PF-TUNA mode. a) Height sensor image. b) TUNA current image. 63

Figure 3.8: Negligible d.c. output from sliding Pt–Si diodes on flat surfaces. a,b) Si(100), and c,d) Si(111) surfaces (CZ phosphorus-doped wafers, 8–12 Ω cm). All surfaces are monolayer-protected but non-structured, that is, prepared without the KOH and second NH_4F etches. The Peak Force set-point is 2.000 µN, the scan rate 0.988 Hz, and scale bars are 2 µm. Samples are imaged in PF-TUNA mode. a,c) Height sensor images. b,d) TUNA current images. 64

Figure 3.9: High-speed capture current data. The current peaks while the Pt AFM tip is contact with the silicon surface while there is only a small dielectric breakdown between the surface and tip immediately after the tip has left contact with the surface. The TUNA current is the average of the raw current over each tip contact cycle. AFM data acquired on FZ n-type Si(100) samples (8–12 Ω cm). Peak Force set-point was set to 2.000 µN, the scan rate to 0.894 Hz, and the deflection error and raw current are sampled at 500 kHz over two cycles of tip–surface contact. 64

Figure 3.10: Conductive lateral force microscopy. Contact mode conductive AFM with the sample scan angle set to 90° for all images to obtain friction data. Samples are CZ Si(111) wafers, p-type (boron), 8–12 Ω cm. The deflection set-point was set to 400 nN for all images. Scale bars are 1 µm. a–c) 3-azidopropan-1-amine treated (click reaction) surfaces, showing increased friction and decreased current versus (d–f) 1,8-nonadiyne surfaces. a,d) Height sensor images. b,e) TUNA current images. c,f) Friction loop (retrace image minus trace image then divided by a factor of two. The difference in the lateral forces in the retrace versus the trace image corresponds to twice the friction force). 66

Figure 3.11: Joined pyramids showing no enhancement of current at Si(111)–Si(111) junctions. Zero-bias current imaging of Pt–Si sliding diodes on Si(100) substrates (FZ wafers, 8–12 Ω cm in resistivity, n-type (phosphorus-doped)) etched to expose Si(111) pyramids. a) Height sensor image. b) TUNA current map in trace direction (left to right). c) TUNA current map in retrace direction (right to left). The Peak Force set-point was set to 2.000 µN, the scan rate is 0.894 Hz, and scale bars are 2 µm. Imaging is in PF-TUNA mode. 67

Figure 3.12: Zero-bias current increases with the minority carriers' mobility. Current output from sliding Schottky diodes (Pt–Si) on lowly doped (8–12 Ω cm) CZ (a–c) and FZ (d–f) n-type silicon. a,d) 12 × 12 µm AFM electrical data (TUNA retrace maps) showing higher currents close to the (100)–(111) boundary. b,e) Current–potential (I–V) curves acquired either on planes of Si(100) (black trace), on the Si(111) pyramid where low current is observed (red), and on the Si(111) pyramid where high current is observed (blue). Lines indicate the mean current from I–V curves recorded at ten sampling points, with each location sampled five times (from positive to negative) with the shaded area corresponding to one standard deviation. c, f) Histograms showing the relative frequency of the current value in the TUNA current image. Scale bars in (a) and (d) are 2.0 µm. 68

Figure 3.13: Doping and zero-bias output. Current output from sliding Schottky diodes (Pt–Si) on lowly doped (8–12 Ω cm) CZ p-type (a–c), and on highly doped (0.007–0.013 Ω cm) CZ n-type (d–f) silicon. a,d) 12 × 12 µm AFM electrical data (TUNA retrace maps) showing higher currents close to the (100)–(111) boundary. b,e) I–V curves acquired either on planes of Si(100) (black trace) and on the Si(111) pyramid (red). Lines indicate the mean current from I–V curves recorded at ten sampling points, with each location sampled five times from positive to negative with the shaded area corresponding to one standard deviation. c,f) Histograms showing the relative frequency of the current value in the TUNA current image. Scale bars in (a) and (d) are 2.0 µm. 69

Figure 3.14: Pyramid size and zero-bias current magnitude and localization. (a–d) Topography images of Si(111) pyramids of various sizes prepared on lowly doped (8–12 Ω cm) n-type FZ (100) silicon. The width from top edge to bottom edge is displayed for each pyramid. (e–h) Current images (retrace TUNA current) showing localization of the d.c. current maxima at the pyramids' edges. Such localization is less appreciable in the smaller pyramids (h). Scale bars are 3.0 µm. 70

Figure 3.15: Peak Current (current when the tip contact force is highest) trace showing a maximal current of 30.6 nA on Si(100) FZ wafers, 8–12 Ω cm in resistivity, n-type (phosphorus-doped) etched to expose Si(111) pyramids. Back contact is with a gallium/indium eutectic on copper tape..71

Figure 4.1: Silicon surface preparation. Schematics of the surface functionalization strategy. Native oxide is first cleaned and etched (1,2) to form a hydrogen-terminated surface. This surface is reacted under UV with 1,8-nonadiyne to form surface **S1**. The terminal acetylene functionality of **S1** is reacted through a CuAAC reaction to covalently attach either 3-azidopropan-1-amine (forming **S2-NH$_2$**), 3-azidopropan-1-ol (**S2-OH**), or 1-azidobutane (**S2-CH$_3$**). 76

Figure 4.2: Mechanism for the attachment of 1,8-nonadiyne to SiH surface [36]. A hydrogen atom is removed from the Si surface, which is followed by attachment of 1,8-nonadiyne to the surface by a radical hydrosilylation. The formed C-centred radical then abstracts a hydrogen atom from a neighbouring Si atom, which then further reacts with 1,8-nonadiyne by the same mechanism. 76

Figure 4.3: Mechanism of CuAAC reaction [155]. A Cu(1) complex coordinates to the terminal alkyne of the monolayer. This then further reacts with another equivalent of the Cu(I) complex which replaces the hydrogen of the terminal alkyne. The azide then coordinates to the Cu(I) complex which is coordinated to the alkyne by the π-system. This complex then rearranges to form a six-membered ring with the nitrogen coordinating to the two Cu(I) complexes. This eliminates one equivalent of the Cu(I) complex forming the 1,2,3-triazole. The final Cu(I) complex is replaced by hydrogen in the final step. 77

Figure 4.4: X-ray reflectometry (XRR) profiles of a) **S1**, b) **S2-NH$_2$**, c) **S2-OH**, and d) **S2-CH$_3$** surfaces made on N-type silicon substrates. The points with error bars are the collected data and the solid lines are the fits to a monolayer model defined by its thickness (d), scattering length density (SLD), and roughness. The refined structural parameters were: **S1**, d = 10.38 (4.52) Å, SLD = 1.05 × 10^{-5} Å^{-2}; **S2-NH$_2$**, d = 14.41 (0.24) Å, SLD = 1.21 × 10^{-5} Å^{-2}; **S2-OH**, d = 12.23 (0.19) Å, SLD = 1.35 × 10^{-5} Å^{-2}; **2-CH$_3$**, d = 12.12 (0.19) Å, SLD = 1.27 × 10^{-5} Å^{-2}. Estimated standard deviations (esd's) are given in parentheses. SLD for X-rays are equal to the material electron density (e$^-$/Å^3) multiplied by 2.82 × 10^{-5} Å. The refined electron densities obtained for these surface (~0.4 e$^-$/Å^3) are higher than the average 0.31 e$^-$/Å^{3}reported for a series of methyl-terminated monolayers prepared on Si(100) from 1-alkynes [157], reinforcing on the compactness of the organic monolayers used in this study. 78

Figure 4.5: Silicon surface characterization. (a) Water contact angle measurements, showing minimal influence of substrate doping on wettability within samples of same surface chemistry. (b) High-resolution X-ray photoelectron spectroscopy of the Si 2p narrow region, showing minimal formation of silicon oxides. (c) Plot of the anodic (positive values) and cathodic (negative values) current peak heights obtained from cyclic voltammograms of ferrocene-terminated monolayers. Current data indicate a comparable ferrocene surface coverage, hence CuAAC yield, in both P- and N-type silicon. (d) Work function of the chemically passivated surfaces measured by ultraviolet photoelectron spectroscopy. 79

Figure 4.6: XPS wide scans of a) **S1** samples prepared on N-type silicon (C/Si ratio = 0.496), b) **S1** samples prepared on P-type silicon (C/Si ratio = 0.489), c) **S2-NH$_2$** samples prepared on N-type silicon (C/Si ratio = 0.871), d) **S2-NH$_2$** samples prepared on P-type silicon (C/Si ratio = 1.071), e) **S2-OH** samples prepared on N-type silicon (C/Si ratio = 0.623), f) **S2-OH** samples prepared on P-type silicon (C/Si ratio = 0.714), g) **S2-CH$_3$** sampled prepared on N-type silicon (C/Si ratio = 0.615), and h) **S2-CH$_3$** samples prepared on P-type silicon (C/Si ratio = 0.699). All wide scans showed expected emissions in agreement with the expected Si and C presence (all surfaces) and N (only for **S2** surfaces). Peaks corresponding to Cu emission at 933 eV were observed on N-type **S2-NH$_2$**, P-type **S2-NH$_2$**, P-type **S2-OH** and P-type **S2-CH$_3$**. 81

Figure 4.7: XPS narrow scans of the C 1s region of a) N-type S1, b) P-type S1, c) N-type S2-NH2, d) P-type S2-NH2, e) N-type S2-OH, f) P-type S2-OH, g) N-type S2-CH3 and h) P-type S2-CH3 samples. For S1 surfaces, three mixed Gaussian–Lorentzian (80% Gaussian and 20% Lorentzian) functions were required to fit the experimental C 1s band. These three refined components were centred at 283.5, 284.5 and 285.6 eV corresponding respectively to C–Si (silicon-bound carbons, [164]), C–C (carbon-bound carbons [165]), and carbon in either a C–OH or C≡C bonding configuration for the high energy component [166]. For S2 surfaces, three separate functions were also required fit the experimental C 1s emission. These functions were located at 284.5, 286.1 and 287.9 eV, corresponding to C–C, the C–N/C–O and the C=N carbons, which is consistent with previous reports [85]. 82

Figure 4.8: XPS narrow scans of the Si 2p region of a) N-type **S1**, b) P-type **S1**, c) N-type **S2-NH$_2$**, d) P-type **S2-NH$_2$**, e) N-type **S2-OH**, f) P-type **S2-OH**, g) N-type **S2-CH$_3$** and h) P-type **S2-CH$_3$** samples. For all surfaces, the experimental Si 2p emission was fitted with two mixed Gaussian–Lorentzian (95% Gaussian and 5% Lorentzian) functions centred at 98.8 and 99.4 eV, corresponding respectively to the 2p$_{3/2}$ and 2p$_{1/2}$ spin–orbit-split components, and having a FWHM of 0.5 eV. This assignment is in line with previous reports [85]. The silicon 2p scan emission did not show evidence of oxidised silicon on the **S1** surfaces, however a minor high binding energy component located at ca, 102 eV was detected in the **S2** samples and attributed to minor presence of silicon oxides. We attribute this to oxidation during the CuAAC reaction, however silicon oxide was not observed in AFM (e.g. Fig S9), which generally appears as sharp topographic features. 83

Figure 4.9: XPS narrow scans of the N 1s region of a) N-type **S2-NH_2**, b) P-type **S2-NH_2**, c) N-type **S2-OH**, d) P-type **S2-OH**, e) N-type **S2-CH_3** and f) P-type **S2-CH_3** sample. The N 1s experimental signals were fitted with two Gaussian functions centered at 399.7 and 401.3 eV, corresponding to N═N–N and NH_2 (for **S2-NH_2** surfaces) and N═N–N in line with previous reports [85, 167]. As expected from the chemical structure of the azide tethered onto the surface, the two refined contributions were a 2:1 ratio for **S2-OH** and **S2-CH_3** samples, and in a 3:1 ratio for **S2-NH_2** surfaces. No emission corresponding to unreacted (physically adsorbed rather than chemisorbed) azide molecules, expected at 405 eV [168], was seen in any of the spectra. 84

Figure 4.10: Electrochemical measurements of the CuAAC reaction yields (surface coverage). Cyclic voltammograms recorded at a variable voltage sweep rate (indicated by the labels in figure) of ferrocenylated silicon surfaces (chemical details as per Fig. 2c). The silicon surface served as the working electrode, and Ag/AgCl as the reference electrode, and a platinum coil as the counter electrode. The electrolyte was aqueous 1.0 M $HClO_4$. Panel (a) shows data for P-type samples under ambient light, and (b) for N-type samples under red light illumination (660 nm). 85

Figure 4.11: UPS spectra of the secondary edge region of a) N-type **S1**, b) P-type **S1**, c) N-type **S2-NH_2**, d) P-type **S2-NH_2**, e) N-type **S2-OH**, f) P-type **S2-OH**, g) N-type **S2-CH_3** and h) P-type **S2-CH_3** samples. The black line is the acquired data and the red lines are linear fits to the flat and steep regions. The work function of each sample was estimated from the position of the intersection between the flat lines (subtracted from the 21.218 eV excitation energy)..... 87

Figure 4.12: XPS-derived surface copper concentration estimated as percentage of the total photoelectron counts. In general, a small amount of copper was observed on samples prepared on N-type silicon, while a greater amount was observed for P-type surfaces. This trend tracks the change in work function (UPS data, Figure 4.11)... 88

Figure 4.13: AFM experiments. (a) Schematic showing the AFM tip–monolayer–Si sliding contact and the configuration of the electrical circuit for C-AFM. In our C-AFM setup the external voltage bias is applied to the substrate. b) Typical topography data of a monolayer-modified crystalline Si surface (**S2-NH_2**, N-type). (c) Representative zero-bias (0.0 V) current image of a sliding junction (**S2-NH_2**, N-type). (d) Representative friction loop image (friction measured in the trace direction minus the friction measured in the retrace direction, all divided by two to give the friction force; **S2-NH_2**, N-type). (e,f) Current–voltage (I–V) curves acquired on P-type (e) and N-type (f) silicon surfaces bearing different monolayers (each trace is the average of ten I–V curves; labels to the curves specify the monolayer chemistry)................ 90

Figure 4.14: Topography AFM images and roughness values for all surfaces of this study ((a) N-type **S1**; (b) P-type **S1**; (c) N-type **S2-NH$_2$**; (d) P-type **S2-NH$_2$**; (e) N-type **S2-OH**; (f) P-type **S2-OH**; (g) N-type **S2-CH$_3$**; (h) P-type **S2-CH$_3$**). The topography images are height sensor images acquired under an applied force of 50 nN. Analysing data of a 1.8 μm × 200 nm region allows removing edge artifacts. This was the same sampling area on which friction data are also measured. Scale bars are 400 nm. Surface roughness (Ra) values are indicated in figure. 91

Figure 4.15: Nulling voltages as determined from I–V curves, as the external bias at which the current switches sign. These data show a consistently greater (more negative) nulling voltages on N-type over P-type, and indicate a greater effect on nulling voltage mediated by the monolayer chemistry rather than by the doping type of the underneath silicon......................92

Figure 4.16: AFM-derived friction, adhesion and zero-bias current data. (a,b) Friction force versus normal force data for all monolayer systems ((a), N-type silicon; (b) P-type silicon). Data recorded at zero applied bias. c) Adhesion data for all monolayer systems, prepared on either N- or P-type silicon substrates. d) Friction coefficients (μ) for all monolayer systems (N- and P-type silicon substrates). e) Ratio between the friction coefficient of samples with the same monolayer type but grafted on either N- or P-type silicon. Data indicate a significantly larger μ on N-type samples for all **S2** monolayers systems, while the N-/P- ratio of μ was closer to unity for the **S1** monolayer. f) Maximum zero-bias tribocurrent output measured on samples prepared on N-type silicon. Sliding junctions made on P-type silicon did not show a zero-bias current greater than the noise in the measurements (~1 pA). 93

Figure 4.17: X-ray reflectometry (XRR) analysis of the nanoscale water-uptake kinetics on monolayer-modified samples. By unveiling the time scale required for a nanoscale water layer to adsorb, time-resolved XRR experiments allowed to rule out a doping-related effect on water uptake, hence a link between friction and current with surface water layers. The velocity and extent of water accumulation is comparable between P- and N-type samples. (a,b) XRR data showing the accumulation of water on **S1** surfaces, showing no kinetic difference, between samples made on substrates of different doping type, in the water uptake from air ((a) N-type silicon; (b) P-type silicon). The blue XRR profiles are obtained on dry samples (t = 0 h), while the red curves are profiles obtained between 1 and 15 h after exposure of the samples to ambient air. The emergence of a Kiessig fringe indicate nanoscale water accumulation on the surface. This water layer makes the system overall progressively thicker, and the black traces are the final measurements at time t = 15 h. (c) Plot of R/R_0 at $Q = 0.351$ Å^{-1} (where R is reflectivity at a given time and R_0 is reflectivity a t = 0 h) which shows increasing intensity of the Kiessig fringe over time. 95

Figure 5.1: Synthesis of studied monolayers using typical methods to hydrogen-terminate the surface then a hydrosilylation and CuAAC strategy to assemble the monolayers of interest. 100

Figure 5.2: Cyclic voltammogram of highly doped N-type **S1** surface at 100 mV/s scan rate (5 cycles) 101

Figure 5.3: Cyclic voltammogram of lowly doped P-type S3 surface at 100 mV/s scan rate (5 cycles), showing the presence of copper......101

Figure 5.4: Surface concentration as determined from anodic peak of cyclic voltammogram in Figure 5.3 102

Figure 5.5: Cyclic voltammograms of four lowly doped P-type S2 surfaces at a range of scan rate with Cu shoulder peak annotated by an arrow. a) Sample 1, b) sample 2, c) sample 3, d) sample 4 102

Figure 5.6: Cyclic voltammograms of three highly doped P-type S2 surfaces at a range of scan rate with Cu shoulder peak annotated by an arrow. a) Sample 1, b) sample 2, c) sample 3..104

Figure 5.7: Cyclic voltammograms of three lowly doped N-type S2 surfaces at a range of scan rates under illumination. a) Sample 1, b) sample 2, c) sample 3 105

Figure 5.8: Cyclic voltammograms of highly doped N-type S2 surfaces at a range of scan rates. a) Sample 1, b) sample 2, c) sample 3 106

Figure 5.9: Bode plots of S2 surfaces on a) lowly-doped N-type silicon with filled squares for dark EIS and crossed squares for red illuminated EIS, b) lowly-doped P-type silicon, c) highly-doped N-type silicon with filled squares for initial EIS and empty squares for EIS after obtaining cyclic voltammograms, d) highly-doped P-type silicon. 107

Figure 5.10: Model Randles circuit for EIS fitting. R_{sol} is the solution resistance, C_{ads} is the adsorption pseudo-capacitance, R_{ct} is the charge transfer resistance and C_{dl} is the double layer capacitance. 108

Figure 5.11: Mott-Schottky plots at 10 kHz of prepared surfaces (black) with linearly fit and extrapolated region (red) to determine the flat band potential. a) Lowly-doped P-type S1, b) lowly-doped N-type S1, c) lowly-doped P-type S2, d) lowly-doped N-type S2, e) lowly-doped P-type S3, f) lowly doped N-type S3. 109

Figure 5.12: Flat band potential as determined from extrapolation of Mott-Schottky plots .110

Figure 5.13: Open circuit voltages versus Ag/AgCl for a) **S1** surfaces, b) **S2** surfaces and c) **S3** surfaces. 111

List of Abbreviations

AC – alternating current

AFM – atomic force microscopy

CA – contact angle

CZ – Czochralski process

C-AFM – conductive atomic force microscopy

CuAAC – copper azide-alkyne coupling

CV – cyclic voltammetry

DC – direct current

DCM – dichloromethane

DMT – Derjaguin-Muller-Toporov

e-*h* – electron-hole

EIS – electrochemical impedance spectroscopy

fwhm – full width half maximum

FZ – float zone process

HD – highly doped

LD – lowly doped

LFM – lateral force microscopy

M-S – Mott-Schottky

OCP – open circuit potential

PENG – piezoelectric nanogenerator

PET – poly(ethylene terephthalate)

PF-TUNA – Peak Force tunnelling AFM

PPy – polypyrrole

SEM – scanning electron microscopy

TENG – triboelectric nanogenerator

TUNA – tunnelling AFM

TXRF– total x-ray reflection fluorescence

UPS – ultraviolet photoelectron spectroscopy

UV – ultraviolet

XPS – x-ray photoelectron spectroscopy

XRR – x-ray reflectometry

List of Publications

First Author Publications

Ferrie, S.; Darwish, N.; Gooding, J. J.; Ciampi, S., Harnessing silicon facet-dependent conductivity to enhance the direct-current produced by a sliding Schottky diode triboelectric nanogenerator. *Nano Energy* **2020,** *78*, 105210.

Ferrie, S.; Le Brun, A. P.; Krishnan, G.; Andersson, G. G.; Darwish, N.; Ciampi, S., Sliding silicon-based Schottky diodes: Maximizing triboelectricity with surface chemistry. *Nano Energy* **2022,** *93*, 106861.

Co-Author Publications

Zhang, J.; Ferrie, S.; Zhang, S.; Vogel, Y. B.; Peiris, C. R.; Darwish, N.; Ciampi, S., Single-Electrode Electrochemistry: Chemically Engineering Surface Adhesion and Hardness To Maximize Redox Work Extracted from Tribocharged Silicon. *ACS Applied Nano Materials* **2019,** *2* (11), 7230-7236.

Rahpeima, S.; Dief, E. M.; Peiris, C. R.; Ferrie, S.; Duan, A.; Ciampi, S.; Raston, C. L.; Darwish, N., Reduced graphene oxide–silicon interface involving direct Si–O bonding as a conductive and mechanical stable ohmic contact. *Chemical Communications* **2020,** *56* (46), 6209-6212.

Zhang, S.; Ferrie, S.; Lyu, X.; Xia, Y.; Darwish, N.; Wang, Z.; Ciampi, S., Absence of a Relationship between Surface Conductivity and Electrochemical Rates: Redox-Active Monolayers on Si(211), Si(111), and Si(110). *The Journal of Physical Chemistry C* **2021,** *125* (33), 18197-18203.

Zhang, S.; Ferrie, S.; Peiris, C. R.; Lyu, X.; Vogel, Y. B.; Darwish, N.; Ciampi, S., Common Background Signals in Voltammograms of Crystalline Silicon Electrodes are Reversible Silica–Silicon Redox Chemistry at Highly Conductive Surface Sites. *Journal of the American Chemical Society* **2021,** *143* (3), 1267-1272.

Peiris, C. R.; Ferrie, S.; Ciampi, S.; Rickard, W. D. A.; Darwish, N., Memristor Arrays Formed by Reversible Formation and Breakdown of Nanoscale Silica Layers on Si–H Surfaces. *ACS Applied Nano Materials* **2022,** *5* (5), 6609-6617.

Chapter 1 Introduction

The generation of clean power is one of the great challenges for the 21st century. A reliance on fossil fuels is fuelling climate change, so it is imperative that we reduce this reliance. A move away from fossil fuels comes with it challenges. New clean energy sources are needed, especially those that can be miniaturised and decentralised.

The current power grid is built around centralised power stations distributing energy outwards. This distribution is becoming increasingly outmoded with the increase in decentralised solar cells and batteries capable of storing the excess energy from solar power. With an increasing move towards the Internet of Things, we will need further autonomous highly efficient direct current power sources that step away from this grid based system [1].

This need is currently filled by batteries, which require recharging or replacement once the battery has completely discharged and can contain expensive, such as lithium; or toxic, such as cadmium, components. This desire for green energy has expanded the scope of the search for harvestable energy. Solar panels are advantageous where there is sunlight, however this is not always viable in places with lower solar flux or where systems may be completely in the dark. Wind power requires constant winds which makes it unsuitable for many areas. Another further issue with both wind and solar is the inability to miniaturise these systems.

One such promising class of devices are nanogenerators which convert mechanical energy into electrical energy. The first developed variants of these were piezoelectric nanogenerators, which use piezoelectricity to generate current. These however are hampered by low power densities [2]. Triboelectric nanogenerators (TENGs) use triboelectricity: current generated by friction. A particularly promising set of these are those based on junctions with rectifying properties such as Schottky diodes.

Silicon is an ideal material for these Schottky diode-based TENGs, as it is cheap and versatile. The properties of silicon itself are also of interest as it can be modified by selecting an appropriate doping, facet or process to make monocrystalline silicon wafers. Procedures to etch silicon to form pyramidal microstructures are also well characterised and allow access to adjacent (100) and (111) facets, which are of interest due to their contrasting electrical properties.

The surface chemistry of silicon is of particular interest. Unlike many other semiconductors which are III-V or II-IV compounds, silicon is a semiconducting element. One issue with silicon however is the oxidation that occurs on its surface. Silicon oxide is an insulator, so this oxidation can adversely affect the charge transport properties through the surface. Surface chemistry provides us with an avenue to minimise this oxidation with the added benefits of being able to further tune other properties of the surface. Those of interest to triboelectric nanogenerators that can be tuned by surface chemistry include the friction, adhesion and wettability.

In this chapter, section 1 discusses the general properties of silicon with a further discussion of the general preparatory methods used in silicon chemistry. Section 2 discusses organic monolayers on silicon with emphasis on the synthesis and properties of these monolayers. Section 3 discusses friction on monolayers and the relevant mechanisms by which friction occurs on these. Section 4 discusses TENGs in greater detail, particularly of Schottky diode based TENGs. Section 5 is a general overview of the thesis.

1.1 Silicon

1.1.1 General properties

Silicon is one of the most important elements underpinning our current society. Without it, we wouldn’t be able to achieve the rapid pace of the advancement of our technology. Silicon crystallises in a centrosymmetric Fd-3m space group, as shown in Figure 1.1

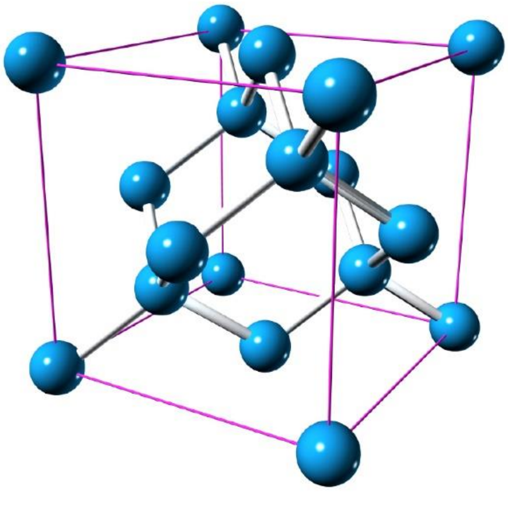

Figure 1.1: Schematic of the crystal structure of silicon. Reproduced under Creative Commons Attribution 3.0 International License from [3]

Monocrystalline silicon as a material is typically obtained in wafers produced by either the Czochralski (CZ) or float-zone (FZ) process. The Czochralski process requires the melting of polycrystalline silicon, into which a seed crystal is placed. Silicon crystallises from the melt on this seed crystal to form a monocrystalline boule of silicon. This large single crystal is then cut into wafers [4].

The float-zone process silicon is substantially more expensive, but comes with the advantage of very low concentrations of oxygen in the crystal itself [5]. The float-zone process requires an already formed polycrystalline silicon ingot, which is then pulled through a series of induction heaters which melt the silicon ingot and reform it into a single crystal. The impurities in the silicon are trapped in the melt, leaving extremely pure silicon at the end [6].

Silicon is rarely used as an intrinsic semiconductor, rather it is doped with small amount of other elements. P-type doping introduces more holes into the silicon, decreasing the electrons in the valence band, which increases the conductivity as more dopant is added. Typically for P-type silicon, boron is used as the dopant.

For N-type doping, the addition of these dopants adds electrons into the conduction band, again increasing the conductivity as more dopant is added. Most N-type silicon is doped with phosphorus; however antimony and arsenic doped silicon are commercially available as well.

A single crystal of silicon can be cut in to give different facets of silicon. The two most relevant of these are (100) and (111). Almost all technological applications use (100). One important property that varies with facets is the surface conductivity. Si(100) and (111) wafers were broken to expose Si{111} and Si{112} facets. These were then contacted with tungsten probes and the I-V curves were measured, revealing conductivities in the order {112} > {111} > {100} > {110}. Rectifying behaviour was observed with the two probes contacting {111} and {110}, and {110} and {112} facets, as seen in Figure 1.2 [7]. This is attributed to the varying degrees of band bending at the silicon–tungsten interface with greater band bending corresponding to greater conductivity.

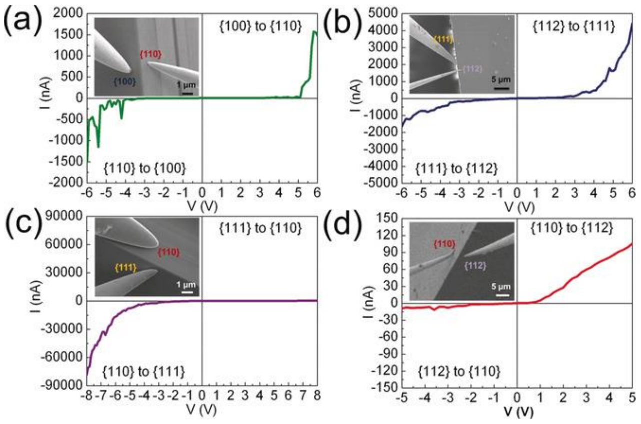

Figure 1.2: Current-voltage curves and SEM images of tungsten probes contacting various facets of a silicon wafer. a) Contacting 100 and 110 facets. b) contacting 112 and 111 facets. c) contacting 111 and 110 facets. d) contacting 110 and 112 facets. Used with permission from [7]. Copyright 2017, Wiley.

The work function of a material is the lowest energy required to eject an electron from its surface. This depends on a range of factors, including facet [8], surface chemistry [9] and doping [10].

1.1.2 Silicon in atomic force microscopy

As atomic force microscopy (AFM) is a primary method in this thesis, the properties of silicon in an atomic force microscope and under strain are of interest. The forces are typically small in an AFM experiment, up to the order of micronewtons, however, at the same time, the contact area can be on the order of nanometres. This can result in pressures on the order of gigapascals. This means that the effects of pressure on silicon cannot be ignored. Monocrystalline silicon undergoes a phase transition at 15 GPa at room temperature from a semiconducting state to a metallic state with a concomitant drastic decrease in resistivity [11]. Even at pressures below this, there is remains an effect on the band structure of silicon [12], resulting in a splitting of the conduction band and an enhancement in hole mobility.

Flexoelectricity was proposed by Sun et al. to tune the behaviour of a silicon-based Schottky diode formed in an atomic force microscope between a metallic Pt/Ir tip and p-type silicon (111) surface [13]. Flexoelectricity is the effect on the electrical properties of a material due to a non-uniform strain, such as a sharp AFM tip contacting a surface, breaking the symmetry of a material, in this case, silicon. Silicon has a centrosymmetric crystal structure so does not display bulk piezoelectricity, however flexoelectricity is still present which affects the electrical properties of the silicon [14], increasing its conductivity with increased strain. Flexoelectricity, studied by varying the normal force of the AFM tip, was shown to play a significant role in varying the current-voltage response of the diode, as shown in Figure 1.3.

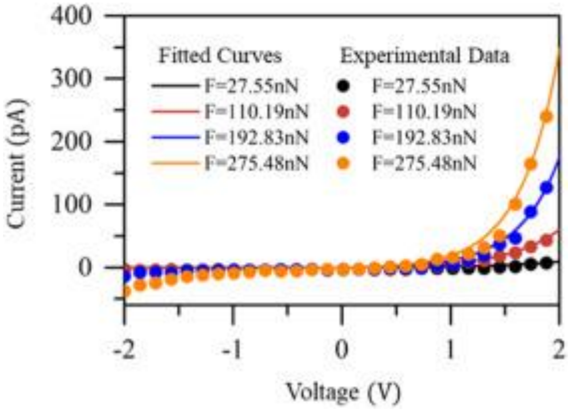

Figure 1.3: Effects of flexoelectricity by varying the applied tip force on the current-voltage response curve of a Schottky diode formed in AFM. Fitted curves are fitted to classical thermionic emission theory. Used with permission from [13]. Copyright 2021, Elsevier.

1.1.3 Preparation of silicon surfaces

Silicon surfaces are coated with an unclean layer of oxide when obtained from suppliers which requires cleaning and preparation to obtain the surface chemistry that is of interest in this thesis. This requires harsh cleaning conditions to remove any organic compounds that may remain on the surface. To this end, piranha solution is used, which is a mixture of hot concentrated sulfuric acid and 30% hydrogen peroxide. This leaves a clean oxide layer on the surface.

There are a range of commonly used etchants to remove the native SiO_x layer and replace it with hydrogen termination on the surface of silicon wafers. Hydrofluoric acid, buffered oxide etch and ammonium fluoride are all in use, however ammonium fluoride was used for all procedures in this thesis. Ammonium fluoride has a range of advantages over hydrofluoric acid. Hydrofluoric acid is extremely hazardous and deaths have resulted from exposure to as little at 2.5% of body area [15]. Ammonium fluoride on Si(111) surfaces produces an atomically flat surface compared to the atomically rough surface produced with hydrofluoric acid [16]. There is similarly a variation in the hydride termination of these surfaces: Si(111) ends up with monohydride (Si–H), dihydride ($Si–H_2$) and trihydride ($Si–H_3$) termination when etched with hydrofluoric acid, while ammonium fluoride produces dominantly monohydride termination [17]. In contrast to Si(111), Si(100) remains rough with ammonium fluoride etching with dihydride termination dominating, however forming some Si(111) surfaces. These appear as protuberances in scanning tunnelling microscopy up to 20 Å tall after 10 seconds of ammonium fluoride etching, as shown in Figure 1.4 [18].

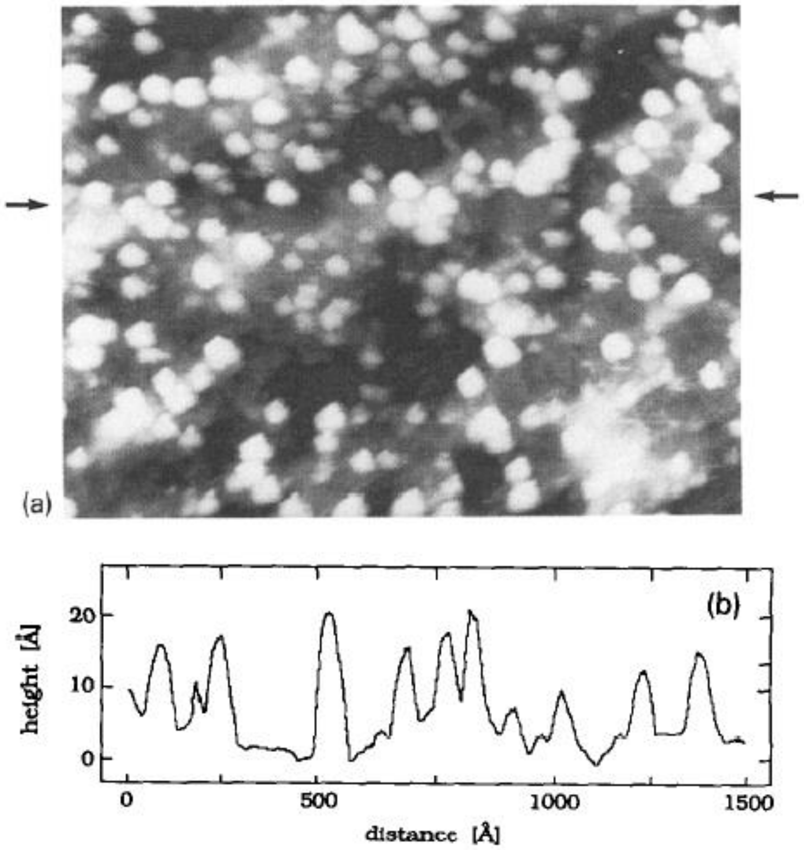

Figure 1.4: Si(100) surface after 10 s of etching in 40% NH_4F *solution after oxide was removed with HF. a) SEM image of flat regions with protuberances. b) Cut along of the line indicated by the two arrows in a). Used with permission from [18]. Copyright 1993, Elsevier.*

These hydride terminated surfaces are unstable on the order of hours in air, so the immediate usage or further modification is prudent [19]. This can be reoxidised in a controlled fashion by the use of chemical vapour deposition or reacted further with organic molecules to form organic monolayers.

Silicon (100) wafers can be etched with hydroxide-containing solutions to form pyramids on the surface [20]. The hydroxide will oxidise the silicon to form silicates and hydrogen, via the following reactions:

$$Si + 2\ OH^- \rightarrow Si(OH)_2^{2+} + 4\ e^- \qquad \text{(Equation 1.1)}$$

$$Si(OH)_2^{2+} + 4\ e^- + 4\ H_2O \rightarrow Si(OH)_6^{2-} + 2\ H_2 \qquad \text{(Equation 1.2)}$$

$$Si + 2\ OH^- + 4\ H_2O \rightarrow Si(OH)_6^{2-} + 2\ H_2 \qquad \text{(Equation 1.3)}$$

Typically 2-propanol is added to complex the formed silicates and avoid redeposition [21]. This anisotropic etching is due to the etching rate in the ⟨100⟩ direction is 100 times faster than in the ⟨111⟩ direction [20]. This etching with a solution saturated with 2-propanol however results in the formation of higher index {567} planes [22], but after further ammonium fluoride etching, {111} planes are produced.

These pyramidal nanostructures have found a variety of uses in the literature, from increasing efficiency of solar panels due to their increased ability to trap light [23] to decreasing cell adhesion on silicon surfaces [24].

1.2 Monolayers

1.2.1 Introduction to monolayers

Organic monolayers on silicon are a well-studied and versatile platform for the modification of silicon surfaces. This affords us a great deal of control over the properties of these surfaces. Surface modification affects physical properties such as the wetting of the surface and the work function, which can have positive effects on the output of TENGs. Chemical properties such as kinetics of reactions can also be affected, protecting surfaces from oxidation or unwanted chemical processes.

1.2.2 Silane monolayers on silicon

The first type of monolayers on silicon studied were formed from silanes on silicon oxide layers. Untreated silicon is covered with a layer of native oxide approximately 2 nm in thickness. After cleaning with piranha solution (3:1 98% H_2SO_4/30% H_2O_2), this oxide can be reacted with silanes to form organic monolayers attached by Si–O bonds enabling access to a wide variety of chemistries. [25] A pertinent disadvantage of the usage of these silane-derived monolayers for is the insulating nature of the silicon oxide layer, decreasing performance of electronic devices using this as a substrate for monolayers [26].

Silane monolayers do allow us access to a range of terminal functionalities-providing us with an interesting platform for the study of surface chemistry effects. However, they require an oxidised silicon surface, which we desire to avoid. Electrical transport through these oxidised layers can be very low [27]. They provide a very well-studied platform for a range of physical properties, e.g. friction [26, 28], however they are prone to hydrolytic cleavage, especially in electrolyte solutions reducing usefulness in studying aqueous electrochemical processes e.g. ferrocenylated monolayers [29]

1.2.3 Carbon-based monolayers on silicon

Silicon–carbon-bound monolayers were first formed by Linford and Chidsey in 1993 [30]. Diacyl peroxides were thermally decomposed to generate alkyl radicals which attached to hydrogen-terminated Si(100) and Si(111) surfaces. These surfaces were compared to structurally similar thiols on gold and silane-derived monolayers on oxidised silicon. These alkyl monolayers were seen to be very robust, comparably so to the silane-derived monolayers.

Further improvements upon this method was achieved by using 1-alkenes on hydrogen-terminated Si(111) surfaces [31]. Similar diacyl peroxides were used as radical initiators. Thermal hydrosilylation was also achieved without the use of a radical initiator. The usage of ultraviolet (UV)-catalysed hydrosilylation with 1-alkenes was also achieved with high quality monolayers formed [32].

1.2.4 Synthesis of monolayers

1.2.4.1 Hydrosilylation reactions

A powerful reaction for the formation of Si is the hydrosilylation reaction, which turns a Si–H bond into a Si–C bond. A hydride-terminated surface of silicon is required for these reactions which is readily prepared by methods described in 1.1.3. For the carbon-containing portion of the monolayer, an alkene [33] or alkyne [34] is required for the Si–C bond to form, as shown in Figure 1.5. There however is a surprising diversity in the mechanisms by which this reaction can happen, including UV-catalysed [35], white-light catalysed [36], thermal [37] and with a radical initiator [30]. UV-catalysed hydrosilylation is used in this thesis due to the milder conditions and ease of preparing many samples in parallel.

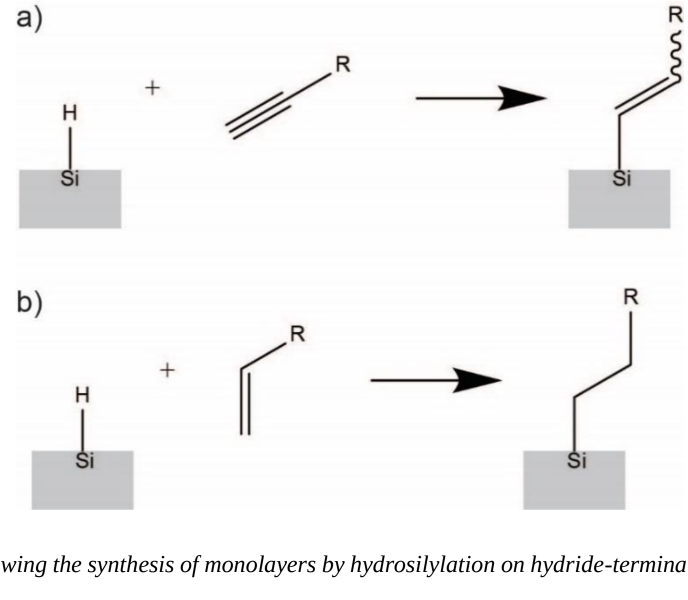

Figure 1.5: Schematic showing the synthesis of monolayers by hydrosilylation on hydride-terminated silicon using a) alkynes and b) alkenes.

1.2.4.2 Clicked monolayers

With the use of α,ω-dialkynes, such as 1,8-nonadiyne, a hydrosilylation reaction can attach a monolayer with a terminal alkyne functionality. This alkyne functionality can then be reacted in a copper-catalysed azide-alkyne coupling (CuAAC) reaction. This reaction involves an azide and an alkyne reacting to form a 1,2,3-triazole with a copper(I) catalyst as shown in Figure 1.6. The high yield and ease of this reaction has placed it firmly within the realm of "click chemistry", to the point where it is also known as the click reaction [38]. This allows the attachment of a wide range of new functionalities to the monolayer in good yield [34].

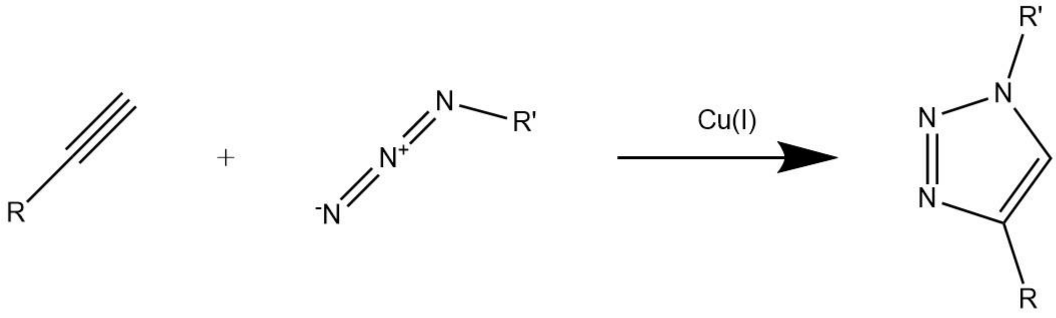

Figure 1.6: Schematic of the CuAAC reaction

One important feature of this reaction is that it forms a 1,2,3-triazole within the monolayer. 1,2,3-Triazoles have large dipole moments and are aromatic which can affect the electrical properties of the monolayer, as it will be seen in Chapter 4.

One particularly useful functionality is a ferrocenyl moiety [39]. This redox-active functionality allows the study of electron transfer reactions through the monolayer and an assessment of the coverage and thus efficiency of the CuAAC reaction.

1.2.5 Copper in click reaction

As the CuAAC reaction uses a copper catalyst, it is worth noting that the presence of copper impurities in the prepared monolayer can affect the properties of the surfaces, as will be discussed in Chapter 5. Transition metal ions such as copper decrease the carrier lifetime by increasing the surface recombination velocity by increasing the density of trap states at the surface [40, 41].

Triazole coordination to copper is well established [42]. This copper contamination has been observed by X-ray photoelectron spectroscopy (XPS) [43]. In some cases, the copper was completely removed to within the noise of the XPS experiment [44]. This was further studied by Wu et al. by scanning photo-induced impedance microscopy (SPIM) to visualise copper after a patterned CuAAC reaction, which revealed that copper(I) was not completely removed by aqueous hydrochloric acid [45]. Instead to completely remove the copper contamination, ethylenediaminetetraacetic acid acidified with trifluoroacetic acid was used.

1.2.6 Properties of monolayers

One property of surfaces that is easily tuned by the usage of monolayers is hydrophilicity and thus wettability. One of the simplest methods to characterise surfaces is a contact angle (CA) measurement. This involves placing a drop of water on a surface and measuring the angle between the surface and the droplet.

X-ray reflectometry (XRR) has also been used to study the deposition of water onto monolayer-modified silicon [46, 47].This work showed water deposited from the air onto the surfaces at different rates, which both the eventual thickness of the water layer and the kinetics of the deposition depend heavily on the identity of the monolayer. For the CuAAC modified monolayers, poor agreement between macroscale water CA and XRR-determined water deposition. The most hydrophobic surface (a 1,8-nonadiyne-derived monolayer) in [46] adsorbed a thicker water layer than a more hydrophilic amine terminated surface, while the ferrocene and butyl terminated surfaces have similar contact angles but the butyl monolayer adsorbed significantly less water than the ferrocene terminated surface.

Oxidation of a hydride-terminated silicon substrate while scanning by AFM was observed. This was attributed to the interaction between the in-built electric field of the Pt-Si Schottky diode and adsorbed water. This was seen to be reversed however by annealing in an environment of nitrogen [48]. An advantage of using organic monolayers is that this oxidation of silicon during scanning is minimised and a sharp drop off in current is not observed. 1,8-nonadiyne derived monolayers can protect from oxidation in aqueous electrolytic systems. [49]

1.3 Friction

1.3.1 Introduction to friction

Friction is everywhere. Wherever two surfaces are in contact and motion, there is friction. Friction typically converts some of this motion into heat, where it is lost to the environment.

The simplest model of friction between two surfaces is Amontons' Law (Equation 1.4).

$$F_{friction} = \mu F_{normal} \qquad \text{(Equation 1.4)}$$

This describes macroscopic systems well, where the friction force depends only on the normal force and the apparent contact area does not seem to matter.

There are a range of open questions in friction however including the role of water, electrostatics and the electronic components of friction. This is further explored in Chapter 4 with an examination of the effects of monolayers on friction.

1.3.2 Electron-hole excitation

Friction is dissipated in a number of different mechanisms. This includes phonon emission, exoelectron ejection, photon ejection and electron-hole excitation [50]. Of these mechanisms, electron-hole pair excitation is of most interest to us, as it provides a pathway to generate electricity in a similar mechanism to the photoelectric effect.

On a metallic or semiconducting surface, of interest to the development of direct current (DC)-TENGs is the generation of electron-hole (*e-h*) pairs. A range of alkane adsorbates on Cu(100) surfaces were studied and a pronounced effect of formation of *e-h* pairs on the damping of parallel adsorbate vibrations was observed [51]. This phenomenon is further supported by the effect of a transition from a conductor to a superconductor decreasing the friction of physisorbed layers of gases [52, 53].

A pronounced effect of doping of silicon on friction was observed by Park et al. [54]. An n-type doped substrate was implanted with highly doped p-type stripes and current and friction were simultaneously measured at +4 V applied bias as shown in Figure 1.7. This bias put the p-type regions into strong accumulation and the n-type regions into depletion or weak inversion. A large excess of friction was observed on the p-type regions compared to the n-type regions without a concomitant increase in wear.

This was followed up by the same group, who further examined the effect of the bias between the tip and sample [55]. Adhesion was not found to vary between the p and n-type regions as the bias was varied. Friction, however, was again seen to increase on the p-type regions when the p-type regions were in strong accumulation.

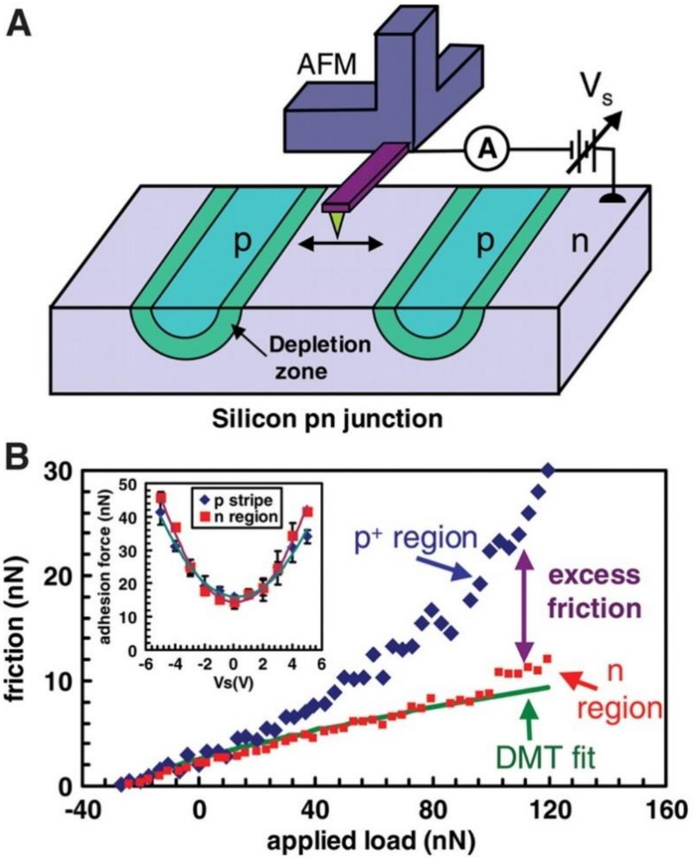

Figure 1.7: A) A schematic of the AFM experiment, showing the p-type stripes embedded in n-type silicon. B) Plot of the friction force on each region at +4 V applied bias, showing excess friction on the p-type regions. Inset shows the lack of difference of the adhesion force between the two regions as a function of sample bias. From [54]. Reproduced with permission from AAAS.

This phenomenon of excess friction in accumulation was confirmed by the study of n-type gallium arsenide. The proposed mechanism by which accumulation leads to excess friction is that of electrostatic effects from trap states leading to a trail of charged traps which leads to additional attraction and thus excess friction [56].

The interaction of hexadecanethiol-modified metal surfaces showed a pronounced effect of the identity of the metal pair on the friction and triboelectricity [57]. Charge transfer and *e-h* pair formation was observed to be dominant mechanisms in the friction between the monolayer-modified metal surfaces. Direct current triboelectricity was also observed at an applied pressure of 6 MPa between the Ti and Au surfaces and Ag and Au surfaces.

1.3.3 Friction on monolayers

Friction was studied on a series of monolayer pairs by LFM by Li et al. [58]. A gold-coated AFM tip was modified with either dodecanethiol or 10-mercaptodecanoic acid to provide tips with either methyl or carboxylic acid termination. These were studied against a gold surface modified with a series of short chain (3 carbon) or long chain (11-12 carbon) thiols with either a methyl, alcohol or carboxylic acid termination. Greater friction was seen with short chain monolayers and when the polar or non-polar terminations of the tip matched the polar or non-polar termination of the surface. This work clearly indicates the potential effects that monolayers can have on friction.

The adhesion and friction of monolayers on silicon were studied again by the same group [59]. Using silicon nitride tips, the friction coefficients of various monolayer-modified and chemically modified Si(111) surfaces were studied, including oxide-terminated silicon, hydride terminated and those modified with 1-dodecene and methyl undecyl-10-enate or undecyl-10-enic acid. Water contact angle was seen to correlate with friction coefficient on the monolayer-modified surfaces however the friction coefficient on oxide-terminated silicon was much higher than the monolayer-modified surfaces.

The effect of humidity was studied on monolayers on gold synthesised with a mixture of dodecanethiol and 11-mercaptoundecan-1-ol, which showed a clear relationship between the friction coefficient and the surface composition [60]. Friction coefficients on the 11-mercaptoundecan-1-ol-modified surface were seen to strongly depend on the relative humidity with a decrease as the humidity increases, whereas friction coefficients on the dodecanethiol-modified surface were comparatively insensitive to the humidity. The effect of humidity on friction on monolayers is of interest to this thesis as hydrophilic and hydrophobic monolayers are compared at uncontrolled room humidities, comparable to the higher end of this paper.

1.4 Triboelectric nanogenerators

1.4.1 Introduction to nanogenerators

Nanogenerators are a powerful emerging energy generation technology. They convert mechanical energy directly into electrical energy. One such specific type is the triboelectric nanogenerator (TENG), first reported in 2012 by Zhong Lin Wang’s group [61]. This device consisted of a layer of polyester and a layer of Kapton as seen in Figure 1.8, which were bent and then released to generate a power density of 10.4 mW cm^{-2}. This device generates alternating current (AC) as current is generated in one direction when the TENG is bent and the other direction is generated when the TENG is relaxed. This is characteristic of polymer-based TENGs.

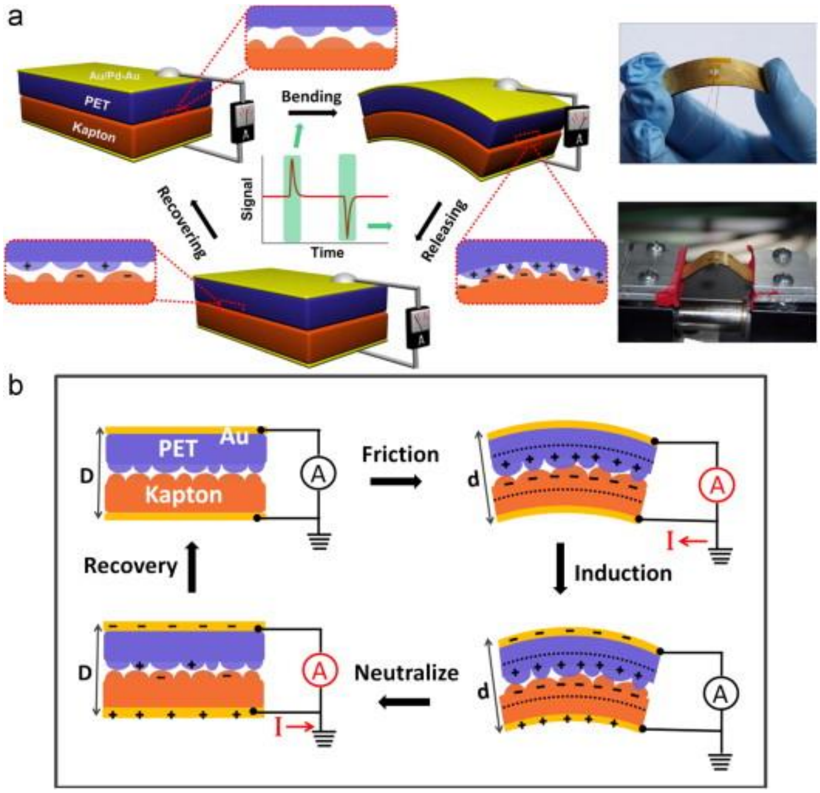

Figure 1.8: Structure and mechanism of polymer-based TENG. a) Structure and current response of a PET-Kapton TENG. b) Mechanism of this polymer-based TENG. Charges are generated at the interface between the two polymer layers by friction, which induces charges in the metallic electrodes which then neutralise and the polymer layers recover, enabling the cycle to begin again. Used with permission from [61]. Copyright 2012, Elsevier B.V.

TENGs are particularly advantageous for the capturing of energy from low frequency and small amplitude motions as compared to traditional electromagnetic generators [62]. The question remains: how to generate the direct current required by many devices? Many clever solutions have been found using polymer-based TENGs, including using a dielectric breakdown of air to rectify the current [63] and using a rotating disk setup [64].

The applications of TENGs vary immensely from the more traditional sensing and power generation for sensors to the new areas of using electricity to assist in wound healing [65] or electroculture of plants [66].

p-n diodes have been studied in and have a similar mechanism to Schottky diode-based TENGs, in that, friction generates electron–hole pairs at the surface which are then separated by the built-in electric field of the p-n diode [67]. This was further explored with a range of combinations of different semiconductors. A dynamic MoS_2/AlN/Si generator was found to be ideal, working for up to 60 minutes continuously. The large band gap and interface barrier height of the AlN layer was found to increase the output substantially over other insulators used in the device [68].

The first Schottky diode-based TENG used a semiconducting polypyrrole (PPy) layer sandwiched between an aluminium and gold electrode, creating an AlPPy Schottky junction and an ohmic AuPPy Schottky junction. This TENG generated direct output current densities of up to 2.186 A m^{-2}. The authors also note that the output of this device is not due to the triboelectric effect, an early indication of the difference in mechanism between typical polymer-based AC TENGs and semiconductor-based DC TENGs [69]. The same group studied a similar system with polyaniline doped with various protonic acids and found a significant increase in the current and voltage outputs: a maximum of 0.339 A m^{-2} and 0.9 V with the use of HCl as a dopant [70].

The first usage of an inorganic semiconductor was achieved in 2017 by Liu et al. in the form of molybdenum disulfide showing a far greater current output than semiconducting polymer-based TENGs [71]. A MoS_2 thin film was deposited on Ag which was then studied by conductive AFM (C-AFM). This demonstrated clearly the feasibility of studying these devices by C-AFM. One issue seen with the MoS_2 layer was a large variability between the electrical behaviour between individual grains. This gave rise to a range of electrical behaviours as shown in Figure 1.9.

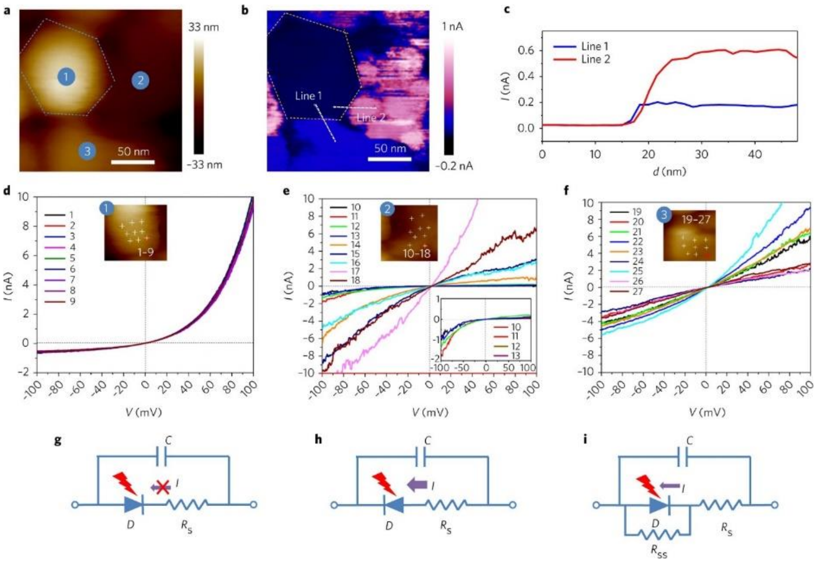

Figure 1.9: a) Topography image from AFM showing three labeled grains of MoS_2. b) Current image from AFM of same region as a), showing a difference in tribocurrent between grains.. c) Current along lines 1 and 2 as shown in b). d-f) I-V curves on each region in a), highlighting the different electrical behaviour between grains. g-i) Equivalent circuits of tip-grain contact corresponding to the grains in a), where C is the capacitance of the depletion region, R_s is the resistance of the surface and D is the Schottky diode. Used with permission from [71]. Copyright 2017, Springer Nature.

The usage of MoS_2 was scaled up by the same group and examined in metal/semiconductor, metal/insulator/semiconductor and semiconductor/insulator/semiconductor configurations. A range of mechanisms for the dc conduction were proposed: thermionic emission for the metal/semiconductor configuration, defect conduction for the metal/insulator/semiconductor configuration and tunnelling of the tribo-excited carriers for the semiconductor/insulator/semiconductor case [72].

The first usage of silicon as a semiconductor for TENGs was again achieved by the same research team [73]. The use of silicon wafers avoided the inhomogeneity associated with pulsed laser deposited MoS_2. Their macroscale study also showed an enhancement in current output over polymer-based TENGs and PENGs. Friction-induced tunnelling was found to be a cause of generation of direct current in all silicon dopings studied, however Fermi level pinning due to the SiO_2 layer on the surfaces was found to enhance the current on p-type silicon surfaces, as seen in Figure 1.10 [74]. An inversion of the sign of the voltage was seen after etching with HF which removed the oxide layer and thus reduced the Fermi level pinning.

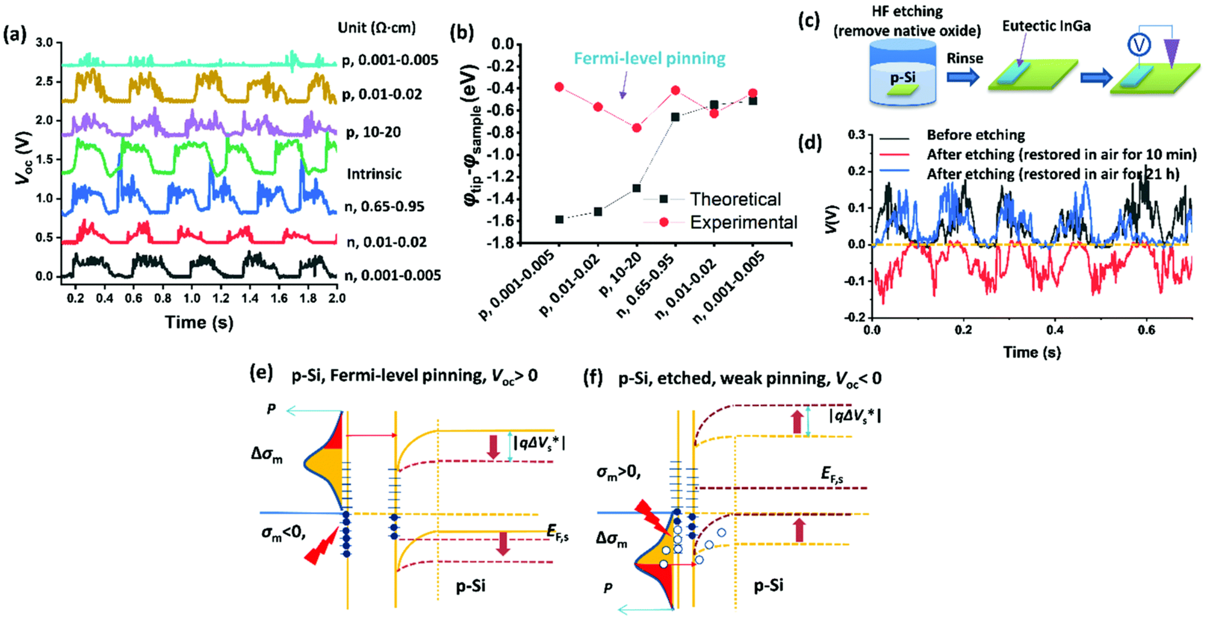

Figure 1.10: Effects of doping and Fermi pinning on TENG output. a) Open circuit voltage output of different dopings of silicon. b) Experimentally and theoretically determined surface potential differences showing Fermi level pinning. c) Removal of surface oxide using HF. d) Open circuit voltage output after HF etching after 10 minutes (removal off oxide) and 21 hours (restoration of oxide layer), demonstrating the inversion of sign due to reduction of Fermi level pinning. e) Energy band diagram of the metal–silicon contact before HF etching. f) Energy band diagram of the same contact after HF etching. Used with permission from [74]. Copyright 2019, Royal Society of Chemistry

One issue with these Schottky diode-based TENGs is the low voltage outputs; typically less than 0.5 V. One solution to this is to use an array of microtips in parallel to increase the voltage output, however the machining of these microtips is complex and inefficient. The use of a conductive carbon aerogel which functions as a Schottky contact with a large number of individual contacts achieved an open circuit voltage approaching 2 V, a viable voltage to power devices [75].

1.4.2 Mechanisms

To discuss diode-based TENGs, a brief discussion of polymer-based TENGs is warranted. Three mechanisms are at play in these: electron transfer, ion transfer and material transfer. There is a material dependence here as there is a range of phenomena that are explained by each mechanism but different effects are observed with different materials [76]. Irrespective of these mechanistic questions, for a polymer-based TENG, the two polymer electrodes become oppositely charged, which induces image charges in the metal contacts, forcing current to flow as shown in Figure 1.5 [77].

In 2019, Wang and Wang coined the term “tribovoltaic effect” with explicit reference to p-n junctions [78]. They note the depletion layer is a few nanometres thick while the contact electrification only occurs at the interface directly. The surface states are filled with holes on the p-type and electrons on the n-type. When these two surfaces contact, electrons flow from the surface states of the n-type to the p-type, resulting in a negatively charged p-type surface and a positively charged n-type surface. This releases enough energy to separate electron-hole pairs in a fashion similar to the photovoltaic effect, thus the term, tribovoltaic effect.

This similarity is further compounded by the observations of Ren et al. [79], who examined a p-type Si wafer sliding against an n-type GaN wafer under illumination with UV light. This motion generates direct current by the tribovoltaic effect, however under illumination, the photovoltaic effect also generates current. This led to a 13-fold increase in current and a 4-fold increase in voltage, demonstrating the coupling between the photovoltaic and tribovoltaic effects.

Another supporting observation to that of the involvement of surface states was by the increase in current when using surfaces that were etched with reactive ion etching. This roughens the surface and increases the density of surface states. An increase in current was seen with all of p-n, n-n^+ and Schottky junctions, shown in Figure 1.11, clearly demonstrating the tribovoltaic effect [80].

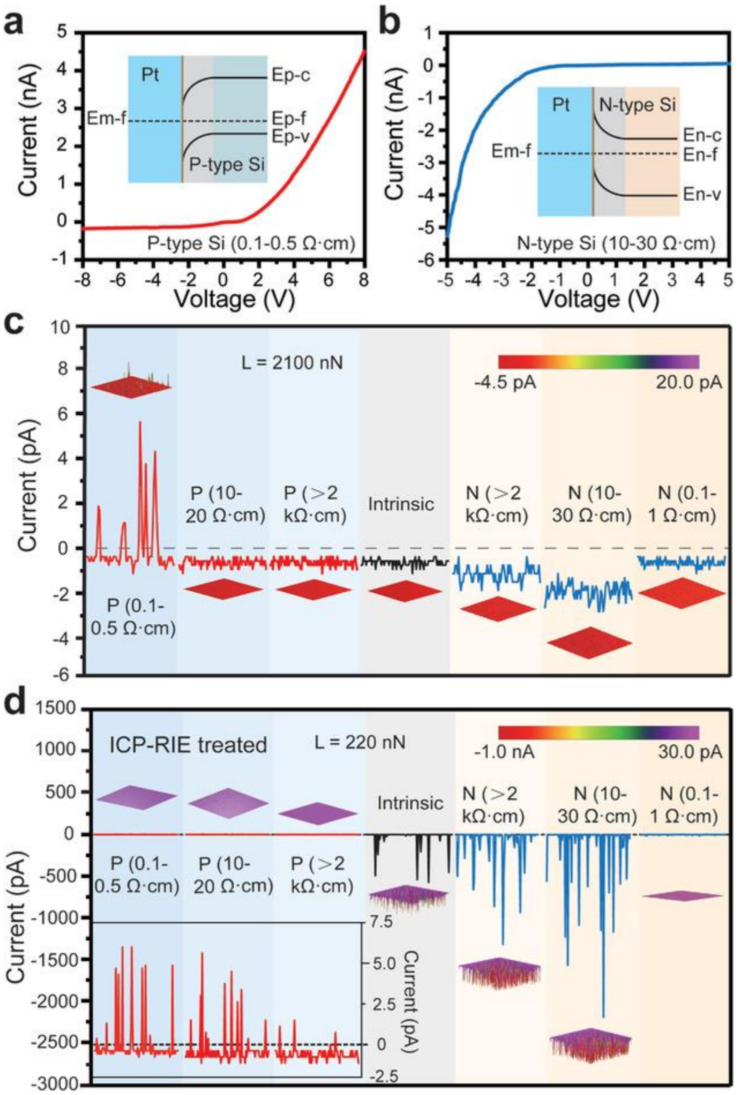

Figure 1.11: Tribocurrent between Pt and Si with different dopings. a) I-V curve on P-type silicon with band diagram showing the band bending. b) I-V curve on N-type silicon with band diagram. c) Tribocurrent on non-etched surfaces with different dopings. d) Tribocurrent on reactive ion etched surfaces, showing an enhancement in current. Used with permission from [80]. Copyright 2020, Wiley

The tribovoltaic effect has also been demonstrated at liquid-semiconductor interfaces [81]. A water–silicon junction was shown to have similar rectifying properties to solid metal–silicon interfaces as shown in Figure 1.12. The tribovoltage and tribocurrent were both found to depend on the built-in electric field induced by the tribovoltaic effect.

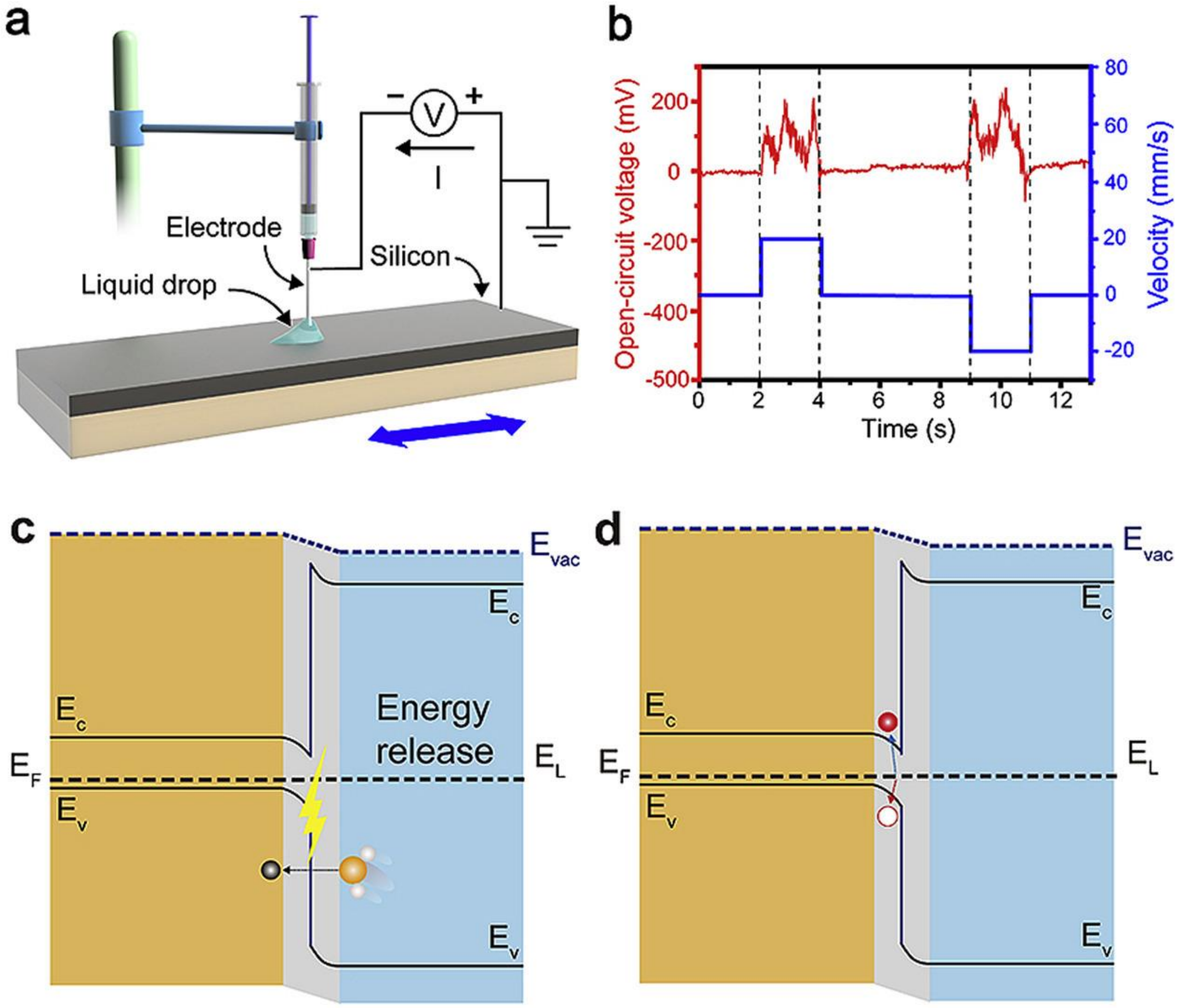
a
Electrode
Liquid drop
Silicon
V
I
b
Open-circuit voltage (mV)
Velocity (mm/s)
Time (s)
200
0
-200
-400
-500
80
60
40
20
0
-20
0
2
4
6
8
10
12
c
E_{vac}
E_c
Energy release
E_c
E_F
E_L
E_v
E_v
d
E_{vac}
E_c
E_c
E_F
E_L
E_v
E_v

Figure 1.12: Water-silicon TENG. a) Schematic of the experiment, showing the water-silicon TENG. b) Voltage response the motion of the TENG. c) Energy band diagram showing band structure of when water is in contact with the silicon. d) Energy band diagram showing excitation of electron-hole pair. Used with permission from [81]. Copyright 2020, Elsevier.

The tribovoltaic effect at a liquid-semiconductor interface with illumination has also been examined [82]. A similar enhancement of the tribocurrent and tribovoltage was seen here under illumination, indicating a similar mechanism as to that proposed in [79]. Temperature effects were also studied by the same group, with increasing temperature observed to give an increase in current and voltage [83].They attribute this to the increase in formation of bindington, the energy released from forming chemical bonds which is Wang’s theory for the origin of the tribovoltaic effect.

Huang et al. constructed a similar device but using a microscale flake of graphite and n-type silicon in a structural superlubric state [84]. This achieved high current (~210 A m^{-2}) and power (~7 W m^{-2}) densities and a high level of electrical stability. This is particularly of interest as the bindington mechanism cannot explain these observations, as the friction force from dangling bonds of the graphite is too small in these devices to excite sufficient electrons from the valence to conduction band of silicon or tunnel from the graphite into the conduction band of the silicon. The proposed mechanism to account for these observed currents is that of a depletion layer establishment and destruction, which was simulated and shown in Figure 1.13. They do note however that with an AFM tip that the friction force is sufficient to excite electrons to generate the observed current.

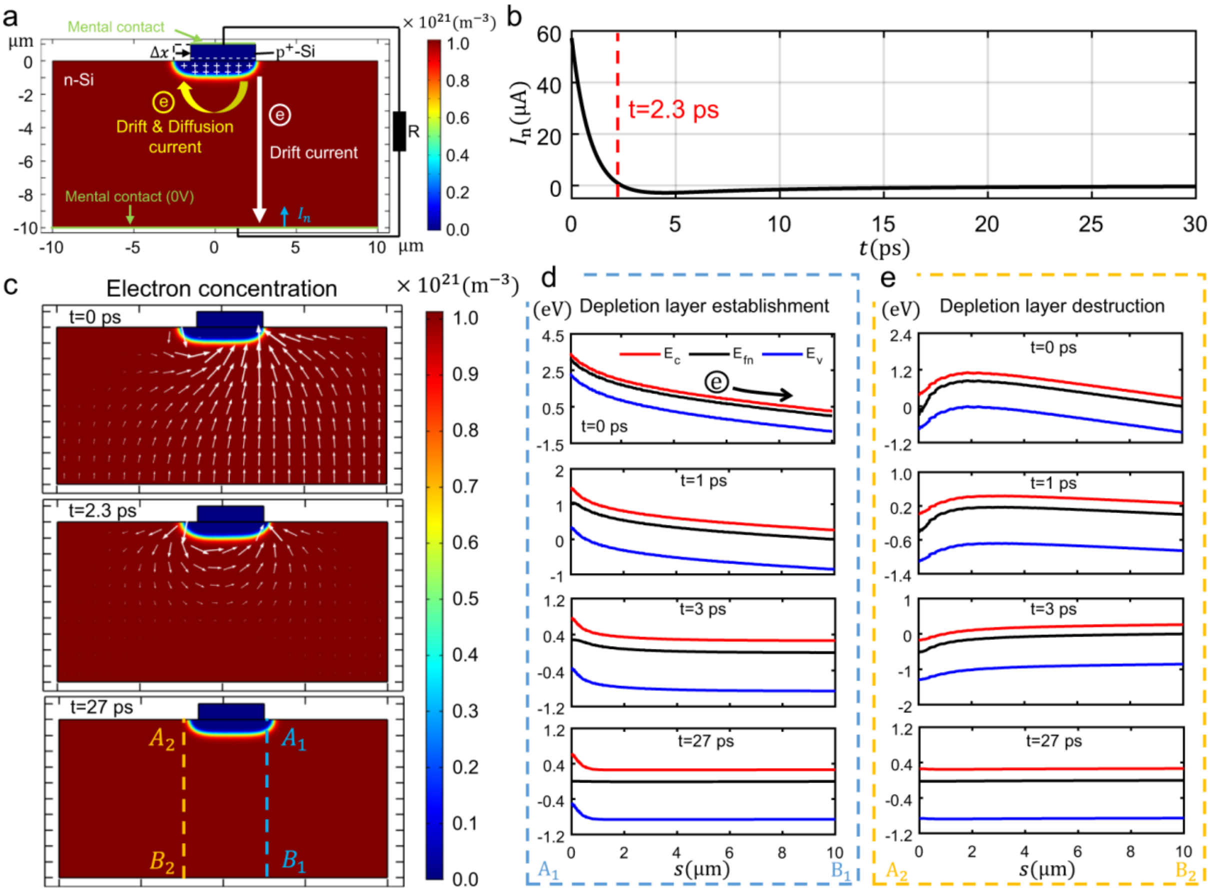

Figure 1.13: Depletion layer establishment and destruction mechanism. a) Quasi-static finite element simulation model structure and physical process. b) Output current along bottom surface with time. c) Electron concentration with time with arrows showing the direction of the current. d) Distribution of the band and Fermi level energies along the A1-B1 line in c). e) Distribution of the band and Fermi level energies along the A2-B2 line in c) Reproduced under Creative Commons Attribution 4.0 International License from [84].

This plurality of three primary mechanisms is summarised in Figure 1.14.

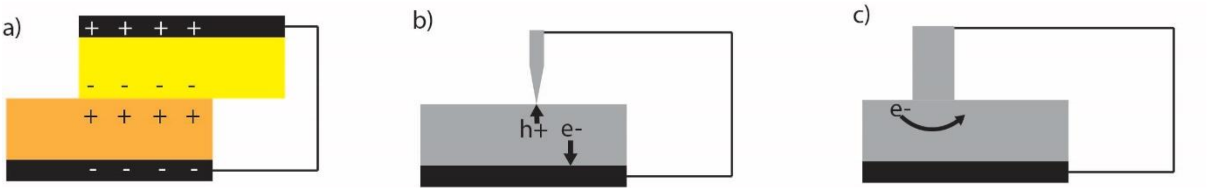

Figure 1.14: Summary of TENG mechanisms. a) Polymer based TENGs, which generate AC based on static charging of surfaces, b) Diode based TENGs which generate DC based on separation of electron-hole pairs, c) Graphite based TENGs which generate DC based on depletion layer establishment and destruction.

1.5 Thesis Overview

Chapter 2 will describe the methods generally used in this thesis. Presented within are details of the surface preparation for each chapter, the AFM experiments used and the electrochemical procedures.

Chapter 3, already published in *Nano Energy* in 2020, will examine the effect of sharp lateral changes in the conductivity and electrical properties of Pt–Si-based Schottky diodes. Surfaces were microtextured with Si(111) pyramids on a Si(100) surface to create Si(111)–Si(100) junctions which were examined by conductive AFM. Sharp increases in current were seen at the concave boundaries between the Si(111) and Si(100) facets. FZ lowly doped n-type silicon was observed to have the highest current output, followed by CZ lowly doped n-type, obeying the trend of the minority carrier's mobility. The highest currents were observed on the largest pyramids.

Chapter 4, already published in *Nano Energy* in 2021, will explore the effects of surface chemistry on the friction and current output of Pt–Si based Schottky diodes of which the silicon was modified with organic monolayers. The surface chemistry was engineered to control a range of properties, including friction, wettability and work function. The current was observed to double in the case of the amine and alcohol terminated surfaces as opposed to the methyl terminated and thinner alkyne terminated surfaces, paralleling the effect of increased friction observed. A profound effect on the friction by the doping of the underlying silicon was observed with a large increase on n-type versus p-type.

Chapter 5 will examine the electrochemistry of some of the surfaces studied in Chapter 4 with an emphasis on the viability of detecting the copper trapped in the CuAAC-derived monolayers by electrochemical techniques.

Chapter 6 will conclude this thesis and examine future directions for the field of DC TENGs on oxide-free silicon surfaces.

Chapter 2 Materials and Methods

2.1 Introduction

A range of experimental procedures were undertaken in the course of this thesis with a view towards preparation and characterization of surfaces for the study of the fundamentals underpinning triboelectric nanogenerators.

To prepare surfaces for study, Si(100) or (111) surfaces were cleaned with piranha solution, etched with ammonium fluoride to prepare hydrogen-terminated surfaces and then further modified depending on the desired surface.

To prepare pyramidally textured surfaces, a potassium hydroxide etch was used as this anisotropically etches Si(100) to reveal higher order facets. This was then etched again with ammonium fluoride to prepare hydrogen-terminated surfaces ready for hydrosilylation with 1,8-nonadiyne, which forms a passivating layer protecting the surface from oxidation.

For azide-modified surfaces, the hydrogen-terminated Si(111) surfaces were reacted with 1,8-nonadiyne, which also has a terminal alkyne group, allowing further modification with a range of azide-containing molecules in a Cu-catalysed azide-alkyne cycloaddition to prepare 1,2,3-triazoles with a variety of terminal functional groups. Amine, alcohol and methyl terminated surfaces were prepared for study by atomic force microscopy for TENGs while amine and ferrocene terminated surfaces were prepared for electrochemical study.

To characterise these surfaces and assure that the surfaces prepared were those expected, a range of techniques were used. Contact angle measurements were used to determine the hydrophilicity of a surface. X-ray reflectometry was used to determine thickness of monolayers and x-ray photoelectron spectroscopy was used to determine the elemental composition of surfaces.

For electrochemical characterisation, a series of techniques were used, including cyclic voltammetry, electroimpedence spectroscopy and open circuit potential measurements. Cyclic voltammetry was used to measure the coverage of ferrocene moieties, the presence of Cu and the kinetics of the electron transfer to ferrocene. Electroimpedence spectroscopy was used to determine the kinetics of electron transfer to ferrocene and the flat-band potential. Open circuit potential measurements were used to measure the open circuit potential which was attempted to be correlated with the presence of Cu trapped in the monolayers.

Atomic force microscopy was used in a range of modes to characterise surfaces. The Peak Force TUNA mode was used to measure the triboelectric output of pyramidally textured surfaces, which also recorded topographical and micromechanical information. For azide-modified surfaces, conductive lateral force microscopy was used, as this gives information about the topographical, electrical and frictional properties of the surfaces studied.

2.2 Materials

Hydrogen peroxide (30 wt % in water), ammonium fluoride (Puranal, 40 wt % in water), and sulfuric acid (Puranal, 95−97%) used in wafer cleaning and etching procedures were of semiconductor grade and obtained from Sigma-Aldrich. Redistilled solvents and Milli-Q water (>18 MΩ cm) were used for substrate cleaning, chemical modification procedures and to prepare electrolytic solutions. Potassium hydroxide (99.99% trace metals), 1,8-Nonadiyne (98%), 3-azidopropan-1-amine (≥95%), 3-azidopropan-1-ol (≥96%), sodium ascorbate (crystalline, 98%) were obtained from Sigma-Aldrich. 1-Azidobutane [85] and azidomethylferrocene [86] were synthesized according to literature procedures. Copper sulfate ($CuSO_4•5H_2O$) was purchased from Chem-Supply. Prime grade Si(100) and Si(111) silicon wafers (± 0.05°) were obtained from Siltronix, S.A.S (Archamps, France). Wafers were 500 µm thick, polished on one side only, and were of either N- or P-type (phosphorus- or boron-doped) with a resistivity of 7–13 Ω cm, hence referred to as lowly doped or 0.007–0.013 Ω cm, hence referred to as highly doped. Lowly doped N-type wafers were either float zone (FZ) or Czochralski process (CZ), while all other wafers were CZ process.

2.3 Preparation of surfaces

2.3.1 Preparation of pyramidally microtextured silicon surfaces

Silicon (100) wafers were cut into 1 cm by 1 cm pieces and rinsed with dichloromethane, 2-propanol and MilliQ water. The rinsed wafers were then placed into piranha solution (130 °C, 3:1 98% sulfuric acid/30% hydrogen peroxide) for 30 minutes. They were then rinsed with MilliQ water. The etched pieces were then placed in 40% ammonium fluoride solution for 10 minutes, degassed with argon to which a small amount of ammonium sulfite was added as an oxygen scavenger. The etched pieces were then rinsed in MilliQ water. The etched pieces were then further etched for 30 minutes at 65 °C in 20% potassium hydroxide solution to which a small amount of isopropyl alcohol was added. The etched pieces were then etched again in 40% ammonium fluoride for 10 minutes, again degassed with argon to which a small amount of ammonium sulfite was added. The etched pieces were then rinsed with MilliQ water and DCM and blown dry with nitrogen. The etched pieces were covered by 1,8-nonadiyne, deoxygenated with argon, and placed under a 312 nm UV lamp under nitrogen for 2 hours. The etched pieces were then rinsed with dichloromethane and stored in dichloromethane at 4 °C overnight before usage.

2.3.2 Preparation of azide-modified silicon surfaces for AFM

Silicon (111) wafers were cut into 1 cm by 1 cm pieces and rinsed with dichloromethane, 2-propanol and MilliQ water. The rinsed wafers were then placed into piranha solution (130 °C, 3:1 98% sulfuric acid/30% hydrogen peroxide) for 30 minutes. They were then rinsed with MilliQ water. The etched pieces were then placed in 40% ammonium fluoride solution for 13 minutes, degassed with argon to which a small amount of ammonium sulfite was added as an oxygen scavenger. The etched pieces were then rinsed in MilliQ water and dichloromethane and blown dry with nitrogen. The etched pieces were covered by 1,8-nonadiyne, deoxygenated with argon, and placed under a 312 nm UV lamp under nitrogen for 2 hours. These surfaces were rinsed with dichloromethane and used as synthesised after storing at 4 °C overnight or further reacted. The etched pieces for further reaction were rinsed with 2-propanol and then placed in a vial with a 1:1 (v/v) MilliQ water/2-propanol solution of 0.5 mM either 1-azidobutane, 3-azidopropan-1-ol or 3-azidopropan-1-amine; 0.1 mM copper sulfate and 0.5 mM sodium ascorbate. These were left to react in the dark for 30 minutes. After the reaction, they were rinsed with 2-propanol, dichloromethane, 2-propanol, MilliQ water, 0.5 M hydrochloric acid, MilliQ water, 2-propanol and dichloromethane. They were then stored at 4 °C overnight before analysis.

2.3.3 Preparation of azide-modified silicon surfaces for electrochemistry

Silicon (111) wafers were cut into 1 cm by 1 cm pieces and rinsed with dichloromethane, 2-propanol and MilliQ water. The rinsed wafers were then placed into piranha solution (130 °C, 3:1 98% sulfuric acid/30% hydrogen peroxide) for 30 minutes. They were then rinsed with MilliQ water. The etched pieces were then placed in 40% ammonium fluoride solution for 13 minutes, degassed with argon to which a small amount of ammonium sulfite was added as an oxygen scavenger. The etched pieces were then rinsed in MilliQ water and dichloromethane and blown dry with nitrogen. The etched pieces were covered by 1,8-nonadiyne, deoxygenated with argon, and placed under a 312 nm UV lamp under nitrogen for 2 hours. These surfaces were rinsed with dichloromethane and stored at 4 °C overnight before usage in electrochemical experiments or further reaction. The etched pieces for further reaction were rinsed with 2-propanol and then placed in a vial with a 1:1 (v/v) MilliQ water/2-propanol solution of 0.5 mM either azidomethylferrocene or 3-azidopropan-1-amine; 0.1 mM copper sulfate and 0.5 mM sodium ascorbate. These were left to react in the dark for 45 minutes. After the reaction, they were rinsed with 2-propanol, dichloromethane, 2-propanol, MilliQ water, 0.5 M hydrochloric acid, MilliQ water, 2-propanol and dichloromethane. They were then stored at 4 °C overnight before analysis.

2.4 AFM experiments

Experiments were performed in air and at ambient conditions (~22 °C, 45-55% humidity). All AFM experiments were performed using a Bruker Dimension AFM fitted with an Icon head with a PF-TUNA module. To estimate normal forces, the deflection sensitivity was measured and the cantilever spring constant was calibrated using the inbuilt Thermal Tune. Tip radius was measured using an RS-12M (Bruker) standard and deconvoluted using NanoScope Analysis (Bruker).

2.4.1 PF-TUNA for pyramids

AFM measurements were carried out in PF-TUNA mode, which allows simultaneous topographic, nanomechanical and electrical measurements. Solid Pt tips were used for all measurements (RMN-25PT300B, spring constant = 18 N/m, resonant frequency = 20 kHz, tip radius < 20 nm). Si surfaces were mounted to the AFM stage by conductive carbon tape. The Peak Force setpoint was set to 2 µN, the imaging resolution to 256 points/line and the scan rate to 1 Hz. Current–voltage measurements were performed at 2.25 µN and the current sensitivity set to 100 pA/V.

2.4.2 TUNA LFM for azide modified surfaces

AFM measurements were carried out in TUNA mode, which allows simultaneous topographic, friction and electrical measurements. Solid Pt tips were used for all measurements (RMN-12PT300B, spring constant = 0.8 N/m, resonant frequency = 9 kHz, tip radius < 20 nm).

Si surfaces were mounted to the AFM stage by gallium/indium eutectic on copper tape which was fixed to the stage with conductive carbon tape to prevent the sample from moving. The cantilever spring constant was calibrated using the inbuilt Thermal Tune and the deflection sensitivity calibrated using a silicon oxide surface. Deflection set point was set to between 0 and 100 nN at 5 nN intervals to determine the friction coefficient of these surfaces. Current sensitivity was set to 100 pA/V for scanning measurements and the scan angle was set to 90° to capture friction data. The imaging resolution was set to 256 points/line and the scan rate to 0.5 Hz. Friction was measured imaging a 2 μm × 200 nm region and subtracting the retrace friction image from the trace friction image and dividing the result by 2 to give a friction loop image. The middle 1.8 μm × 200 nm section was examined to avoid edge artifacts and the mean friction and standard deviation across the region were recorded. For force-distance curve measurements, the maximum deflection was set to 100 nN with a ramp size of 300 nm. These curves were recorded at 10 points across the image and the mean and standard deviations were recorded. For current–potential (I–V) measurements, the deflection set-point was set to 100 nN and the detector sensitivity was set to 1 nA/V.

2.5 Electrochemical Measurements

Experiments were performed using a CHI650D (CH Instruments) electrochemical workstation with a conventional three electrode setup in a custom Teflon cell. Modified silicon wafers were used as the working electrode, an Ag/AgCl (3.0 M KCl) electrode was used as the reference electrode and a Pt wire was used as the counter electrode. 1.0 M perchloric acid was used as the electrolyte. Experiments were carried out at room temperature (22 ± 2 °C). Open circuit potentials were measured for 30 minutes with the potential being recorded each second. Cyclic voltammograms for ferrocenylated surfaces were examined at a range of scan rates (25 mV s^{-1} – 5 V s^{-1}) and for other surfaces at 100 mV s^{-1}. The silicon electrode for cyclic voltammetry for lowly doped N-type was illuminated with a collimated deep red LED (660 nm, nominal output 1050 mW, Thorlabs part M660L4 coupled to a SM1P25-A collimator adaptor) at a distance of approximately 7 cm to ensure sufficiently fast kinetics to determine the coverage [87]. Electrochemical impedance spectroscopy (EIS) data were collected between 0.1 to 10^6 Hz with the applied working electrode DC potential set to the $E_{1/2}$ as determined by cyclic voltammetry with an AC perturbation of 15 mV. Data for Mott-Schottky plots were collected at a frequency of 10^4 Hz with an AC perturbation of 15 mV scanning between 0.2 V and -1 V in the positive direction for P-type samples and the negative direction for N-type samples.

2.6 Contact angle measurements

Contact angles were measured using a CAM 101 optical contact angle meter (KSV Instruments). Measurements were performed in triplicate using a sessile drop method with 100 μL drop size.

2.7 X-ray reflectometry

X-ray reflectometry was carried out on a Panalytical Ltd X′Pert Pro instrument with a tube source of Cu Kα radiation ($\lambda = 1.54$ Å). The X-ray beam is focused using a Göbal mirror and a fixed slit set to 0.1 mm pre-sample and a parallel collimator post-sample. Data was obtained over an angle of incidence range of 0.05° to 5.00° using 0.01° steps which was measured over a time frame of 1 hour. The measurement was repeated sequentially 16 times to observe any structural changes in the film over time. Only specular reflectivity was measured (i.e. angle of incidence = angle of reflection). The data was reduced so that reflectivity was expressed as a function of scattering vector (Q) which is determined by the following:

$$Q = \frac{4\pi \sin\theta}{\lambda}$$

Where θ is the angle of incidence. The reflectivity was also scaled so that the reflectivity at the critical edge is equal to unity. Data was analysed using the REFNX analysis software [88] which uses an optical matrix method with parameters varied using differential evolution until the lowest possible χ^2 value is achieved. The monolayer is modelled as slab defined by the parameters of thickness, roughness, and scattering length density (SLD) which is determined by the atomic makeup of the monolayer and is defined as:

$$SLD = \frac{\sum_{i=1}^{n} Z_i r_e}{V_m}$$

Where Z_i is the atomic number of the ith atom in n atoms, r_e is the Bohr electron radius (2.818×10^{-5} Å), and V_m is the molecular volume.

2.8 X-ray photoelectron spectroscopy for C, Si, N and O

XPS experiments were performed in a Kratos Axis Supra instrument (Kratos Analytical Ltd). Monochromatic Al K-alpha (1486.6 eV) radiation was used as the excitation source. Spectra were collected in hybrid lens mode, with an excitation power of 225W. The pass energy was set to 160 eV for wide scans using a 1 eV step size and a 200 ms dwell time. The pass energy was set to 20 eV for high resolution windows around core levels, using a 0.1 eV step size and a 200 ms dwell. High resolution scans were repeatedly swept (up to 10 sweeps) until a target figure of merit for signal-to-noise was achieved. The binding energy axis was corrected by rigidly shifting all spectra from a given sample to place the 2p 3/2 peak of elemental silicon at 98.8 eV.

XPS data were analysed using CasaXPS. A Shirley background subtraction was performed then a nonlinear least-squares fit with mixed Gaussian-Lorentzian functions. The C 1s emission region was deconvoluted and fitted with 80% Gaussian and 20% Lorentzian line shapes. The N 1s emission region was deconvoluted and fitted with 100% Gaussian line shapes. The Si 2p emission region was deconvoluted to two peaks and fitted with 95% Gaussian and 5% Lorentzian line shapes [85].

2.9 X-ray photoelectron spectroscopy for Cu

XPS data were acquired using Mg Kα radiation [89]. The apparatus was built by SPECS (Berlin, Germany) with a non-monochromatic X-ray source and has and a base pressure of a few 10^{-10} mbar. The angle between the X-ray source and the analyser is 54.7°. At a pass energy of 10 eV the FWHM of the Ag $3d_{5/2}$ peak is < 1 eV. The uncertainty of the peak positions is typically 0.2 eV. High-resolution scans were recorded at a step size of 0.1 eV for copper at a pass energy of 10 eV. The acquired spectra were calibrated by setting the C 1s peak of C-C sp3 carbon to 285.0 eV. High-resolution XP spectra were fitted with combined Gaussian-Lorentzian peaks with Shirly background subtraction.

Chapter 3 Harnessing silicon facet-dependent conductivity to enhance the direct-current produced by a sliding Schottky diode triboelectric nanogenerator

*Stuart Ferrie, Nadim Darwish, John J. Gooding, and Simone Ciampi,**
S. Ferrie, Dr. N. Darwish, Dr. S. Ciampi
School of Molecular and Life Sciences, Curtin Institute of Functional Molecules and Interfaces, Curtin University, Bentley, Western Australia 6102, Australia
E-mail: simone.ciampi@curtin.edu.au

Prof. J. J. Gooding
School of Chemistry, The University of New South Wales, Kensington, New South Wales 2052, Australia

Adapted from Ferrie, S.; Darwish, N.; Gooding, J. J.; Ciampi, S., Harnessing silicon facet-dependent conductivity to enhance the direct-current produced by a sliding Schottky diode triboelectric nanogenerator. *Nano Energy* **2020,** *78*, 105210. Rights are retained to reuse in a thesis by the authors. An attribution statement is included as Appendix A.

Abstract

Harnessing triboelectricity is a promising form of energy harvesting technology. Unlike conventional triboelectric nanogenerators, which convert friction between insulators into alternating current, a sliding metal–semiconductor contact converts small movements into direct current (d.c.), which can power electronic circuitry without the need of electrical rectification. The zero-bias d.c. output of a dynamic metal–semiconductor contact is assumed to increase linearly with its area, posing restrictions on the miniaturization of this new type of power sources. By implementing silicon surfaces that are electrically heterogeneous, it is found that d.c. outputs are not steady-state, but instead peak when the metal contact slides across concave boundaries between highly and poorly rectifying silicon crystal facets. Sharp lateral changes in electrical rectification, coupled to a concave surface curvature, are more important to maximize current densities than applied normal force or surface friction. These findings help alleviating device-wear issues, as well as removing physical constraints to the miniaturization of sliding-diode nanogenerators.

Graphical Abstract

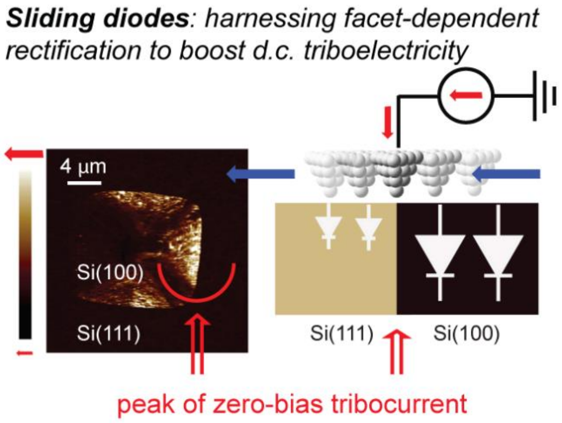
***Sliding diodes**: harnessing facet-dependent rectification to boost d.c. triboelectricity*
4 µm
Si(100)
Si(111)
Si(111)
Si(100)
peak of zero-bias tribocurrent

3.1 Introduction

All electronic devices are powered by direct current (d.c.), commonly supplied by a battery. Batteries need periodic recharging or replacement, but such procedures may not be viable in long-term health monitors and remote sensors in inaccessible places. Where it is not possible to replace or recharge the battery, such as in miniaturized autonomous or remote electronics, converting ubiquitous mechanical vibrations and friction and into electricity is one solution [90]. Ranging from the contraction of a blood vessel to the vibrational energy of an acoustic wave, the environment provides a broad range of mechanical energy sources. However, in a micro-scale setting, the efficient conversion of mechanical energy into electricity remains a challenge. Sliding hands on a rotating evacuated glass globe generate static electricity, and a conventional electrostatic generator exploits this phenomenon to charge conductive plates that are in relative motion but electrically isolated (e.g., by a polymer coating) [91]. This type of charging – contact and separation of dielectrics – being purely capacitive generates an alternating-current output [92]. If used to power electronics, alternating current needs firstly to be rectified (converted into d.c.), for instance, by adding a bridge arrangement of multiple diodes, detracting from any portability advantage [93, 94]. An important conceptual step in the direction of removing the need for downstream rectification was recently achieved by Thundat and co-workers, by means of replacing the capacitive process with a direct charge-transfer process [95]. The authors demonstrated that with no externally applied bias, the lateral movement of the metal contact of a sliding Schottky diode generates a d.c. output [96]. Direct-current triboelectricity – which has so far been reported for Schottky diodes on silicon [95, 97] and MoS_2 [96] – bears the sign of a reverse-bias current. More explicitly, the movement of electrons excited upon friction or mechanical deformation of the junction [98], appears to be guided by the voltage drop inside the semiconductor space charge, such as electrons flowing from a high work function metal contact to a n-type substrate. Published work suggests that on an electrically homogenous semiconducting surface, the magnitude of the zero-bias current collected by a sliding grounded metal contact reaches a steady-state value almost instantaneously [93, 95, 99]. This current output is reported to be a function of the local “static” leakage of the diode. That is, in the absence of an external bias, the triboelectric output is expected to reach a maximum over semiconductor regions showing large reverse bias currents in a static current–voltage measurement [100].

Recent work has pursued scaling up from the AFM scale to macroscale devices with needles as the metal contact [101] which have shown high power densities and even larger contacts have also shown promise [102]. Perovskites have been examined as the semiconducting substrate, which also can capture light as well as mechanical energy [103].

Herein, by using samples that are engineered to be electrically heterogeneous – that is with microscopic domains of poorly rectifying crystal faces surrounded by highly rectifying domains – we demonstrate that lateral electrical contrast and concave surface curvatures, rather than merely large leakage currents, can maximize d.c. outputs. It demonstrates a new approach to minimize device area and wear, and augment zero-bias current harvested from out-of-equilibrium Schottky diodes.

3.2 Results and discussion

Figure 3.1a and b show the topographical characterization by atomic force microscopy (AFM) of silicon samples with (111) facets bordered by (100) planes. Si(100) substrates are structured by anisotropic etching in potassium hydroxide and ammonium fluoride solutions to form protrusions with (111) facets on the surface. These pyramids are scattered across the surface as seen by SEM (Figure 3.2).

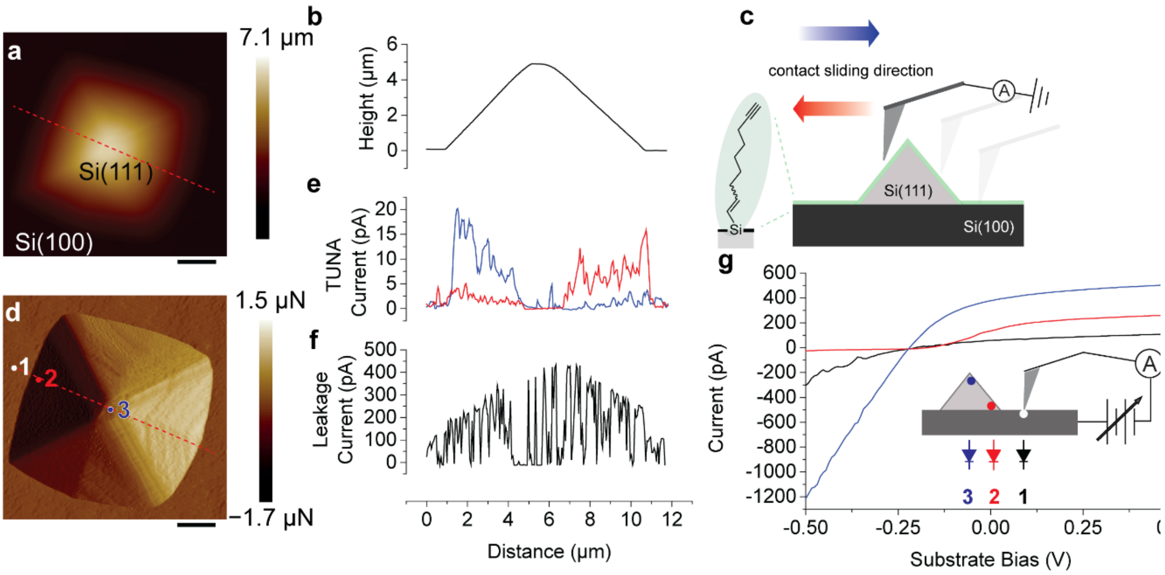

Figure 3.1: Facet-dependent rectification and zero-bias d.c. currents in an out-of-equilibrium Pt–Si diode. a) 12 × 12 µm AFM topographic (height) map of pyramids protruding from flat lowly doped float zone (FZ) n-type Si(100). b) Height profile along the red dotted line shown in (a). c) Schematic of the AFM experiment, with the platinum tip contacting a monolayer coated oxide-free silicon surface. The blue and red arrow indicate the trace (left to right) and retrace direction (right to left), respectively. d) Peak force error map for the retrace direction, showing the actual variation with respect to the 2 µN set-point in the normal force across the sample. e) Zero-bias (0 V) tunneling AFM (TUNA) current profiles for scans along the trace (blue) and retrace (red) directions over the dotted red line shown in both (a) and (d). f) Values of "leakage" reverse-bias (+0.125 V) current, obtained from static current–potential (I–V) curves sampled at 200 evenly spaced points (58.6 nm spacing) along the red dotted line shown in (a). g) Schematic of the sample to tip bias routing and representative I–V curves sampled at point ***1*** *on Si(100), close to the (100)/(111) boundary at point* ***2*** *on Si(111), and at point* ***3*** *on Si(111) but further away from the (100)/(111) boundary. Forward currents appear in the negative quadrant, that is, when the Si is biased negative with respect to the tip. Leakage currents are generally lower at the pyramid base, while rectification ratios (not shown) do not track the pyramid profile as forward currents are generally very disperse. Scale bars in (a) and (d) are 2 µm.*

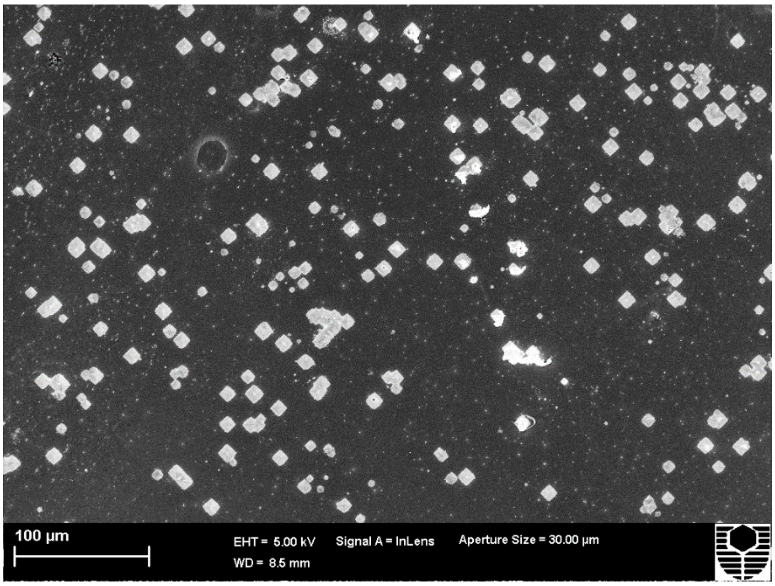

Figure 3.2: SEM imaging of a Si(100) surface with protruding Si(111) pyramids. The substrate is n-type (phosphorus-doped) FZ Si(100) of 8–12 Ω cm resistivity. SEM images were recorded using a Zeiss Neon 40EsB FESEM equipped with a Schottky field emission gun operating at 5 kV and a chamber pressure of approximately 4 × 10^{-6} mbar.

The design of this system was inspired by the recent finding of facet-dependent conductivity in silicon crystals. Measurements with tungsten probes have indicated different electrical conductivities for different silicon facets ((111)>(100)) [104], with similar trends also reported for Cu_2O crystals [105]. To prevent anodic decomposition of the non-oxide semiconductor we coated the hydrogen-terminated silicon with a monolayer of 1,8-nonadiyne (Figure 3.1c) [106]. The monolayer-coated and electrically heterogeneous silicon (111)/(100) platform overcomes the hurdle of the random electrical fluctuations in MoS_2 [96], enabling direct measurements of the links between local characteristics of the metal–semiconductor contact (static biased systems) and 2D distribution of the tribocurrents (zero-bias sliding diode). The AFM PeakForce Tunneling (PF-TUNA™) setup used in this study is selected to ensure precise control of contact force (Figure 3.1d) and to reduce as much as possible lateral forces (friction). Zero-bias PF-TUNA™ current data shown in Figure 3.1e demonstrate that the continuous lateral movement of the Schottky contact – the large work function platinum AFM tip sliding across a float zone (100)/(111) n-type Si sample (Figure 3.1c) – leads surprisingly to spikes of positive currents rather than a steady-state output.

There are no wear tracks detected by AFM (Figure 3.3), and the maximum d.c. output is consistently localized near the pyramid base, indicating that a static electrification of the "fissile crack" type [107] is not playing a significant part in this triboelectric process. Further, based on the absence of an evident oxidative damage (Figure 3.3) the emission of electrons upon an exothermic reaction [108], such as upon the silicon substrate oxidizing to silica [105], is also ruled out.

Another hypothesis ruled out is that there is a large difference in the monolayer properties between the (100) and (111) facets as determined by X-ray reflectometry. The scattering length density (SLD) of a 1,8-nonadiyne-derived monolayer on Si(111) is 10.5×10^{-6} Å^{-2} compared to previous reports of the SLD of a 1,8-nonadiyne-derived monolayer on Si(100) of 10.4×10^{-6} Å^{-2} [109]. The SLD of a monolayer is related to the physical density of it, implying a similarly dense monolayer on (100) and (111) facets.

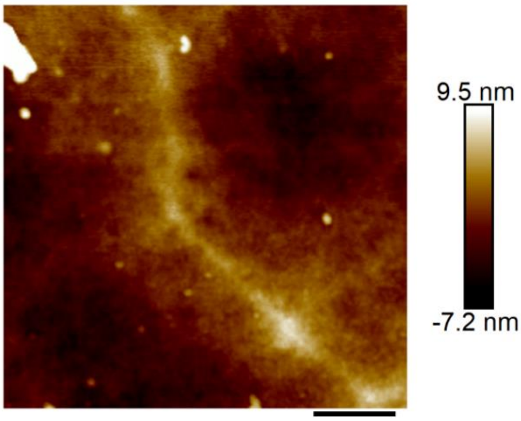

Figure 3.3: No visible wear tracks. AFM topography (height image) data acquired within one side of a Si(111) pyramid etched on a Si(100) wafer (CZ substrate, 8–12 Ω cm, n-type, phosphorus-doped). Data recorded in tapping mode using TESPA-V2 tips after prolonged tribocharging measurements (10 scans in PF-TUNA mode at a Peak Force set-point of 2.000 µN, with line spacing of 58.6 nm). The height image was acquired at a scanning rate of 0.996 Hz. The scale bar is 200 nm and no wear tracks are visible at this scale. Unless otherwise specified, all samples of this study are monolayer-coated (1,8-nonadiyne) hydride-terminated silicon surfaces.

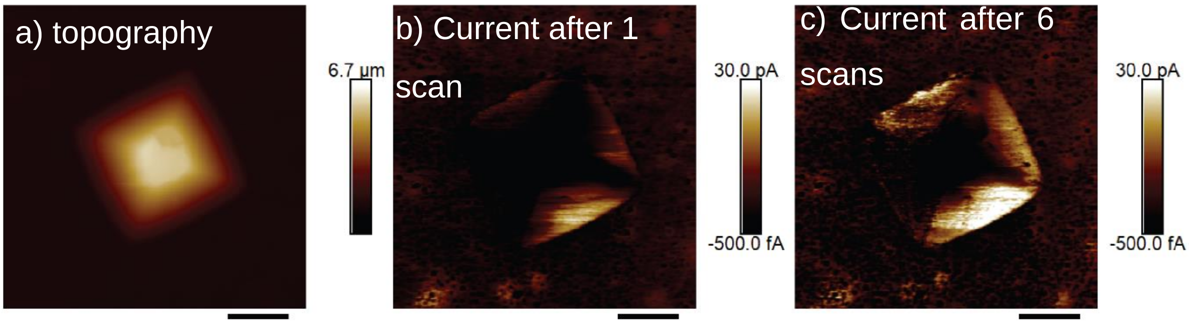

Figure 3.4: Sustained zero-bias d.c. output after repeated sliding experiments. On the time scale of these experiments, the decline in tribocurrents is negligible. Repeated zero-bias current imaging of Pt–Si sliding diodes on Si(100) substrates (CZ wafers, 8–12 Ω cm in resistivity, n-type, phosphorus-doped) etched to expose Si(111) pyramids. a) Height sensor image. b) TUNA current map after 1 scan. c) TUNA current map after six scans. The Peak Force set-point is 2.000 µN, the scan rate 0.894 Hz, and scale bars are 5 µm. Imaging is in PF-TUNA mode

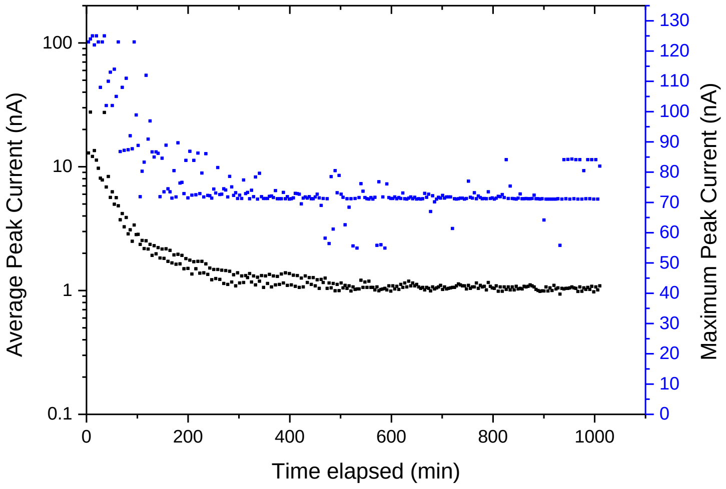

Figure 3.5: Average Peak current (black) and maximum Peak Current (blue) continuously imaged on the same area over a 18h period on a Si(111) pyramid prepared on lowly doped (8–12 Ω cm) n-type FZ (100) silicon with a Ga/In eutectic on copper tape back contact with 15 × 15 µm area with 256 sampling points per line over 256 horizontal lines.

Further experiments to examine the short-term and long-term stability and resistance to fatigue of this setup are in Figure 3.4 and Figure 3.5. This last point is reinforced by the absence of a significant decline in the triboelectric response during consecutive measurements repeated over the same sample area (Figure 3.4). A thermoelectric effect leading to a tribocurrent in silicon is ruled out based on previous reports [100]. Further, the pressure applied by the AFM tip on the silicon surfaces is estimated (DMT model [50]) to be 18.8 GPa, a contact loading that is below the 19.5–20 GPa required in silicon to promote a phase change from semiconductor (Si-I phase) to conductor (Si-II phase) [110]. We therefore conclude that the semiconductor bands remain bent downwards, and the built-in voltage of the platinum–silicon junction is acting to separate electron and hole pairs generated in the semiconductor upon deformation [111] or frictional damage [112]. The data in Figure 3.1e show tribocurrents discharging at the base of (111) pyramids in the form of electrons flowing from the dynamic platinum contact to the n-Si substrate. This zero-bias current peaks when the platinum contact has crossed over the (100)–(111) boundary coming from (100) regions. Force error maps and TUNA current profiles (Figure 3.1d and e, respectively) indicate a constant force across a (111) pyramid face (Figure 3.6), but a monotonically decreasing current output as the tip slides away from the boundary. This localization of spikes in the zero-bias current is not evident in smaller (~50 nm in width) pyramids (Figure 3.7), and becomes undetectable in flat silicon samples (Figure 3.8). Surprisingly the tribocurrent does not reach a maximum at a convex site as expected from Gauss's law which implies a greatest electrical field at a point of highest convexity, nor it tracks, as expected from prior work with MoS_2 [96], the substrate leakage. Instead the tribocurrent is highest at the boundary between (100) and (111) facets.

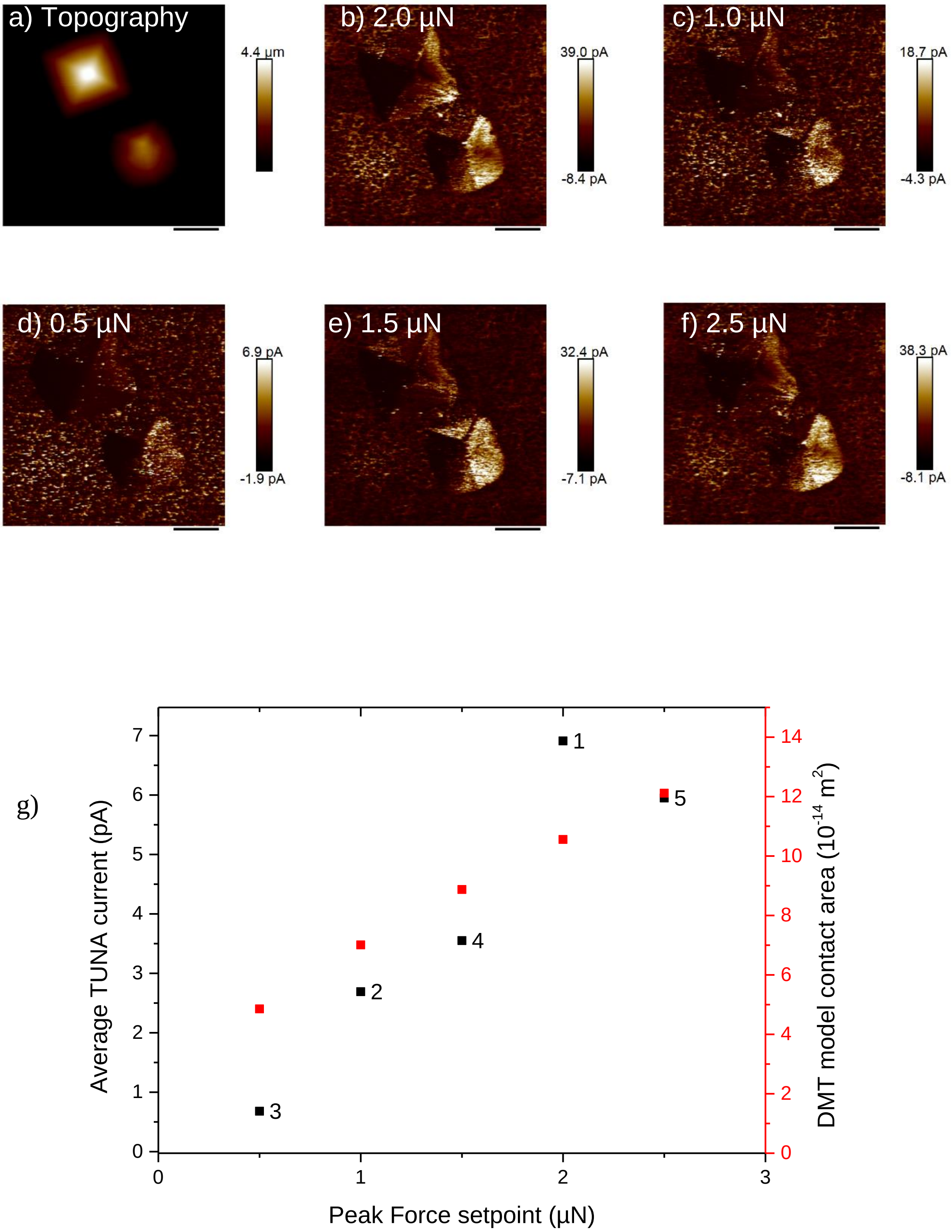

Figure 3.6: Normal force and current. (a) Topography image of Si(111) pyramids prepared on lowly doped (8–12 Ω cm) n-type FZ (100) silicon with a carbon tape back contact. (b-f) Current images at a scan rate of 20 µm/s. These images are in order of scanning, rather than order of applied force. Peak Force setpoint of (b) 2.0 µN (c) 1.0 µN, (d) 0.5 µN, (e) 1.5 µN and (f) 2.5 µN. Scale bars are 4 µm for all images. g) Graph showing Peak Force setpoint versus average TUNA current across

the image and the contact area as calculated by the DMT model as in Section S1. Points are numbered in the order they were imaged.

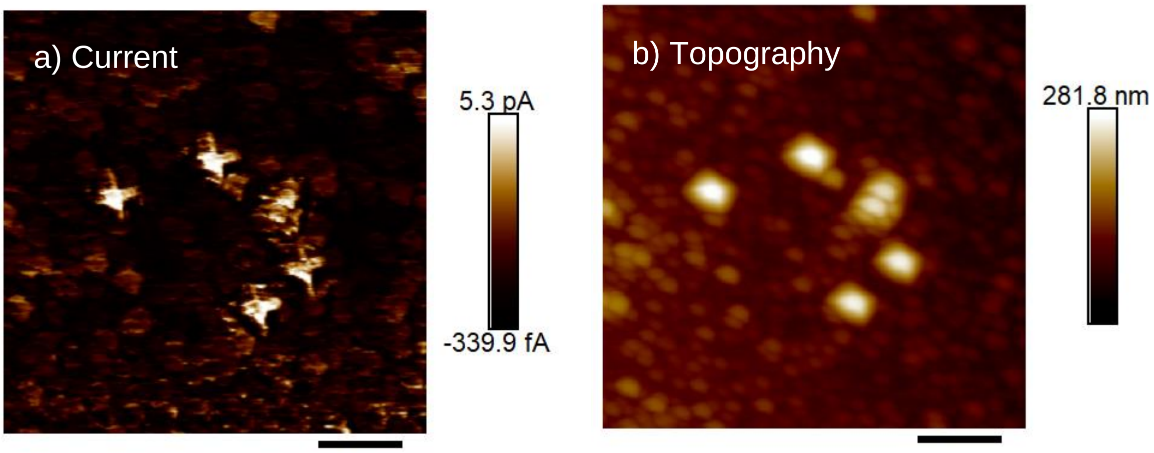
a) Current
5.3 pA
-339.9 fA
b) Topography
281.8 nm

Figure 3.7: Zero-bias current output from sliding diodes on small pyramids. Si(100) CZ samples (8–12 Ω cm resistivity, n-type) etched for 60 min etch in potassium hydroxide solutions, without any isopropyl alcohol, to generate small Si(111) pyramids. The Peak Force set-point is 0.5482 µN, the scan rate 1.00 Hz, and scale bars are 100 nm. Images acquired in PF-TUNA mode. a) Height sensor image. b) TUNA current image.

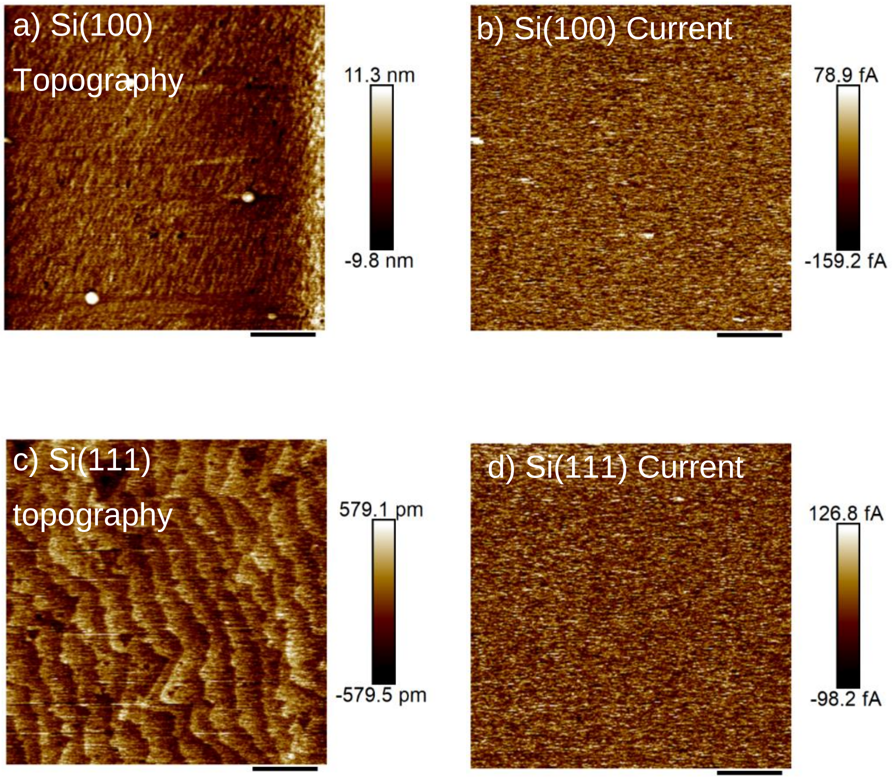
a) Si(100)
Topography
11.3 nm
-9.8 nm
b) Si(100) Current
78.9 fA
-159.2 fA
c) Si(111)
topography
579.1 pm
-579.5 pm
d) Si(111) Current
126.8 fA
-98.2 fA

These two points warrant a further discussion. Firstly, the current does not peak on the pyramid apex (Figure 3.1e). Charges spread as much as possible across a conducting surface, with the result that charging an object that is neither a perfect plane, or a perfect sphere, leads to large charge densities where the radius of the surface curvature is small: a relatively small amount of charge at the tip of an asperity leads to a large electric field outside the solid [113]. Surprisingly the zero-bias d.c. signal peaks on the side of the Si(111) pyramid, in proximity of the concave (111)–(100) plane intersection, and not in correspondence of the convex (111)–(111) apex. We stress that the current is not a dielectric break down of air as shown by high-speed current data capture (Figure 3.9).

Figure 3.8: Negligible d.c. output from sliding Pt–Si diodes on flat surfaces. a,b) Si(100), and c,d) Si(111) surfaces (CZ phosphorus-doped wafers, 8–12 Ω cm). All surfaces are monolayer-protected but non-structured, that is, prepared without the KOH and second NH_4F etches. The Peak Force set-point is 2.000 µN, the scan rate 0.988 Hz, and scale bars are 2 µm. Samples are imaged in PF-TUNA mode. a,c) Height sensor images. b,d) TUNA current images.

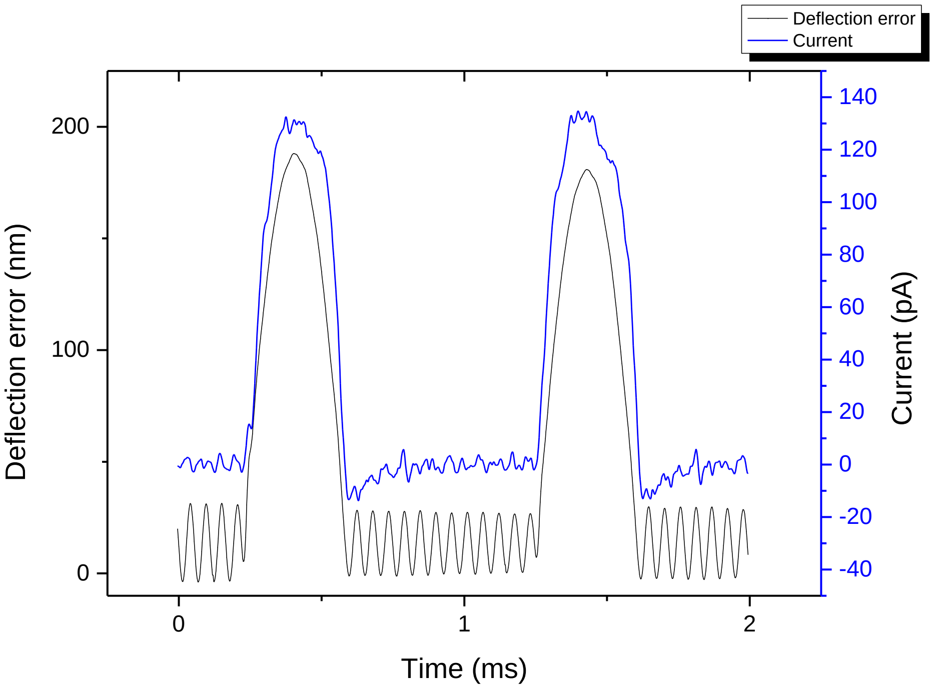

Figure 3.9: High-speed capture current data. The current peaks while the Pt AFM tip is contact with the silicon surface while there is only a small dielectric breakdown between the surface and tip immediately after the tip has left contact with the

surface. The TUNA current is the average of the raw current over each tip contact cycle. AFM data acquired on FZ n-type Si(100) samples (8–12 Ω cm). Peak Force set-point was set to 2.000 µN, the scan rate to 0.894 Hz, and the deflection error and raw current are sampled at 500 kHz over two cycles of tip–surface contact.

Secondly, a detailed analysis of current–potential (*I–V*) curves acquired with high 2D resolution reveals that the d.c. output, which bears the sign of a reverse current, does not match the leakage map of the surface (Figure 3.1f). This analysis, which requires reproducible and spatially resolved *I–V* curves (Figure 3.1g), is only possible because all our samples were chemically passivated with a Si–C-bound organic monolayer [106]. Oxide-free silicon surfaces rapidly oxidize in air to form an insulating layer of silica [96], and in such samples *I–V* measurements were of little value in trying to extract a relationship between static leakage and dynamic zero-bias reverse currents.

The coordinates of the *I–V* sampling points were generally selected such to investigate: i) (100) regions where the zero-bias current is negligible (point **1**, Figure 3.1d); ii) (111) pyramid facets where high zero-bias currents are measured (point **2**); and iii) pyramids, but in correspondence of regions of low d.c. output (point **3**). I–V curves at point **1** show lower current in both the forward and reverse biases than at points **2** and **3**. As noted above, the zero-bias current peaks as soon as the platinum contact, sliding at about 20 µm/s, crosses over from a low-leakage (100) area (point **1** in Figure 3.1d) into a (111) pyramid facet. The discharge of the dynamic current (point **2** in Figure 3.1d), bearing the direction of a leakage process, does however not reach a maximum in correspondence of those regions of largest static leakage (e.g. at point **3** in Figure 3.1d), but rather at the concave boundary between sites of high and low electrical rectification. Electrical heterogeneity alone, as shown by the poor tracking of the leakage and TUNA currents is not linked to any spike of d.c. output. Contrast between the low leakage (100) plane and the leaky and tilted (111) surface appears to maximize the efficiency of charge excitation and extraction upon pressure.

We remark that the use of the term "tribocurrent" without a clear evidence of a link between friction and current output can be misleading. Friction between objects originates (and/or is caused) in part from electronic interactions [114, 115]. Electron/hole pairs form to damp phonons generated when lateral forces are required to slide objects laterally [116, 117]. As we noted above, one advantage of Peak Force AFM experiments is that the normal force is precisely controlled while the lateral force, if not entirely removed, is certainly minimized. Nonetheless, we performed control experiments in AFM contact mode where lateral forces acting on the platinum sliding contact are measured and mapped across the sample, simultaneously with the zero-bias current (Figure 3.10). By changing the chemical nature of the protective monolayer, specifically by adding a primary amine at the monolayer distal end

[118], surface friction was deliberately increased. Current and friction AFM maps in Figure 3.10 reveal that there is no direct correlation between zero-bias current and friction, and surprisingly the lower current was found for the surfaces with larger friction coefficients.

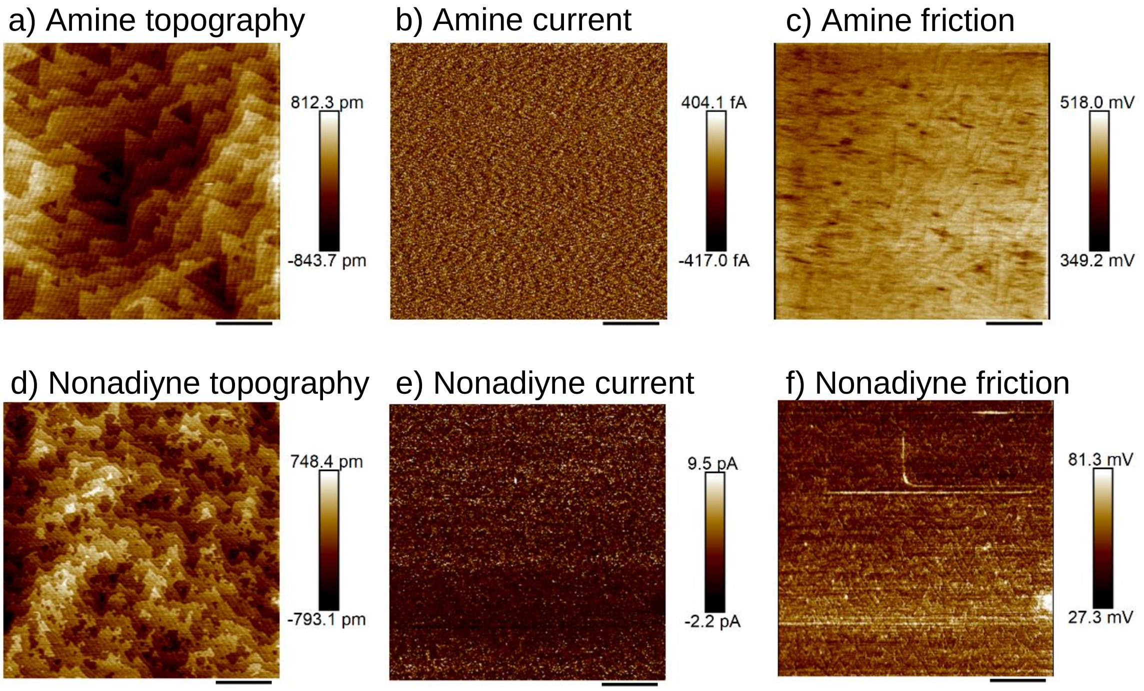

Figure 3.10: Conductive lateral force microscopy. Contact mode conductive AFM with the sample scan angle set to 90° for all images to obtain friction data. Samples are CZ Si(111) wafers, p-type (boron), 8–12 Ω cm. The deflection set-point was set to 400 nN for all images. Scale bars are 1 µm. a–c) 3-azidopropan-1-amine treated (click reaction) surfaces, showing increased friction and decreased current versus (d–f) 1,8-nonadiyne surfaces. a,d) Height sensor images. b,e) TUNA current images. c,f) Friction loop (retrace image minus trace image then divided by a factor of two. The difference in the lateral forces in the retrace versus the trace image corresponds to twice the friction force).

The electronic component to friction [119] remains highly debated: previous work by Nakayama showed essentially no correlation between friction and excitation of electrons in conductors, semiconductors and insulators under mechanical stress [112], while Salmeron and co-workers reported increases in sliding friction for GaAs surfaces biased into accumulation [115]. What is apparent on featureless flat substrates is that the normal force applied by the metal AFM tip on the silicon lattice, and not the lateral friction, is the main driver of electron excitation leading to a zero-bias current, possibly involving transient changes in carrier mobility [120].

Previous studies of macroscopic Pt–Si Schottky diodes under strain have revealed changes in their electrical properties compared to unstrained junctions. For n-type silicon, the Schottky barrier decreases with increasing stress [121]. Furthermore, a concave curvature in n-Si is known to lead to a thinner space charge [122], which, for instance, accounts for the formation of porous silicon under anodic etching instead of an homogeneous thinning of the silicon electrode [123].

This relationship between the width of the space charge barrier and surface curvature, in conjunction with the effect of pressure on the barrier height, appear to account for the localization of the d.c. maxima at the concave (100)–(111) boundary. But again, curvature alone is not sufficient (Figure 3.11) and the contrast in the "static" leakage between the (100) and (111) facets remains a key factor to maximize the current output.

a) Topography b) Trace current c) Retrace

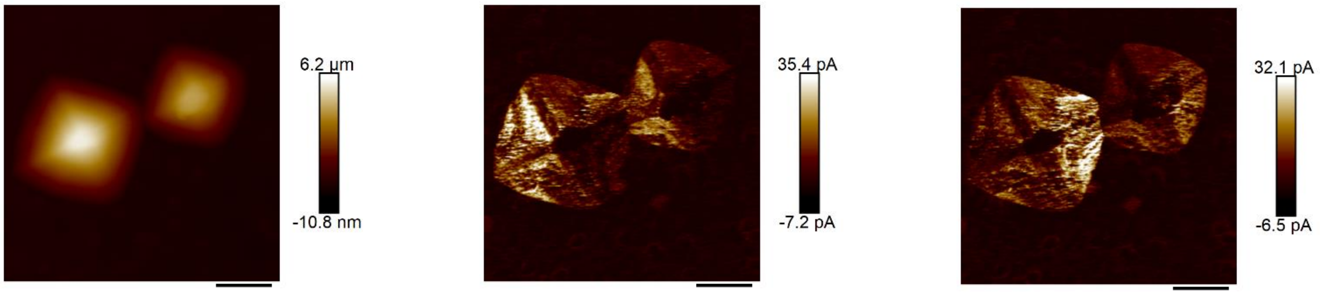

Figure 3.11: Joined pyramids showing no enhancement of current at Si(111)–Si(111) junctions. Zero-bias current imaging of Pt–Si sliding diodes on Si(100) substrates (FZ wafers, 8–12 Ω cm in resistivity, n-type (phosphorus-doped)) etched to expose Si(111) pyramids. a) Height sensor image. b) TUNA current map in trace direction (left to right). c) TUNA current map in retrace direction (right to left). The Peak Force set-point was set to 2.000 µN, the scan rate is 0.894 Hz, and scale bars are 2 µm. Imaging is in PF-TUNA mode.

current

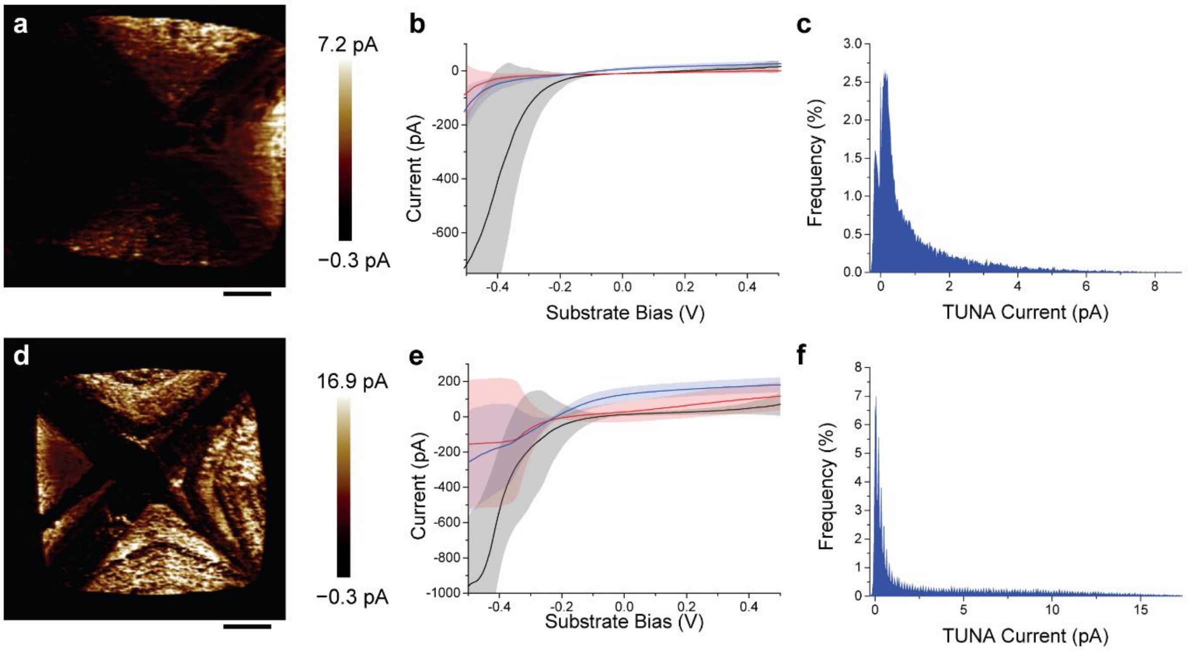

Figure 3.12: Zero-bias current increases with the minority carriers' mobility. Current output from sliding Schottky diodes (Pt–Si) on lowly doped (8–12 Ω cm) CZ (a–c) and FZ (d–f) n-type silicon. a,d) 12 × 12 µm AFM electrical data (TUNA retrace maps) showing higher currents close to the (100)–(111) boundary. b,e) Current–potential (I–V) curves acquired either on planes of Si(100) (black trace), on the Si(111) pyramid where low current is observed (red), and on the Si(111) pyramid where high current is observed (blue). Lines indicate the mean current from I–V curves recorded at ten sampling points, with each location sampled five times (from positive to negative) with the shaded area corresponding to one standard deviation. c, f) Histograms showing the relative frequency of the current value in the TUNA current image. Scale bars in (a) and (d) are 2.0 µm.

The zero-bias current of our sliding rectifiers has the sign of a reverse current and is therefore the sum of the hole and electron currents flowing over and under the barrier. If the barrier is sufficiently high, as is expected from the 0.79 eV difference in work functions between platinum and n-type silicon [124], the reverse current is mainly due to diffusion of minority carriers under the barrier, and therefore the d.c. output would depend critically on the carrier's lifetime. To test this hypothesis we compared zero-bias d.c. outputs between Czochralski (CZ) and float zone (FZ) silicon substrates (Fig. 2), where due to the lower concentration of oxygen impurities, the diffusion length and lifetime of holes is much greater in the latter (FZ) [125]. FZ and CZ silicon crystals show similar trends of tribocurrent localization near the (100)–(111) boundary (Figure 3.12a and d), they both showed largest static leakage over sites of high dynamic output (Figure 3.12b and 2e). The magnitude of the current being significantly greater in FZ junctions with a longer hole lifetime is consistent with our hypothesis that the reverse current is mainly due to the diffusion of minority carriers.

Data in Figure 3.12 illustrate another important point, the zero-bias current is not akin to an electron "pump", where the normal force induces a negative forward current that removes electrons from (100) regions which is then balanced by a positive backward current when the metal tip reaches "leaky" (111) facets. This pump-like mechanism could rely on exoelectron emission triggered by mechanical stress [107], but although this may happen to some small extent, it is largely ruled out upon an analysis of the current histograms in Figure 3.12c and f. In the (100) regions, a small positive current is observed, however it is much lower in magnitude to the (111) regions. The net balance is not zero, with an overall significant measurable excess of forward-biased currents.

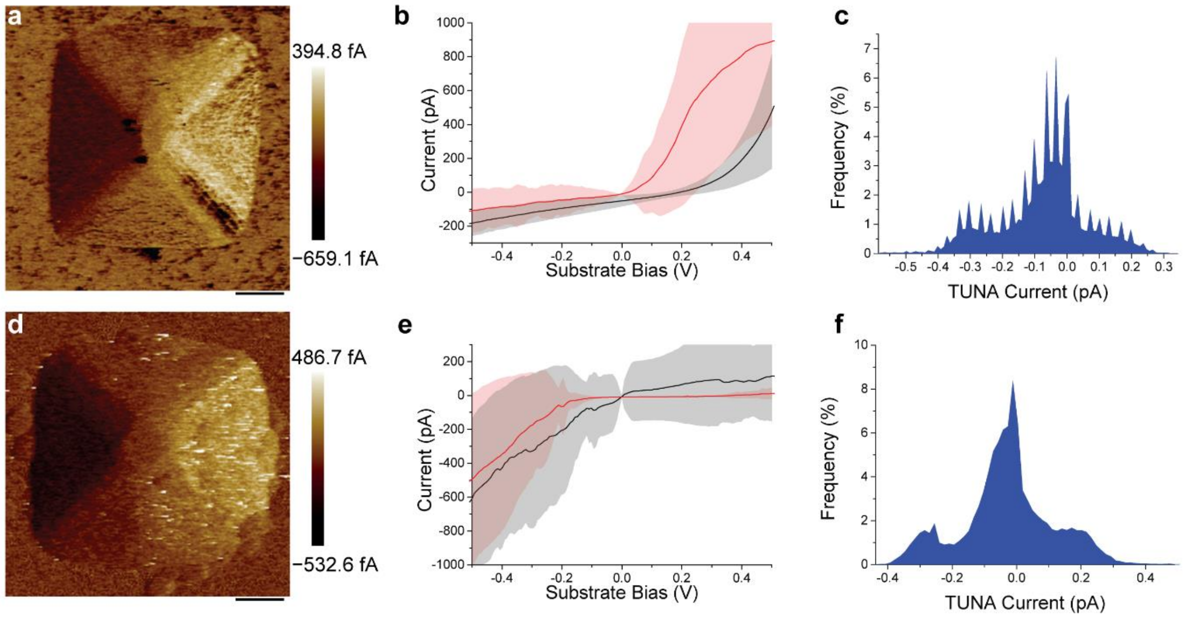

Figure 3.13: Doping and zero-bias output. Current output from sliding Schottky diodes (Pt–Si) on lowly doped (8–12 Ω cm) CZ p-type (a–c), and on highly doped (0.007–0.013 Ω cm) CZ n-type (d–f) silicon. a,d) 12 × 12 µm AFM electrical data (TUNA retrace maps) showing higher currents close to the (100)–(111) boundary. b,e) I–V *curves acquired either on planes of Si(100) (black trace) and on the Si(111) pyramid (red). Lines indicate the mean current from* I–V *curves recorded at ten sampling points, with each location sampled five times from positive to negative with the shaded area corresponding to one standard deviation. c,f) Histograms showing the relative frequency of the current value in the TUNA current image. Scale bars in (a) and (d) are 2.0 µm.*

In contrast to lowly doped n-type silicon, lowly doped p-type and highly doped n-type yield a much smaller current (Figure 3.13a and b). Whilst for lowly doped n-type silicon, the on-pyramid and off-pyramid *I–V* curves are well distinct (Figure 3.13b), this contrast is absent in highly doped n-type (Figure 3.13e). For highly doped n-type, the facet dependence of the diode properties is weaker than for lowly doped n-type. Compared to lowly doped n-type, the histogram is more symmetrical around 0 pA, however there is still a small positive current. For lowly doped p-type, the diode is oriented in the opposite direction. There is a small total negative current compared to the n-type surfaces (Figure 3.13a and c). In contrast to the *I–V* curves of lowly doped n-type silicon, the curves at 0 V for Si(111) are close to the origin, while there is a measurable negative current at 0 V for the Si(100) curves. This agrees with the increased negative tribocurrent on the Si(100) surfaces over the Si(111) surfaces.

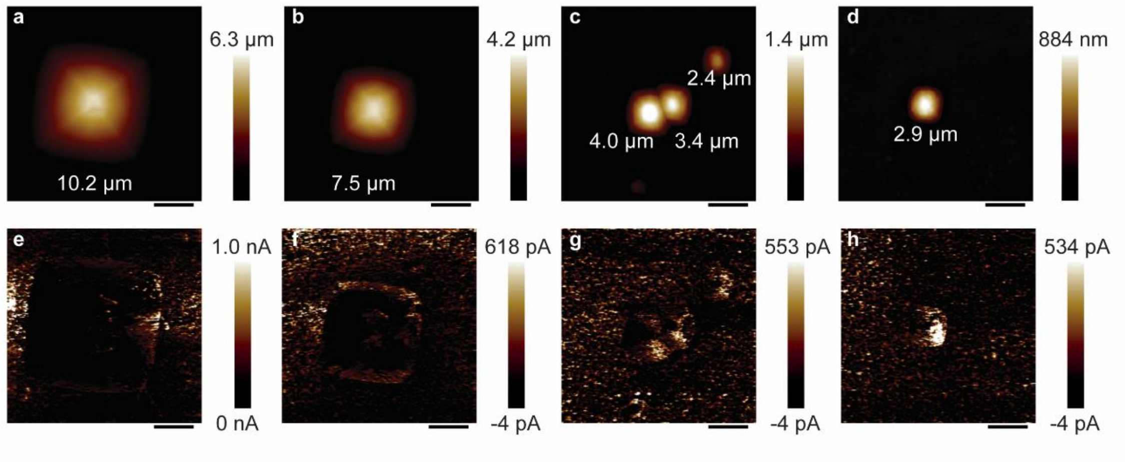

Figure 3.14: Pyramid size and zero-bias current magnitude and localization. (a–d) Topography images of Si(111) pyramids of various sizes prepared on lowly doped (8–12 Ω cm) n-type FZ (100) silicon. The width from top edge to bottom edge is displayed for each pyramid. (e–h) Current images (retrace TUNA current) showing localization of the d.c. current maxima at the pyramids' edges. Such localization is less appreciable in the smaller pyramids (h). Scale bars are 3.0 µm.

We note that despite our primary purpose being to define the links between electrical heterogeneity and d.c. outputs (i.e. localization of tribocurrent maxima), we carried out experiments to further maximize currents. This was primarily intended so to benchmark our outputs against other research in this field. To this end, series resistance was minimized by replacing the carbon tape back contact with gallium–indium eutectic on copper tape, while using lowly doped, n-type FZ silicon wafers (Figure 3.14). Data shown in Figure 3.15 on the same pyramid as in Figure 3.14a and e reveal that the highest Peak Current – the current measured when the tip contact is at the highest force in the tapping cycle, which is different to the TUNA current, which is the current over the entire tapping cycle – being obtained was 30.6 nA, which considering a contact area of 1.06×10^{-13} m^2 (DMT model[50]) gives rise to a current density as high as 2.9×10^5 A m^{-2}. This value is comparable to the values recently reported for Schottky diodes on silicon without 1,8-nonadiyne[97, 101], highlighting the importance of lateral electrical heterogeneity and of protection of silicon with a thin organic monolayer. Finally, while smaller pyramids show in general lower currents (Figure 3.14), the localization of d.c. tribocurrent maxima current at the edges of pyramids is a general feature independent of the pyramid size. However in general, a larger and more localized current is seen with larger pyramids.

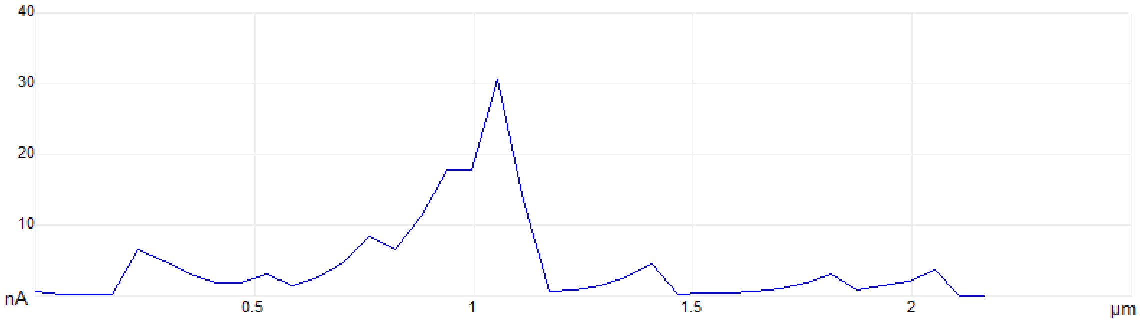

Figure 3.15: Peak Current (current when the tip contact force is highest) trace showing a maximal current of 30.6 nA on Si(100) FZ wafers, 8–12 Ω cm in resistivity, n-type (phosphorus-doped) etched to expose Si(111) pyramids. Back contact is with a gallium/indium eutectic on copper tape.

We stress on the inverse relationship between the curvature of the contact and the d.c. output of a sliding diode. Analogously to the findings on MoS_2 by Thundat and co-workers in reference [7], a 3800 fold increase in the size of the platinum–silicon contact, here achieved by means of rolling a macroscopic 3 mm platinum sphere, resulted in current densities dropping by at least three orders of magnitude. It follows that one viable path of scaling up this form of energy technology is to use sliding contacts made of multiple tips or presenting multiple sharp asperities.

3.3 Conclusion

The full spectrum of chemical, mechanical and electronic factors at play in defining the zero-bias output of an out-of-equilibrium diode is still unclear, but this work provides explicit evidence that the dynamic phenomenon of direct-current triboelectricity is maximized (in this work 2.9×10^5 A m^{-2}) at concave sites separating semiconductor domains of significantly different (static) electrical leakage. Harnessing the facet-dependent conductivity, recently reported for several semiconductors [126], will be one way to engineer two-dimensional surface conductivity, which here we have shown to weight more on zero-bias d.c. currents than vertical and lateral (friction) forces. These findings indicate a target for miniaturizing, and minimizing wear, of this new type of autonomous power sources.

3.4 Acknowledgements

S.C., N.D. and J.J.G acknowledge support from the Australian Research Council (grants no. DP190100735, FT190100148).

Chapter 4 Sliding Silicon-based Schottky diodes: Maximizing Triboelectricity with Surface Chemistry

Stuart Ferrie[a], Anton P. Le Brun[b], Gowri Krishnan[c,d], Gunther Anderson[c,d], Nadim Darwish[a], Simone Ciampi[a,*]

[a] School of Molecular and Life Sciences, Curtin University, Bentley, Western Australia 6102, Australia
[b] Australian Centre for Neutron Scattering, Australian Nuclear Science and Technology Organization (ANSTO), Lucas Heights, New South Wales 2234, Australia
[c] Flinders Institute for Nanoscale Science and Technology, Flinders University, Adelaide, South Australia 5042, Australia
[d] Flinders Microscopy and Microanalysis, College of Science and Engineering, Flinders University, Adelaide, South Australia 5042, Australia

Adapted from Ferrie, S.; Le Brun, A. P.; Krishnan, G.; Andersson, G. G.; Darwish, N.; Ciampi, S., Sliding silicon-based Schottky diodes: Maximizing triboelectricity with surface chemistry. *Nano Energy* **2022,** *93*, 106861. Rights are retained to reuse in a thesis by the authors. An attribution statement is included as Appendix B.

Abstract

Triboelectric nanogenerators are an emerging energy technology which harvests electricity from mechanical energy. Within this technology there are sliding metal–semiconductor contacts, which can be miniaturized, and having a direct current (DC) output are suitable as autonomous power source for electronic devices. Herein we explore the scope of engineering the surface chemistry of silicon towards maximizing the output of a Pt–Si Schottky diode-based triboelectric nanogenerator. Through the attachment of covalent Si–C-bound organic monolayers we have engineered silicon surface chemistry to systematically tune friction, wettability and surface work function, with the overall aim of clarifying the interplay between mechanical and electronic properties defining the DC output of a zero-bias sliding Schottky diode. Current outputs increase two-fold in amine- and alcohol-terminated monolayers compared to shorter and carbon-terminated films. This trend parallels the change in friction measured in response to surface functionalization. A pronounced effect of silicon doping on friction and current was revealed by atomic force microscopy, indicating a link between doping and friction, even at zero applied bias. This work reveals an electrical component of friction by demonstrating a friction excess in response to the flow of current, and it opens up novel avenues into the use of silicon, and its surface chemistry, as platform for triboelectric nanogenerators.

4.1 Introduction

Energy generation is one of the great challenges for the 21st century. An increasingly delocalized demand for the Internet of Things presents us with a further challenge for small, on-demand power supplies. Triboelectric nanogenerators (TENGs) are a promising future power source [127], with a wide range of variants being developed [128-133]. The generation of DC electricity is particularly advantageous as most devices require DC power. In this context, Si-based triboelectricity is rapidly gaining momentum as it has the potential to open up an entirely new and fundamental area in energy and semiconductor research, which will benefit from established surface chemistry methods that are available to control the rectifying "diode-like" properties of static semiconductor junctions [105, 106, 134-136].

As the generation of energy in moving Schottky diode-based TENGs occurs at a metal–semiconductor interface, it follows that the ability to control the surface chemistry of metal and semiconductor, ideally with molecular precision [137, 138], can be a viable path to a more efficient harvesting of friction into electricity. This work aims to define the role of silicon surface chemistry on the current output and friction of a sliding Schottky contact. The ultimate technological goal is that of defining the silicon surface chemistry that yields the largest current output while under minimal friction. The latter requirement – minimal friction – will undoubtedly promote device longevity. As the relationship between doping and friction remains poorly understood [115, 139], the role of silicon doping level and type, on both friction and surface reactivity, was also explored. Previous work on the tribovoltaic effect indicates that friction creates electron–hole pairs, which are then separated by the built-in voltage of the metal–semiconductor junction [82, 102, 140, 141]. Friction has been observed to vary between metal–semiconductor contacts depending on the identity of the metal [142], which has also observed to affect current outputs [73]. The bulk electrical properties of the substrate have been linked to the friction on silicon and GaAs surfaces, with excess friction being shown for substrate forced by an external bias into accumulation [54, 115, 139, 143]. These observations potentially suggest a relationship between friction and current output of a Schottky diode-based TENG, but a deeper investigation is required since, in the first place, the zero-bias DC output of a sliding Schottky diode is often in the direction of a depletion, and not accumulation, current, as seen in Chapter 3.

The chemical and physical properties of a silicon surface, from charge transfer to friction and adhesion [106, 144-146], can be widely tuned by the attachment of an organic monolayer bearing specific chemical functionalities [137, 138]. Hexadecylsilane-derived monolayer islands grafted on silica on highly-doped N-type silicon showed lower friction than the surrounding unmodified surface [147]. The incorporation of similar octadecylsilane-derived monolayers in a micromotor was also shown to reduce friction [148], and the choice of a suitable monolayer terminal group increases friction by favouring hydrogen bonding between two contacting surfaces [58]. However, the use of organic monolayers in TENGs is still in its infancy, with limited examples available for metal–monolayer–metal [149] and metal–monolayer–semiconductor [150] sliding junctions.

In this work we explore the scope, in silicon-based TENGs, of covalently grafted organic monolayers bearing a range of terminal groups. The monolayers are Si–C-bound on oxide-free (hydrogen-terminated) silicon by means of hydrosilylation chemistry which was also used in Chapter 3. This surface chemistry approach is opposed to conventional silane chemistry (Si–O–monolayers) that requires an oxidized, hence partially electrically insulating substrate. This is important as hydrosilylation chemistry allows a broader tuning of surface properties, including control of monolayer thickness, stability of the surface chemistry [151], as well as tunable and reproducible charge transport across the interface [152].

Hydrosilylation of a di-alkyne monolayer-forming molecule (1,8-nonadiyne), and subsequent Cu-catalyzed azide–alkyne cycloaddition (CuAAC) reactions on the base monolayer [151, 153], were used to impart the silicon surface with a range of terminal functionalities (Figure 4.1). The chemically modified silicon surfaces were then characterized by X-ray and ultraviolet photoelectron spectroscopies (XPS and UPS), X-ray reflectometry (XRR), cyclic voltammetry (CV) and contact angle (CA) measurements. Current and friction of sliding Schottky diodes prepared with these surfaces (silicon–monolayer–platinum sliding contacts) were studied by conductive atomic force microscopy (C-AFM), with emphasis on current and friction being evaluated in the absence of any external bias.

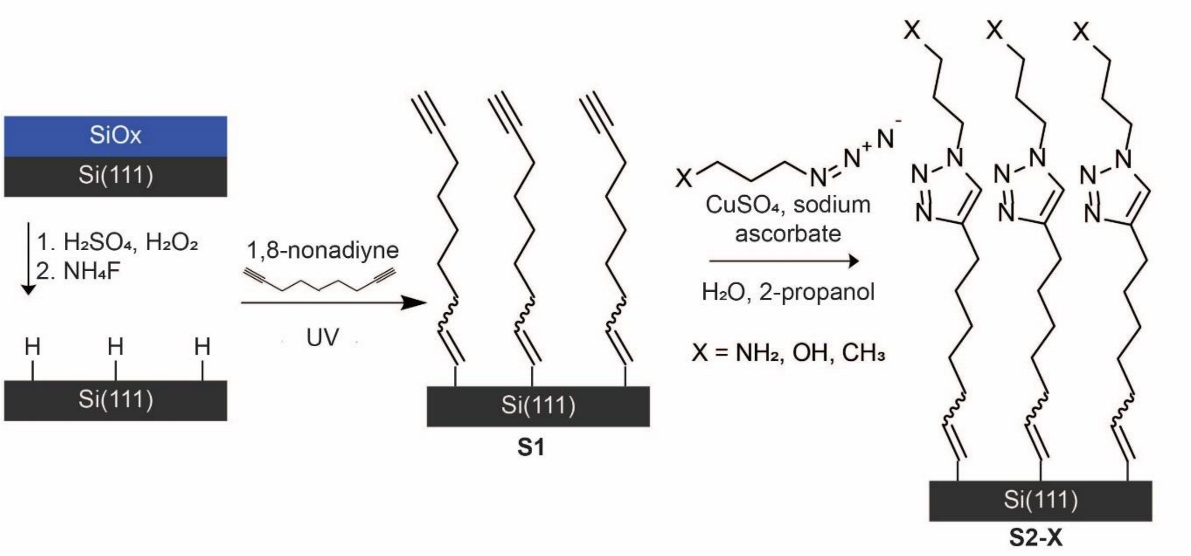

*Figure 4.1: Silicon surface preparation. Schematics of the surface functionalization strategy. Native oxide is first cleaned and etched (1,2) to form a hydrogen-terminated surface. This surface is reacted under UV with 1,8-nonadiyne to form surface **S1**. The terminal acetylene functionality of **S1** is reacted through a CuAAC reaction to covalently attach either 3-azidopropan-1-amine (forming **S2-NH$_2$**), 3-azidopropan-1-ol (**S2-OH**), or 1-azidobutane (**S2-CH$_3$**).*

4.2 Results and discussion

4.2.1 Surface preparation and characterization

Silicon modified with a covalent Si–C-bound monolayer of 1,8-nonadiyne (**S1**, Figure 4.1) was chosen as a robust and well-studied platform for the protection and further modification of the semiconductor surface [150, 151]. Its stability and resistance towards oxidation are well documented in the literature [151]. The mechanism for this reaction is shown in Figure 4.2. A possible side reaction involved is the attachment of the terminal alkyne to the surface, however this is largely ruled out by the thickness of the monolayer as determined by X-ray reflectometry (Figure 4.4), as the monolayer of the **S1** surface is of a similar thickness to the length of 1,8-nonadiyne.

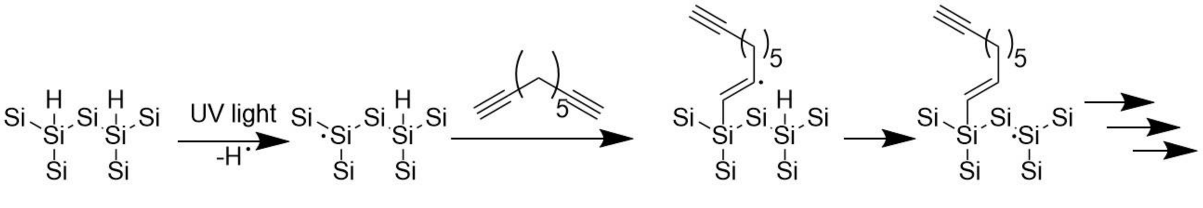

Figure 4.2: Mechanism for the attachment of 1,8-nonadiyne to SiH surface [36]. A hydrogen atom is removed from the Si surface, which is followed by attachment of 1,8-nonadiyne to the surface by a radical hydrosilylation. The formed C-centred radical then abstracts a hydrogen atom from a neighbouring Si atom, which then further reacts with 1,8-nonadiyne by the same mechanism.

A further advantage of this surface chemistry is the presence of a terminal alkyne moiety, which enables an high-yielding and straightforward surface modification via CuAAC reactions; the mechanism of which is shown in Figure 4.3 [85]. Side reactions of this process include homocoupling of alkynes, however this process is suppressed by an excess of sodium ascorbate, which prevents this oxidative coupling [154].

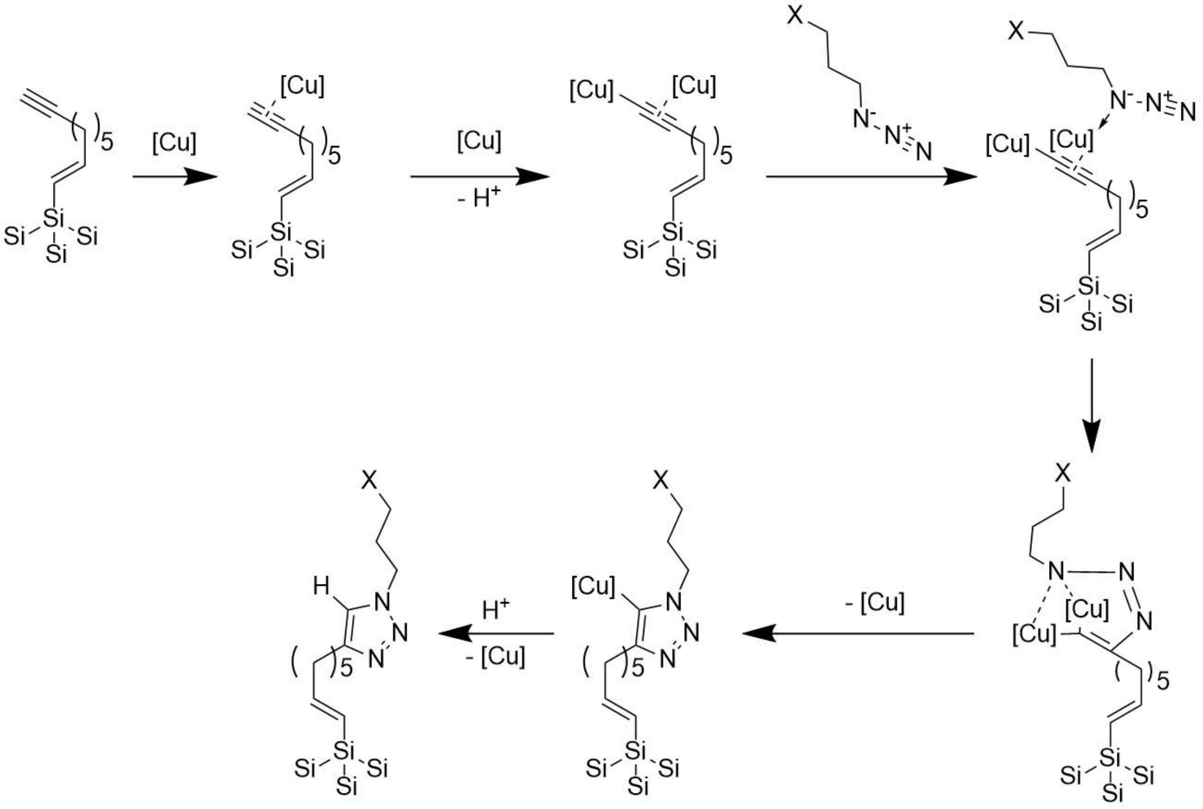

Figure 4.3: Mechanism of CuAAC reaction [155]. A Cu(1) complex coordinates to the terminal alkyne of the monolayer. This then further reacts with another equivalent of the Cu(I) complex which replaces the hydrogen of the terminal alkyne. The azide then coordinates to the Cu(I) complex which is coordinated to the alkyne by the π-system. This complex then rearranges to form a six-membered ring with the nitrogen coordinating to the two Cu(I) complexes. This eliminates one equivalent of the Cu(I) complex forming the 1,2,3-triazole. The final Cu(I) complex is replaced by hydrogen in the final step.

Functional azides used to modify the diyne-passivated silicon surface (**S1**) were structurally similar, with differences being limited to terminal functionality whilst maintaining the same number of atoms in the monolayer. As shown in Figure 4.1, the choice of introducing with the CuAAC reaction either a terminal amine (**S2-NH$_2$**), an alcohol (**S2-OH**) or a methyl (**S2-CH$_3$**) group allows access to a range of hydrophilicities of the surface and to systematically examine the effect of specific surface chemistries on the tribocurrent and friction of sliding metal–monolayer–semiconductor junctions. This experimental design also simplifies the analysis of surface chemistry on DC outputs, as maintaining a constant monolayer thickness removes potentially ambiguous data caused by the exponential dependence of current on tunneling distance. XRR data confirmed a comparable monolayer thicknesses for all three surface chemistries (Figure 4.4), hence comparable tunneling distances, removing the possibility of differences in tribocurrent (vide infra) arising simply from differences in monolayer thickness [156] rather than from different friction and chemistry.

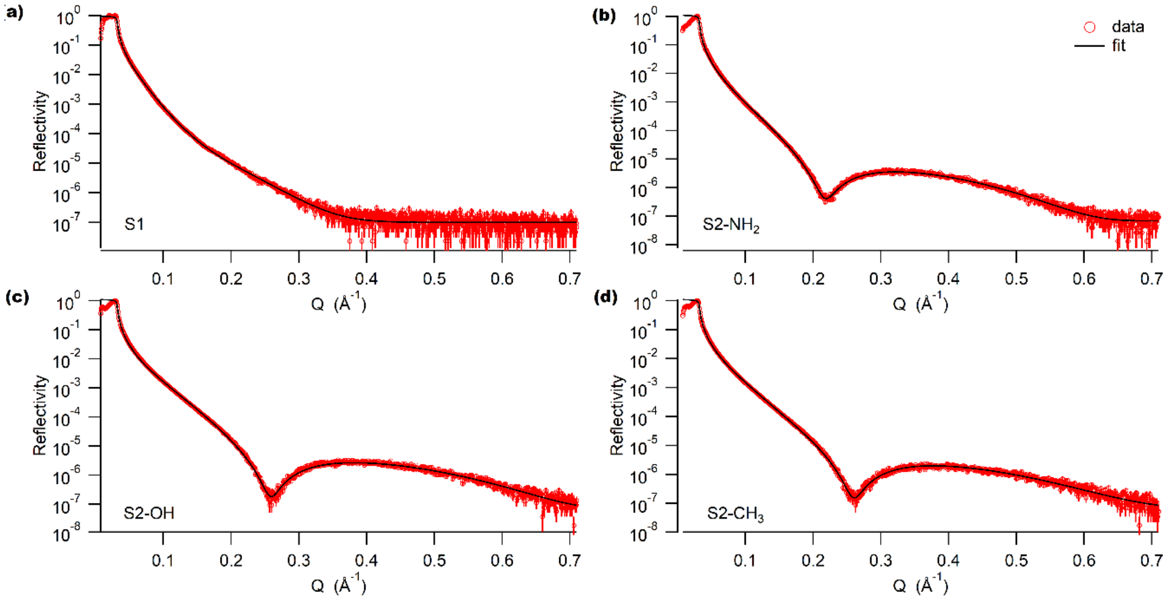

Figure 4.4: X-ray reflectometry (XRR) profiles of a) ***S1****, b)* ***S2-NH$_2$****, c)* ***S2-OH****, and d)* ***S2-CH$_3$*** *surfaces made on N-type silicon substrates. The points with error bars are the collected data and the solid lines are the fits to a monolayer model defined by its thickness (d), scattering length density (SLD), and roughness. The refined structural parameters were:* ***S1****, d = 10.38 (4.52) Å, SLD = 1.05 × 10^{-5} Å^{-2};* ***S2-NH$_2$****, d = 14.41 (0.24) Å, SLD = 1.21 × 10^{-5} Å^{-2};* ***S2-OH****, d = 12.23 (0.19) Å, SLD = 1.35 × 10^{-5} Å^{-2};* ***2-CH$_3$****, d = 12.12 (0.19) Å, SLD = 1.27 × 10^{-5} Å^{-2}. Estimated standard deviations (esd's) are given in parentheses. SLD for X-rays are equal to the material electron density (e^-/Å^3) multiplied by 2.82 × 10^{-5} Å. The refined electron densities obtained for these surface (~0.4 e^-/Å^3) are higher than the average 0.31 e^-/Å^{3}reported for a series of methyl-terminated monolayers prepared on Si(100) from 1-alkynes [157], reinforcing on the compactness of the organic monolayers used in this study.*

Further, C-AFM experiments used to estimate zero-bias DC outputs discussed below were conducted under ambient conditions (relative humidity of ~50%). Therefore controlling and measuring the hydrophilicity of each surface chemistry was done to account for a potentially crucial aspect: surface wetting. Wetting can affect adhesion and friction [158, 159], as well as static charging [160], hence it can potentially influence the performance of a TENG. As shown in Figure 4.5 a, changes to the monolayer distal caused changes in the static water CA value. Surface **S2-NH$_2$** was the most hydrophilic, followed by **S2-OH** and then **S2-CH$_3$**, while **S1** was the most hydrophobic with a contact angle of 80° which is comparable with prior reports [85]. It is interesting to note that the triazole ring formed upon the CuAAC reaction increases the sample hydrophilicity, presumably due to its large dipole moment. Values of water contact

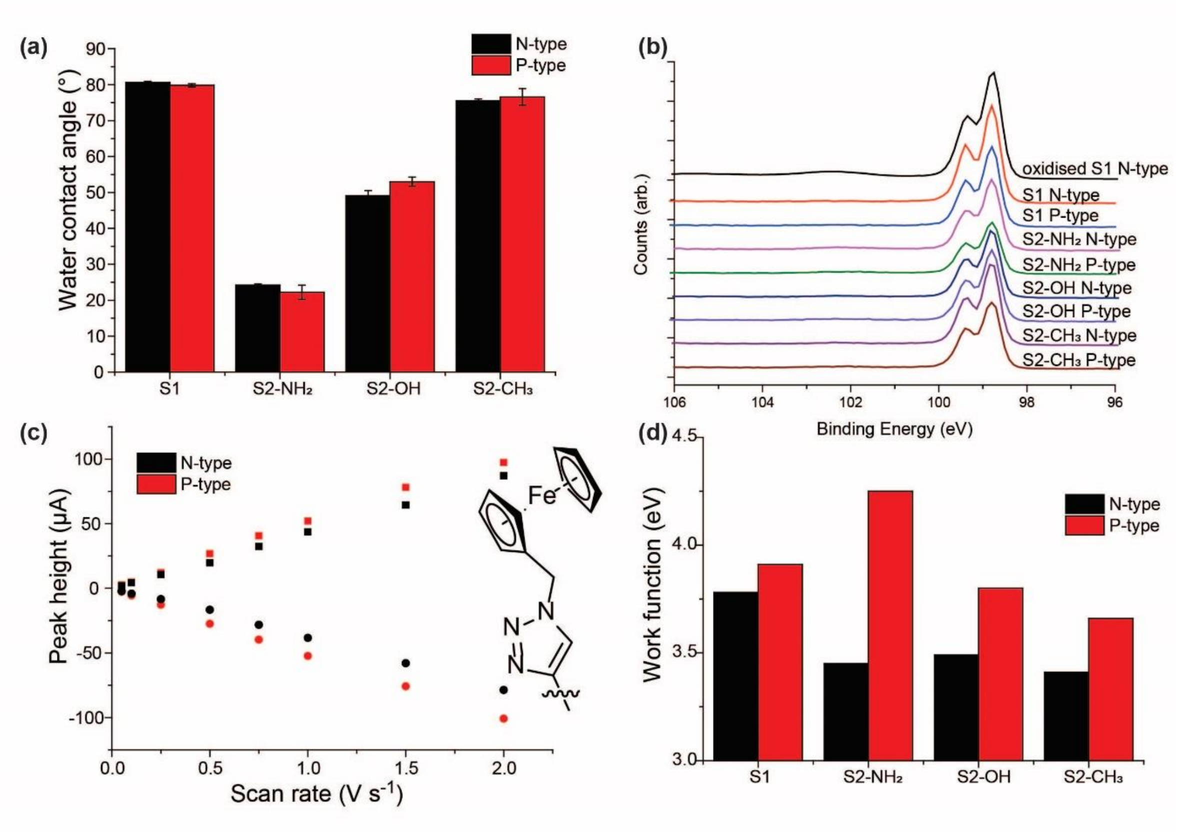

Figure 4.5: Silicon surface characterization. (a) Water contact angle measurements, showing minimal influence of substrate doping on wettability within samples of same surface chemistry. (b) High-resolution X-ray photoelectron spectroscopy of the Si 2p narrow region, showing minimal formation of silicon oxides. (c) Plot of the anodic (positive values) and cathodic (negative values) current peak heights obtained from cyclic voltammograms of ferrocene-terminated monolayers. Current data indicate a comparable ferrocene surface coverage, hence CuAAC yield, in both P- and N-type silicon. (d) Work function of the chemically passivated surfaces measured by ultraviolet photoelectron spectroscopy.

angle were comparable in both N- and P-type silicon, indicating a negligible effect of the silicon doping type on the surface wettability.

XPS data are consistent with a high yield of the CuAAC reaction, and shows spectral features consistent with the expected surface chemistry. Extensive XPS spectral data and their detailed discussion are in Figure 4.6, Figure 4.7, Figure 4.8 and Figure 4.9. Most importantly, Si 2p high-resolution scans (Figure 4.5 b) showed minimal sign of substrate oxidation on all the studied surfaces. While XPS-derived carbon/silicon elemental ratios, for both the CuAAC and hydrosilylation reactions, were similar between P- and N-type systems, we estimated CuAAC yields by means of electrochemical data obtained through cyclic voltammetry experiments (Figure 4.5 c and Figure 4.10). In these controls a conventional redox probe, an azide-tagged ferrocene, is first grafted through the CuAAC reaction on the base layer (**S1**) and then the redox probe surface coverage is accurately assessed by integrating the background-subtracted anodic and cathodic voltametric currents. The ferrocene voltametric signal is in a voltage region free from parasitic redox signals [153]. We estimated the surface density of ferrocene molecules to be 2.17×10^{-10} mol cm^{-2} (1.29×10^{14} molecules cm^{-2}) for P-type, leading to a fractional coverage of 0.165 based on the density of Si–H on Si(111) [161], or equivalent to 48% of the maximum density reported for closely-packed ferrocene head groups [162]. This coverage is close to the maximum value reported for similar chemistries on silicon [163]. Similarly, a coverage of 2.15×10^{-10} mol cm^{-2} (1.31×10^{14} molecules cm^{-2}) was measured for N-type electrodes, indicating a fractional coverage of 0.167 (49% of a closed-packed ferrocene layer). A CuAAC yield close to 50% for the derivatization of the surface acetylenes of **S1** is expected for this type of surface chemistry [138] and was therefore not further optimized.

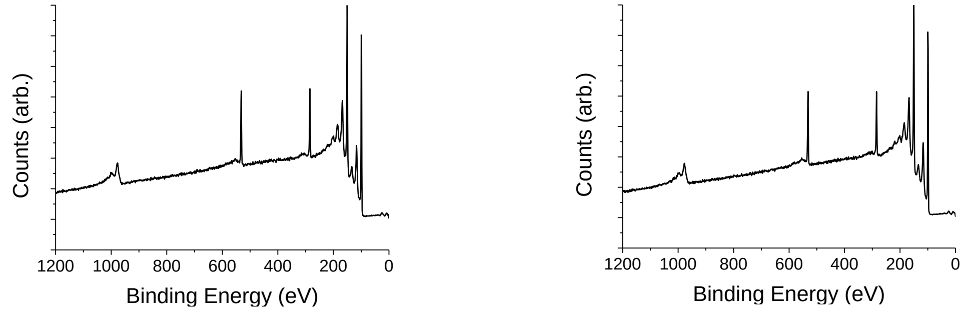

a) N-type **S1** b) P-type **S1**

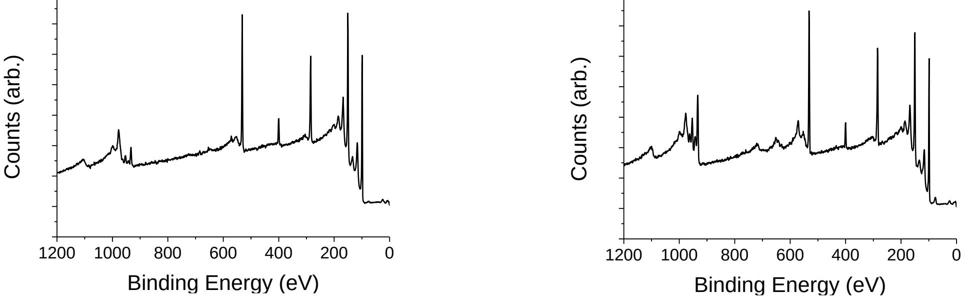

c) N-type **S2-NH$_2$** d) P-type **S2-NH$_2$**

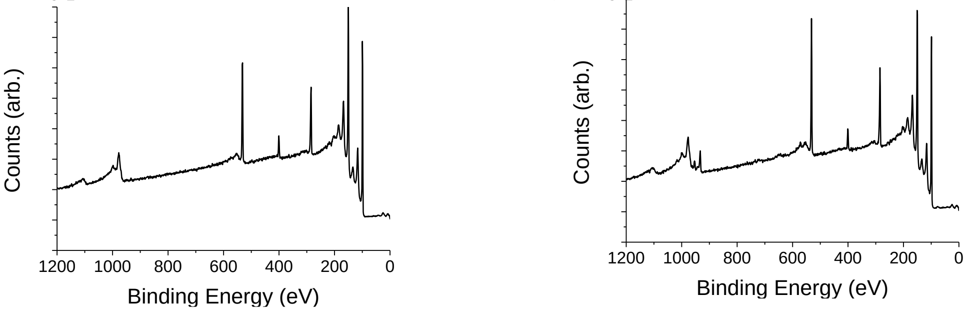

e) N-type **S2-OH** f) P-type **S2-OH**

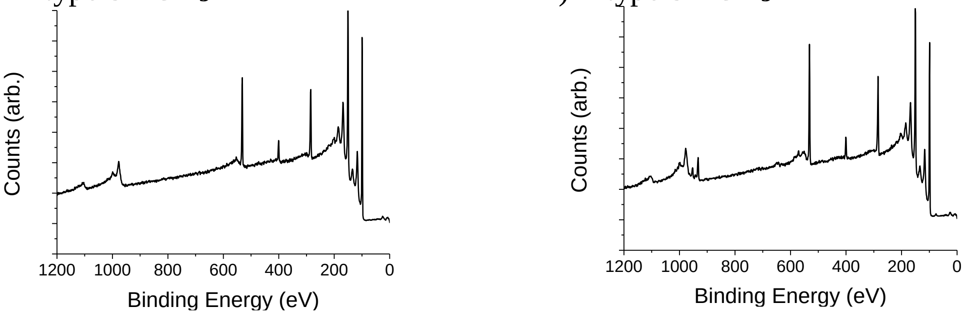

g) N-type **S2-CH$_3$** h) P-type **S2-CH$_3$**

Figure 4.6: XPS wide scans of a) ***S1*** *samples prepared on N-type silicon (C/Si ratio = 0.496), b)* ***S1*** *samples prepared on P-type silicon (C/Si ratio = 0.489), c)* ***S2-NH$_2$*** *samples prepared on N-type silicon (C/Si ratio = 0.871), d)* ***S2-NH$_2$*** *samples prepared on P-type silicon (C/Si ratio = 1.071), e)* ***S2-OH*** *samples prepared on N-type silicon (C/Si ratio = 0.623), f)* ***S2-OH*** *samples prepared on P-type silicon (C/Si ratio = 0.714), g)* ***S2-CH$_3$*** *sampled prepared on N-type silicon (C/Si ratio = 0.615), and h)* ***S2-CH$_3$*** *samples prepared on P-type silicon (C/Si ratio = 0.699). All wide scans showed expected emissions in agreement with the expected Si and C presence (all surfaces) and N (only for* ***S2*** *surfaces). Peaks corresponding to Cu emission at 933 eV were observed on N-type* ***S2-NH$_2$****, P-type* ***S2-NH$_2$****, P-type* ***S2-OH*** *and P-type* ***S2-CH$_3$****.*

a) N-type **S1**

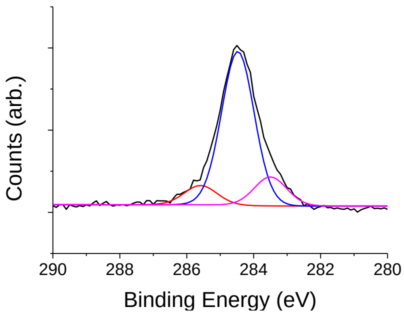

b) P-type **S1**

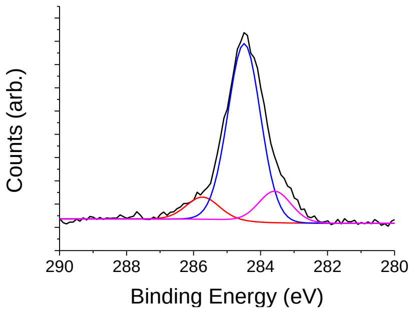

c) N-type **S2-NH$_2$**

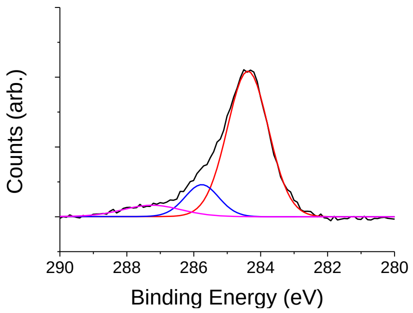

d) P-type **S2-NH$_2$**

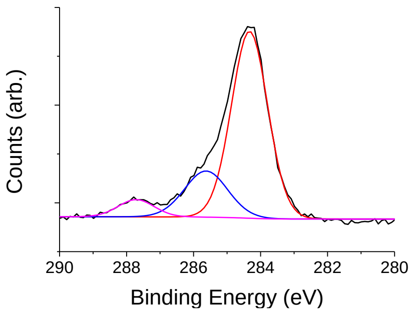

e) N-type **S2-OH**

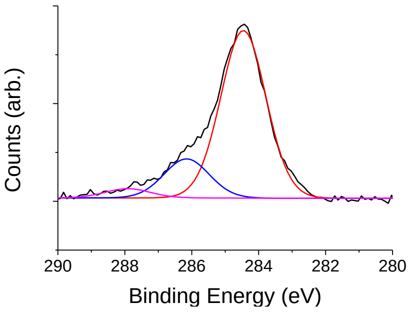

f) P-type **S2-OH**

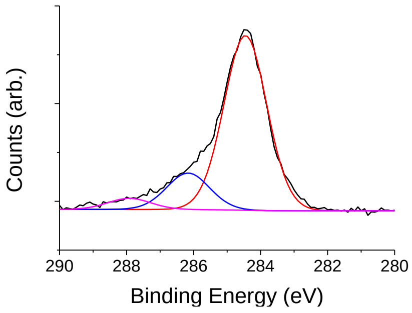

g) N-type **S2-CH$_3$**

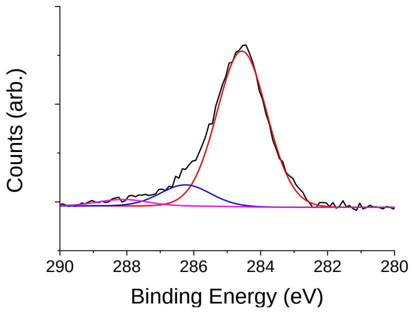

h) P-type **S2-CH$_3$**

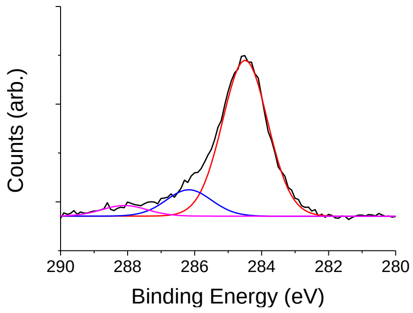

Figure 4.7: XPS narrow scans of the C 1s region of a) N-type S1, b) P-type S1, c) N-type S2-NH2, d) P-type S2-NH2, e) N-type S2-OH, f) P-type S2-OH, g) N-type S2-CH3 and h) P-type S2-CH3 samples. For S1 surfaces, three mixed Gaussian–Lorentzian (80% Gaussian and 20% Lorentzian) functions were required to fit the experimental C 1s band. These three refined components were centred at 283.5, 284.5 and 285.6 eV corresponding respectively to C–Si (silicon-bound carbons, [164]), C–C (carbon-bound carbons [165]), and carbon in either a C–OH or C≡C bonding configuration for the high energy component [166]. For S2 surfaces, three separate functions were also required fit the experimental C 1s emission. These functions were located at 284.5, 286.1 and 287.9 eV, corresponding to C–C, the C–N/C–O and the C=N carbons, which is consistent with previous reports [85].

a) N-type **S1**

b) P-type **S1**

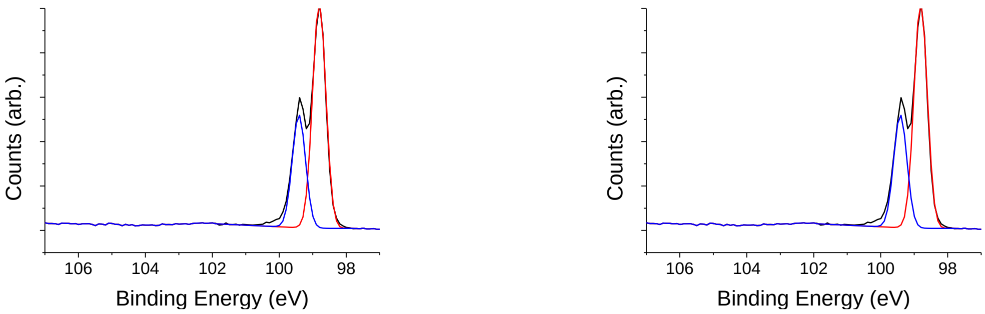

c) N-type **S2-NH$_2$**

d) P-type **S2-NH$_2$**

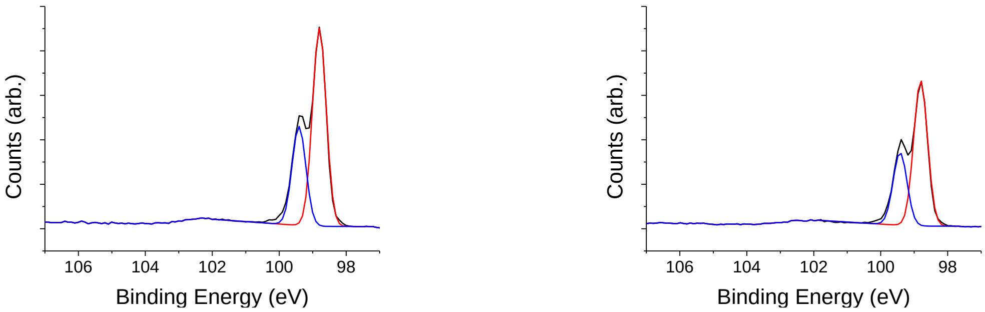

e) N-type **S2-OH**

f) P-type **S2-OH**

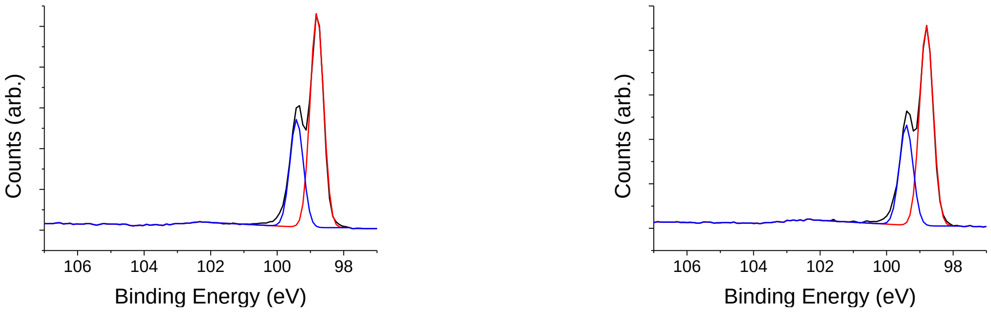

g) N-type **S2-CH$_3$**

h) P-type **S2-CH$_3$**

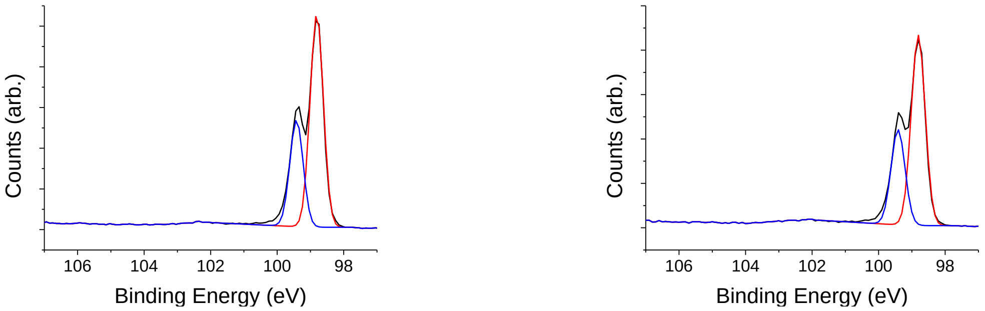

Figure 4.8: XPS narrow scans of the Si 2p region of a) N-type ***S1****, b) P-type* ***S1****, c) N-type* ***S2-NH$_2$****, d) P-type* ***S2-NH$_2$****, e) N-type* ***S2-OH****, f) P-type* ***S2-OH****, g) N-type* ***S2-CH$_3$*** *and h) P-type* ***S2-CH$_3$*** *samples. For all surfaces, the experimental Si 2p emission was fitted with two mixed Gaussian–Lorentzian (95% Gaussian and 5% Lorentzian) functions centred at 98.8 and 99.4 eV, corresponding respectively to the 2p$_{3/2}$ and 2p$_{1/2}$ spin–orbit-split components, and having a FWHM of 0.5 eV. This assignment is in line with previous reports [85]. The silicon 2p scan emission did not show evidence of oxidised silicon on the* ***S1*** *surfaces, however a minor high binding energy component located at ca, 102 eV was detected in the* ***S2*** *samples and attributed to minor presence of silicon oxides. We attribute this to oxidation during the CuAAC reaction, however silicon oxide was not observed in AFM (e.g. Figure 4.14), which generally appears as sharp topographic features.*

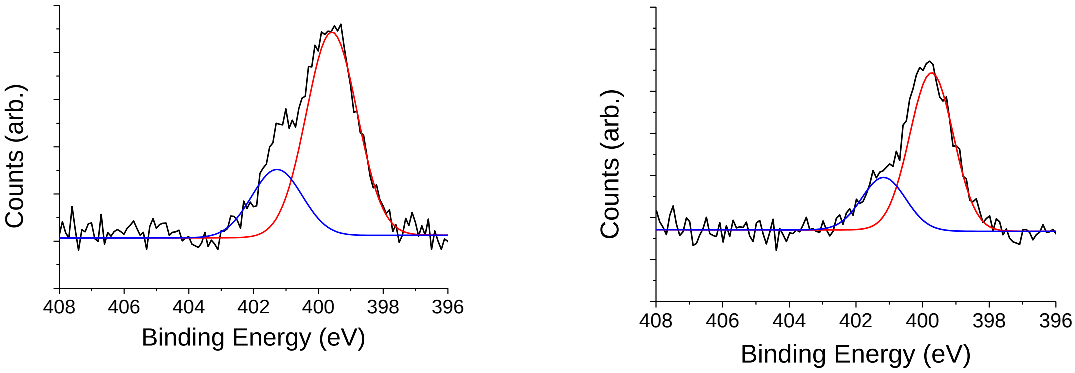
a) N-type **S2-NH$_2$**

b) P-type **S2-NH$_2$**

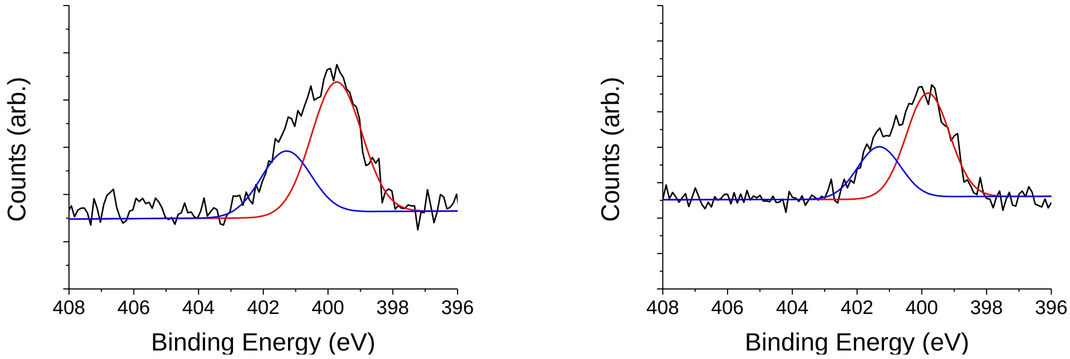
c) N-type **S2-OH**

d) P-type **S2-OH**

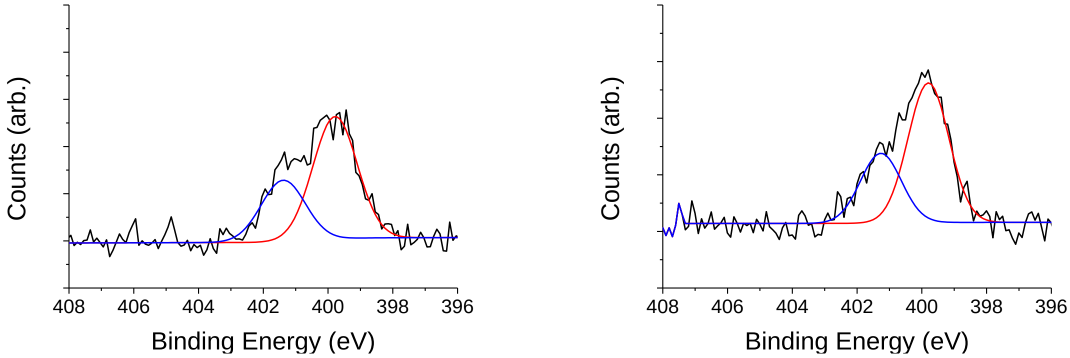
e) N-type **S2-CH$_3$**

f) P-type **S2-CH$_3$**

*Figure 4.9: XPS narrow scans of the N 1s region of a) N-type **S2-NH$_2$**, b) P-type **S2-NH$_2$**, c) N-type **S2-OH**, d) P-type **S2-OH**, e) N-type **S2-CH$_3$** and f) P-type **S2-CH$_3$** sample. The N 1s experimental signals were fitted with two Gaussian functions centered at 399.7 and 401.3 eV, corresponding to $\underline{N}{=}\underline{N}$–N and NH$_2$ (for **S2-NH$_2$** surfaces) and N=N–$\underline{N}$ in line with previous reports [85, 167]. As expected from the chemical structure of the azide tethered onto the surface, the two refined contributions were a 2:1 ratio for **S2-OH** and **S2-CH$_3$** samples, and in a 3:1 ratio for **S2-NH$_2$** surfaces. No emission corresponding to unreacted (physically adsorbed rather than chemisorbed) azide molecules, expected at 405 eV [168], was seen in any of the spectra.*

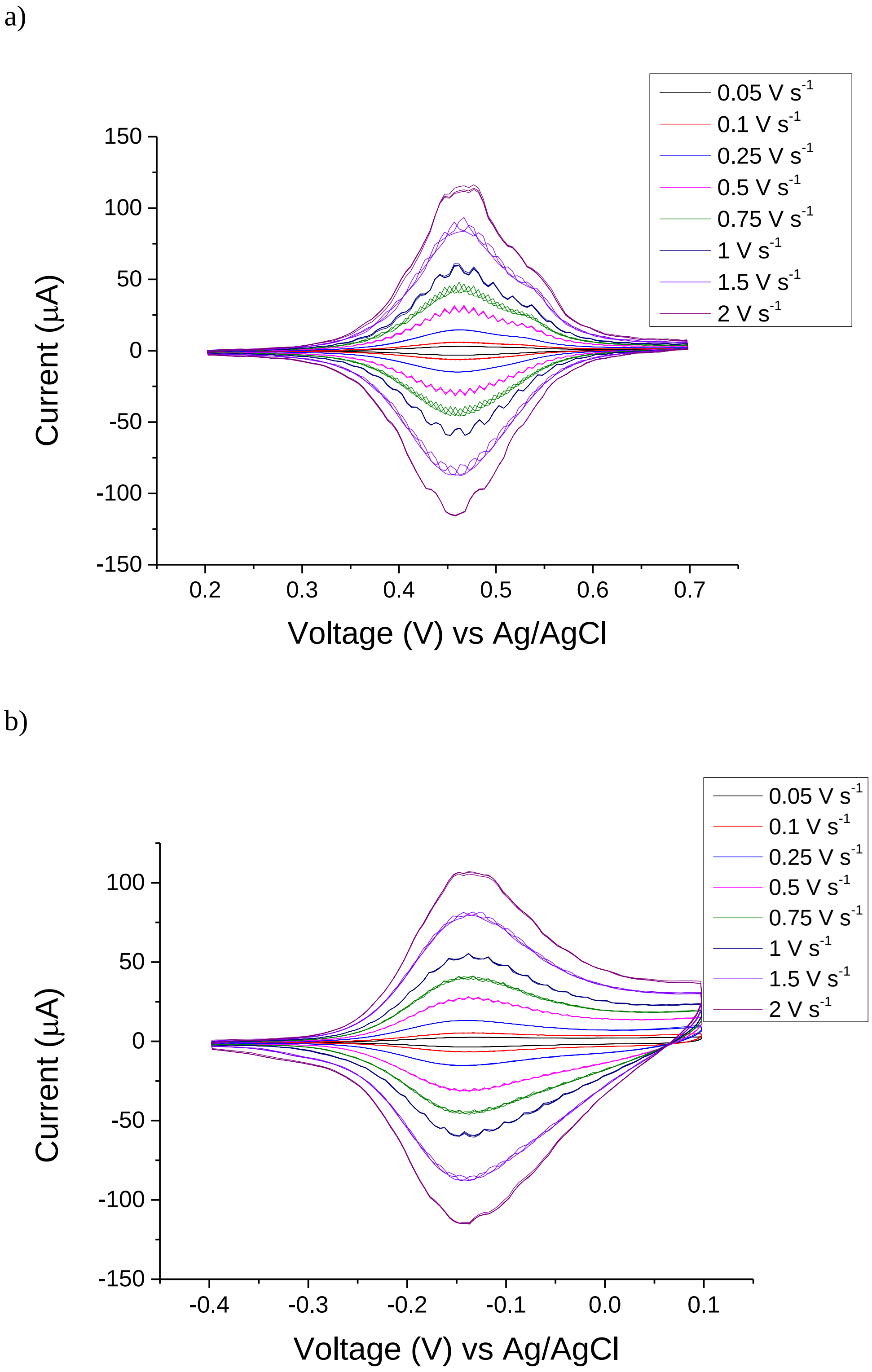

Figure 4.10: Electrochemical measurements of the CuAAC reaction yields (surface coverage). Cyclic voltammograms recorded at a variable voltage sweep rate (indicated by the labels in figure) of ferrocenylated silicon surfaces (chemical details as per Fig. 2c). The silicon surface served as the working electrode, and Ag/AgCl as the reference electrode, and a platinum coil as the counter electrode. The electrolyte was aqueous 1.0 M $HClO_4$. Panel (a) shows data for P-type samples under ambient light, and (b) for N-type samples under red light illumination (660 nm).

Despite surface coverage and wettability not being affected by the substrate doping type, a doping-related electronic effect is present and is tuned by the surface chemistry. UPS data in Figure 4.5 d and Figure 4.11 reveal a stronger electronic effect, imparted by the monolayer chemistry, on P-type than on N-type silicon. On N-type silicon, the surface work function is reduced after the formation of the triazole ring, but this reduction is independent to the terminal chemistry of the monolayer. On the contrary, on P-type we found a significant electronic effect by the monolayer chemistry. This is tentatively attributed to the presence of residual copper catalyst in the monolayer, see Figure 4.12, which parallels the observed trend in work functions. Surprisingly the protocol [169] used to remove the CuAAC copper catalyst in these experiments was highly effective for N-type, but not for P-type.

After having validated the surface chemistry strategy (by XPS), ensured a consistent tunneling barrier (XRR), assessed the wettability and propensity to uptake ambient water (CA and XRR), and gauged surface work functions (UPS), we next moved to studying the electrical and tribological properties of these surfaces.

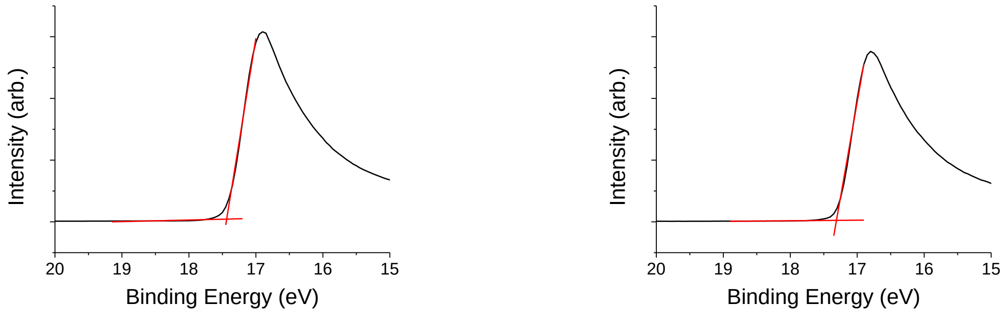

a) N-type **S1**

b) P-type **S1**

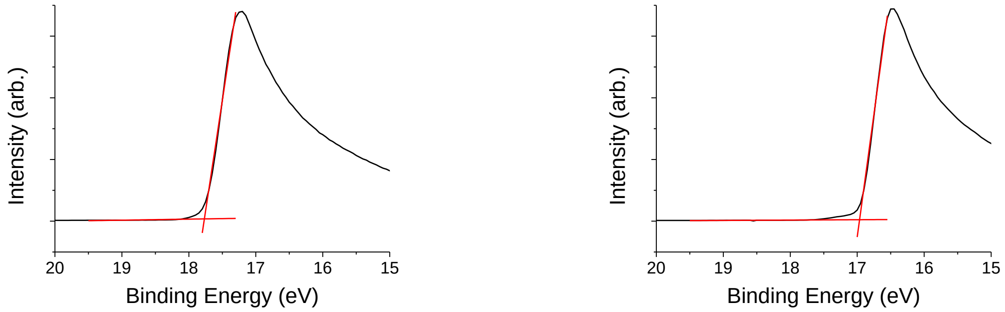

c) N-type **S2-NH$_2$**

d) P-type **S2-NH$_2$**

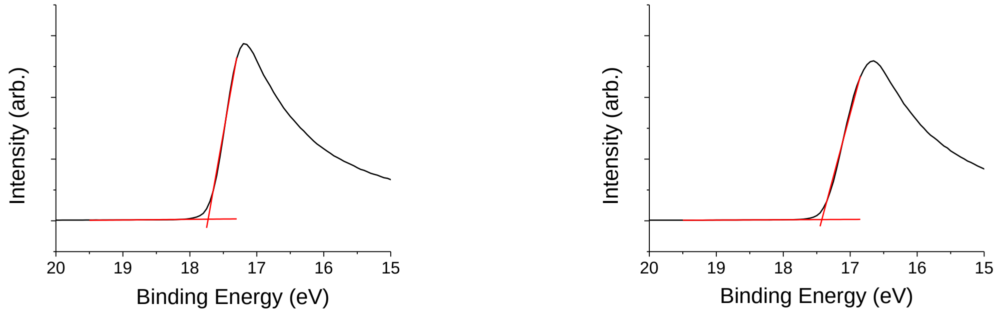

e) N-type **S2-OH**

f) P-type **S2-OH**

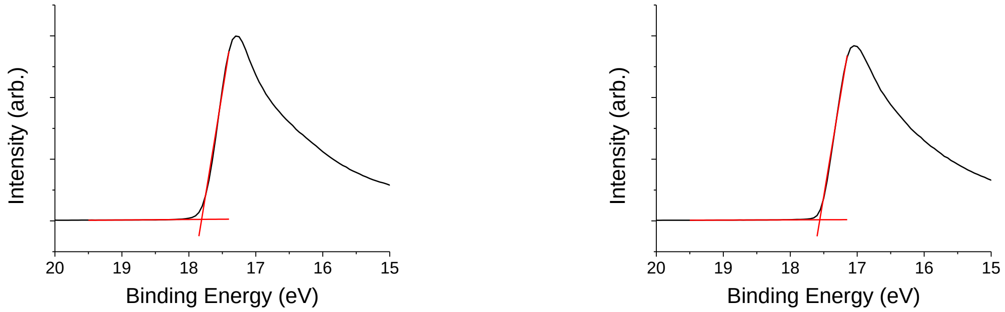

g) N-type **S2-CH$_3$**

h) P-type **S2-CH$_3$**

Figure 4.11: UPS spectra of the secondary edge region of a) N-type ***S1****, b) P-type* ***S1****, c) N-type* ***S2-NH$_2$****, d) P-type* ***S2-NH$_2$****, e) N-type* ***S2-OH****, f) P-type* ***S2-OH****, g) N-type* ***S2-CH$_3$*** *and h) P-type* ***S2-CH$_3$*** *samples. The black line is the acquired data and the red lines are linear fits to the flat and steep regions. The work function of each sample was estimated from the position of the intersection between the flat lines (subtracted from the 21.218 eV excitation energy).*

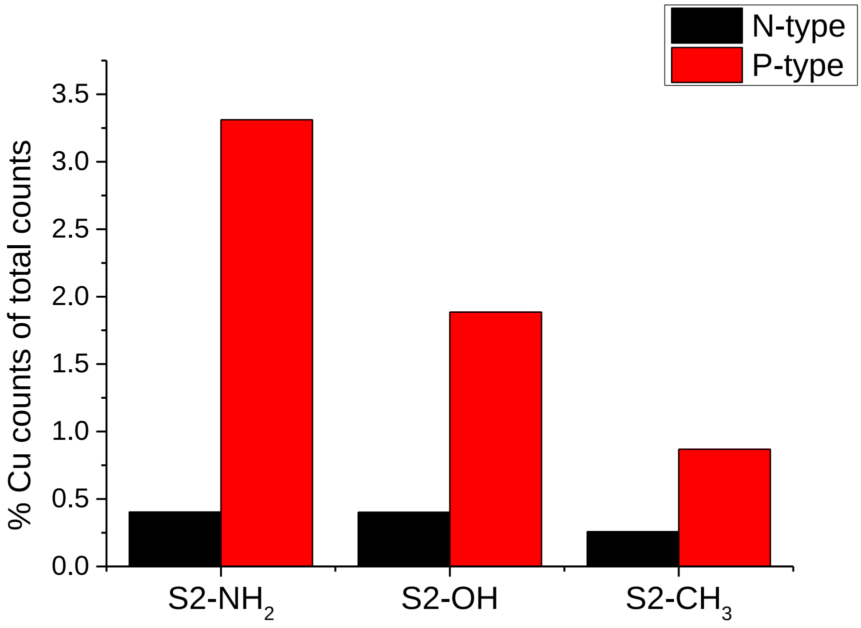

Figure 4.12: XPS-derived surface copper concentration estimated as percentage of the total photoelectron counts. In general, a small amount of copper was observed on samples prepared on N-type silicon, while a greater amount was observed for P-type surfaces. This trend tracks the change in work function (UPS data, Figure 4.11).

4.2.2 Tribocurrent and friction

Conductive AFM (C-AFM) measurements revealed differences in friction and current outputs with varying monolayers and doping of the silicon underneath. Importantly, the use of conductive AFM tips allows us to measure, simultaneously, the zero-bias current as well as the friction and topography across the surface. The generation of DC current with a metal−semiconductor moving contact, rooted in a tribovoltaic effect, is well established [99, 141, 150]. In a typical C-AFM experiment, such as for those shown in Figure 4.13, we simultaneously measured topography (Figure 4.13 b), current (Figure 4.13 c) and friction (Figure 4.13 d) across a range of applied loads (0–100 nN), and then measured the static current–voltage (Figure 4.13 e,f) and force–distance characteristics to determine adhesion afterwards. Topography was observed to be similar between all surfaces (Figure 4.14), and typical of an oxide-free terraced Si(111) crystal surface [153] with a surface roughness (Ra) as low as 0.099 nm. For both P- and N-type substrates, static junctions made on **S1** surfaces showed the smallest current across the entire voltage range (Figure 4.13 e and f). In Figure 4.13 e, the I–V curves of P-type surfaces with **S2-OH** and **S2-CH$_3$** monolayers showed similar current response while the **S2-NH$_2$** monolayer showed a similar profile but a smaller current. In Figure 4.13f, the currents in the reverse bias (positive quadrant in our setup) for N-type surfaces increased in the same order as the sample hydrophilicity (**S2-NH$_2$** > **S2-OH** > **S2-CH$_3$** > **S1**). This warrants particular attention since the zero-bias current has the direction of a reverse bias (leakage) current. This current is mainly carried by holes tunneling under the barrier of the Pt–Si junction, as previously demonstrated [150]. The nulling voltages were measured in another AFM experiment (Figure 4.15) and are consistent with this mechanism.

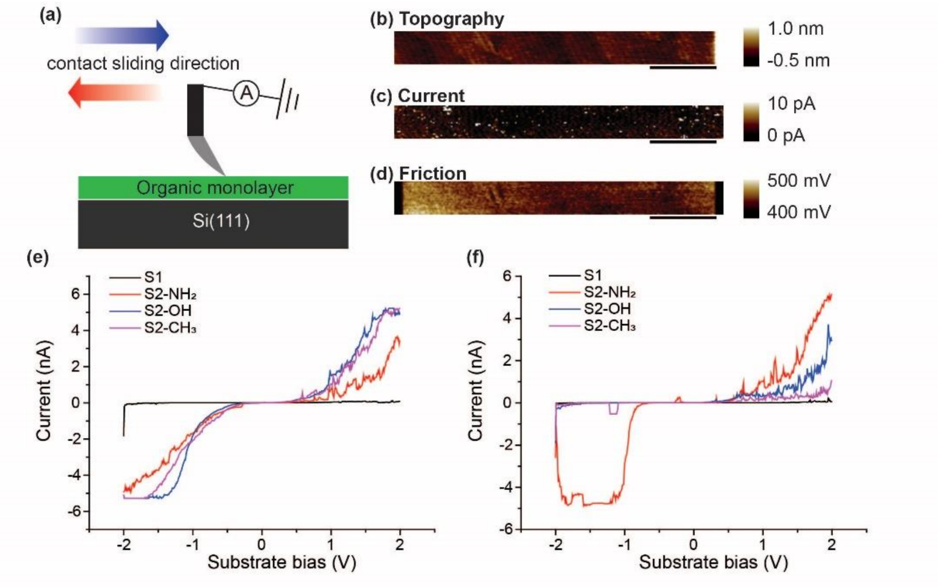

*Figure 4.13: AFM experiments. (a) Schematic showing the AFM tip–monolayer–Si sliding contact and the configuration of the electrical circuit for C-AFM. In our C-AFM setup the external voltage bias is applied to the substrate. b) Typical topography data of a monolayer-modified crystalline Si surface (**S2-NH₂**, N-type). (c) Representative zero-bias (0.0 V) current image of a sliding junction (**S2-NH₂**, N-type). (d) Representative friction loop image (friction measured in the trace direction minus the friction measured in the retrace direction, all divided by two to give the friction force; **S2-NH₂**, N-type). (e,f) Current–voltage (I–V) curves acquired on P-type (e) and N-type (f) silicon surfaces bearing different monolayers (each trace is the average of ten I–V curves; labels to the curves specify the monolayer chemistry).*

a) N-type **S1**

Ra = 0.170 nm

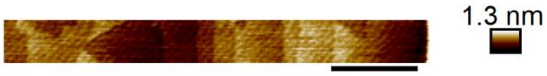

b) P-type **S1**

Ra = 0.099 nm

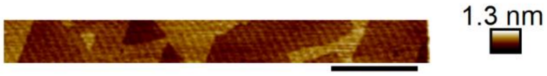

c) N-type **S2-NH₂**

Ra = 0.116 nm

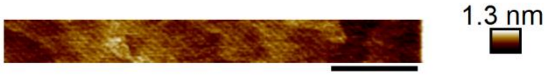

d) P-type **S2-NH₂**

Ra = 0.116 nm

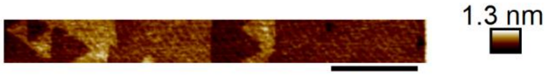

e) N-type **S2-OH**

Ra = 0.311 nm

f) P-type **S2-OH**

Ra = 0.134 nm

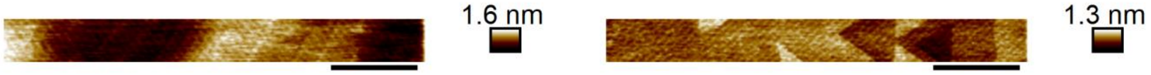

g) N-type **S2-CH$_3$**

Ra = 0.133 nm

h) P-type **S2-CH$_3$**

Ra = 0.105 nm

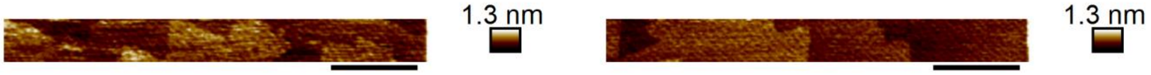

Figure 4.14: Topography AFM images and roughness values for all surfaces of this study ((a) N-type ***S1****; (b) P-type* ***S1****; (c) N-type* ***S2-NH$_2$****; (d) P-type* ***S2-NH$_2$****; (e) N-type* ***S2-OH****; (f) P-type* ***S2-OH****; (g) N-type* ***S2-CH$_3$****; (h) P-type* ***S2-CH$_3$****). The topography images are height sensor images acquired under an applied force of 50 nN. Analysing data of a 1.8 μm × 200 nm region allows removing edge artifacts. This was the same sampling area on which friction data are also measured. Scale bars are 400 nm. Surface roughness (Ra) values are indicated in figure.*

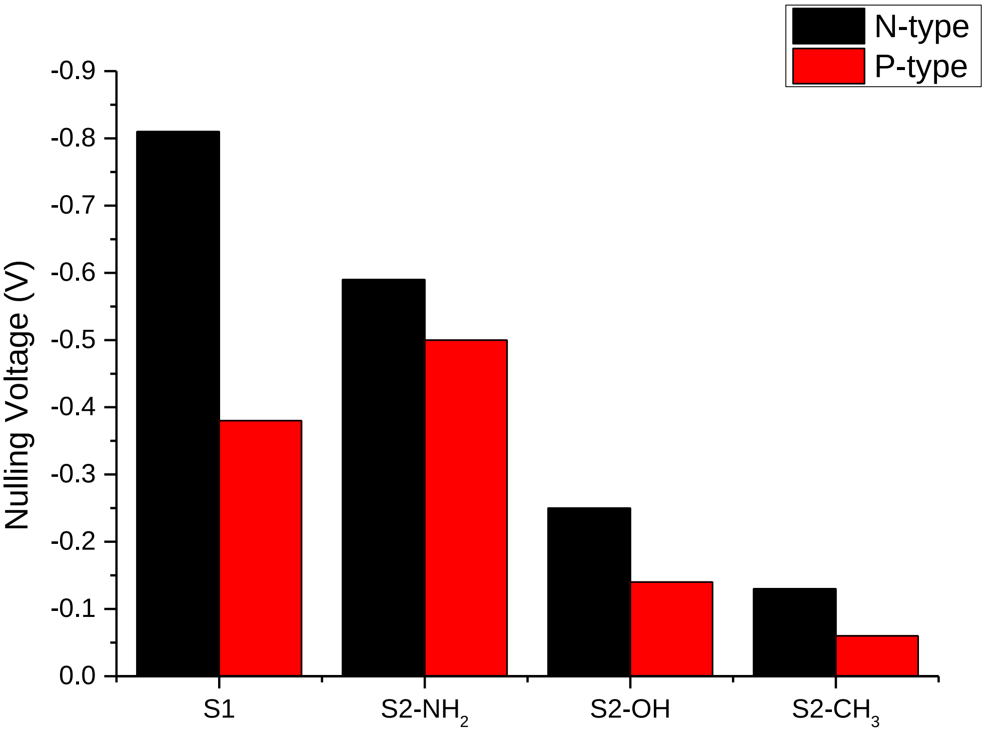

Figure 4.15: Nulling voltages as determined from I–V curves, as the external bias at which the current switches sign. These data show a consistently greater (more negative) nulling voltages on N-type over P-type, and indicate a greater effect on nulling voltage mediated by the monolayer chemistry rather than by the doping type of the underneath silicon.

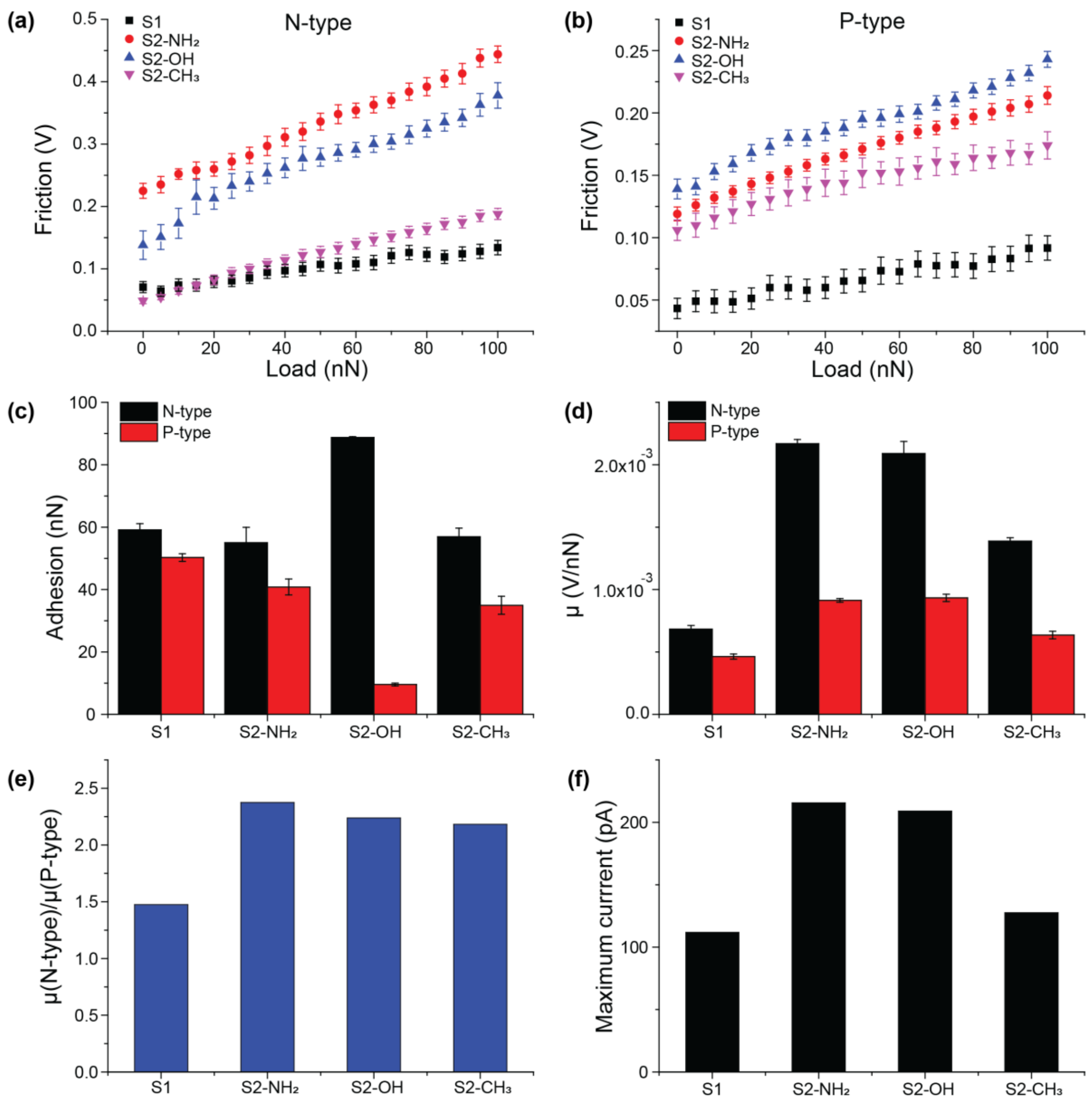

Figure 4.16: AFM-derived friction, adhesion and zero-bias current data. (a,b) Friction force versus normal force data for all monolayer systems ((a), N-type silicon; (b) P-type silicon). Data recorded at zero applied bias. c) Adhesion data for all monolayer systems, prepared on either N- or P-type silicon substrates. d) Friction coefficients (μ) for all monolayer systems (N- and P-type silicon substrates). e) Ratio between the friction coefficient of samples with the same monolayer type but grafted on either N- or P-type silicon. Data indicate a significantly larger μ on N-type samples for all ***S2*** *monolayers systems, while the N-/P- ratio of μ was closer to unity for the* ***S1*** *monolayer. f) Maximum zero-bias tribocurrent output measured on samples prepared on N-type silicon. Sliding junctions made on P-type silicon did not show a zero-bias current greater than the noise in the measurements (~1 pA).*

As shown in Figure 4.16a,b, the measured friction increases with increased load. This is an expected behaviour. An effect on friction is seen by varying the monolayer chemistry while keeping unchanged the substrate doping. Friction increases for monolayers with more polar end groups (**S2-NH$_2$** and **S2-OH**) compared to interfaces exposing less polar terminal functionalities (**S1** and **S2-CH$_3$**). This molecular effect on friction is however more pronounced on P- than on N-type silicon. It is also worth noting that friction was substantially lower on all

P-type surfaces (Figure 4.16b), which, as will be discussed later, are the surfaces with the lower (negligible) zero-bias tribocurrent output. To shine some light on this relationship between friction, doping type and current, specifically, to start addressing the question as whether friction can be, at least in part, a response and therefore, not only because of a passing current, adhesion on N-type surfaces (Figure 4.16c) was observed to be vary weakly with the chemistry of the monolayer, except for a greater adhesion on the **S2-OH** surface. P-type surfaces showed a greater variation in the adhesion with the lowest adhesion being observed on the **S2-OH** surface. Importantly, it is clear that the trend in adhesion does not follow the trend in friction coefficients, so, once again, dynamic factors such as current generation cannot be neglected as having a role in influencing friction.

This finding points towards the tip–surface interaction being governed both by the chemistry of the terminal group as well as involving an electronic effect from the silicon beneath the monolayer. Wear of the tip was ruled out by measuring the tip radius between each surface, which was not found to change.

To gain further insights on the link between friction and current, especially trying to unveil to what extent friction is a response to current and not strictly vice-versa, friction was modelled by a modified form of Amontons' Law where the lateral force (F_L), measured here in Volts, is given by $F_L = \mu F_N + F_0$, and μ is the friction coefficient (with units V/nN) [58]. The friction is measured in Volts due to it being determined by the lateral deflection of the AFM tip which gives rise to a voltage on the photodiode used to determine the angular position of the tip. This voltage is proportional to the friction force by a constant calibration term. We performed linear regression on each of the friction–load curves and the experimentally determined values of μ are shown in Figure 4.16d. As for the friction data discussed above, there is clear evidence of a pronounced effect of the doping type on the friction coefficient. This effect is made more explicit in Figure 4.16e, which plots the ratio of μ values for N-type surfaces over that obtained for P-type surfaces. This was to isolate, within the same monolayer system, the effect of doping alone over the friction coefficient. The N-type to P-type ratio of μ is comparable within experimental error for each of the CuAAC surfaces (**S2-NH$_2$**, **S2-OH**, **S2-CH$_3$**) surfaces, however this is noticeably different to the ratio obtained for **S1** samples, which is closer to unity. This suggests that the backbone of the organic monolayer itself is non-innocent in mediating a substrate-doping effect on friction. The cause is at present unclear, but one crucial difference between the **S1** and all **S2** monolayers is the presence of a 1,2,3-triazole in the latter. It appears as though this feature amplifies the effect of the doping on friction, possibly through the dipole of this group interacting with the electric field of the Schottky junction. A lateral flexoelectronic effect in addition to the flexoelectronic effect due to the normal force may also be present [13].

The most obvious environmental interference on friction and adhesion– differences in nano- and micro-scale water adsorption – was tested by XRR [46]. In general, prior to AFM experiments, surfaces were rinsed with dichloromethane, which will remove water from these surfaces. However measurements were done in air, and there is the possibility that surfaces will slowly re-adsorb water. As shown by XRR data in Figure 4.17, N- and P-type surfaces adsorb nanoscopic layers of water at comparable rates. We thus conclude that the adsorption of water from the air is not a major factor in the causing different friction coefficients between different dopings. This however does not discount the effect of the formation of the water meniscus between the tip and surface influencing the difference between friction coefficients between the different monolayers, yet it will unlikely be the cause of the difference between N- and P-type samples, where the main difference remains the different zero-bias tribocurrent output.

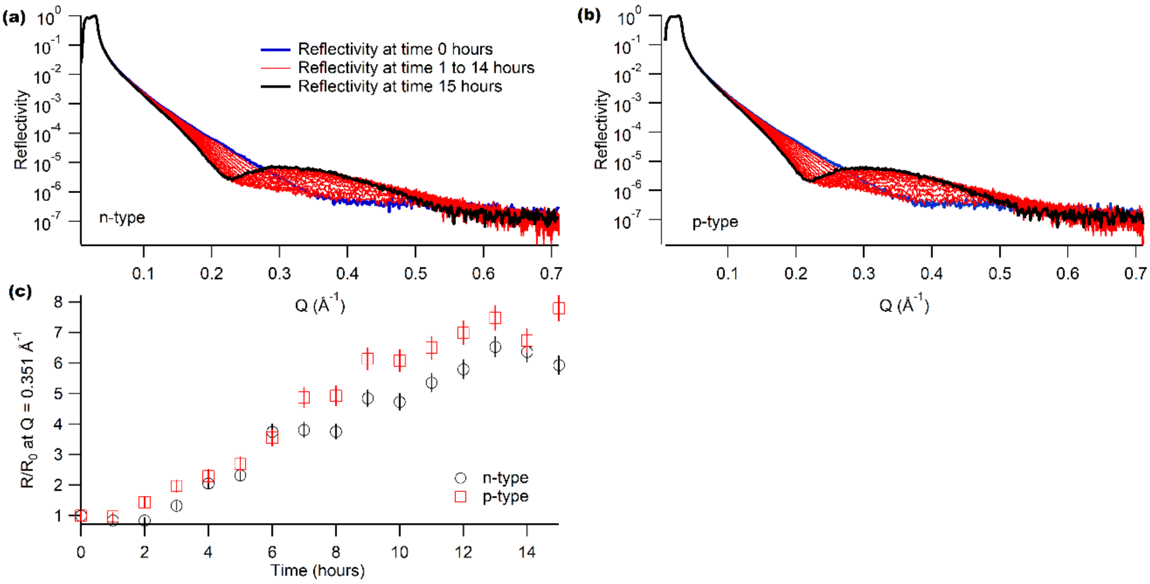

Figure 4.17: X-ray reflectometry (XRR) analysis of the nanoscale water-uptake kinetics on monolayer-modified samples. By unveiling the time scale required for a nanoscale water layer to adsorb, time-resolved XRR experiments allowed to rule out a doping-related effect on water uptake, hence a link between friction and current with surface water layers. The velocity and extent of water accumulation is comparable between P- and N-type samples. (a,b) XRR data showing the accumulation of water on ***S1*** *surfaces, showing no kinetic difference, between samples made on substrates of different doping type, in the water uptake from air ((a) N-type silicon; (b) P-type silicon). The blue XRR profiles are obtained on dry samples ($t = 0$ h), while the red curves are profiles obtained between 1 and 15 h after exposure of the samples to ambient air. The emergence of a Kiessig fringe indicate nanoscale water accumulation on the surface. This water layer makes the system overall progressively thicker, and the black traces are the final measurements at time $t = 15$ h. (c) Plot of R/R_0 at $Q = 0.351$ Å^{-1} (where R is reflectivity at a given time and R_0 is reflectivity a $t = 0$ h) which shows increasing intensity of the Kiessig fringe over time.*

As shown in Figure 4.13 f, beside doping type, tribocurrents were greatly affected by the terminal chemistry. Current densities and contact areas are presented in Table 4.1. By simply changing the monolayer end group we were able to increase the current output by a factor of two and the current density by a factor of 1.9 (Table 4.1: DMT Contact areas and current densities at 100 nN normal force. The current measured for P-type surfaces did not show a greater zero-bias current than the noise in the measurements (~1 pA).).

Table 4.1: DMT Contact areas and current densities at 100 nN normal force. The current measured for P-type surfaces did not show a greater zero-bias current than the noise in the measurements (~1 pA).

Doping type / sample	Contact area (nm^2)	Current density (10^6 A m^{-2})
N-type / **S1**	47	2.4
P-type / **S1**	45	-
N-type / **S2-NH$_2$**	46	4.6
P-type / **S2-NH$_2$**	44	-
N-type / **S2-OH**	53	3.9
P-type / **S2-OH**	37	-
N-type / **S2-CH$_3$**	47	2.7
P-type / **S2-CH$_3$**	42	-

The DMT (Derjaguin-Muller-Toporov) model of contact is appropriate for hard, poorly adhesive materials, such as Si, even when coated with a monolayer. For the DMT model, the contact area is given by the following formula, where R is the tip radius, K is the reduced Young's modulus, L is the normal force and $2\pi R\gamma$ is the adhesive force [170]:

$$A = \pi \left[\frac{R}{K}(L + 2\pi R\gamma)\right]^{\frac{2}{3}}$$

The Young's modulus for Pt and Si are 177.3 GPa and 162.9 GPa respectively and the Poisson ratios are 0.395 and 0.222 respectively [171]. The reduced Young's modulus for the Pt–Si contact is given by the formula:

$$\frac{1}{K} = \frac{4}{3}\left(\frac{1-\nu_1^2}{E_1} + \frac{1-\nu_2^2}{E_2}\right)$$

K for this contact is 70.8 GPa. The tip radius is measured to be 26 nm by AFM in TUNA mode on a standard Ti Roughness sample. The adhesive forces are stated in Figure 4.16d). The normal force is 100 nN at maximum applied force.

Thicker monolayers (e.g. **S2-NH$_2$** versus **S1**) did show the largest output despite the longer tunneling distance, which suggests that the triazole has a positive effect on the current output. The study of the effect of surface dipoles in general is lacking [172] and the modification of surface chemistry can have an impact on the work function and electron affinity of a surface [173]. Zero-bias currents for sliding junctions made on P-type samples did not rise above noise level (~1 pA), while on N-type surfaces (Figure 4.16f) were substantial and tracked the measured friction. This trend also correlates with the static I–V properties, such as the magnitude of the reverse bias current shown in Figure 4.16 f, revealing a powerful diagnostic tool to screen and select for surfaces most likely to lead to a larger tribocurrent and proving a relationship between the static electrical properties and the dynamic friction.

4.3 Conclusions

Despite chemical methods to modify surfaces being routinely exploited in applications ranging from chemical catalysis to sensing, the scope of engineering the surface chemistry of a semiconductor towards improving the performance of TENGs based on sliding Schottky diodes is underexplored. We prepared a series of silicon–carbon-bound organic monolayers on oxide-free Si(111), with an emphasis on controlling the thickness of the organic film (tunneling distance) whilst changing the monolayer terminal chemistry in order to tune friction, adhesion, wettability and work function of the surface. One possible complication here is that the electron tunneling depends on the barrier height and not just the thickness of the monolayer, so this is an avenue of future research.

These monolayers were studied by C-AFM to examine, in particular, the links between friction and current output. We demonstrate that surface chemistry can maximize the zero-bias tribocurrent output, primarily by the formation of a 1,2,3-triazole moiety in the monolayer causing a significant reduction in work function, and increase in static leakage current. Triazole-bearing monolayers with dipolar terminations (amines and alcohols) showed the largest static leakage, matched by the largest DC current output at zero bias. Chemistry-related changes in adhesion do not appear to have a significant effect on tribocurrent outputs. This work has unveiled a surprising and pronounced effect of substrate doping type on the friction of a sliding platinum–monolayer–semiconductor junction. This discovery is counterintuitive, as the generally accepted view is that of friction being determined primarily by the chemistry and morphology of an interface. We show that for monolayer-modified crystalline Si(111) samples, having identical chemistry and morphology, a greater friction manifests when, under no external bias, larger tribocurrents cross the interface. This work bridges the fields of surface chemistry and molecular electronics with the rapidly expanding field of triboelectricity.

4.4 Acknowledgements

S.C. and N.D. acknowledge support from the Australian Research Council (grants no. DP190100735, FT190100148). G.G.A and G.K. acknowledge support from Microscopy Australia, from the Australian National Fabrication Facility (ANFF), and from Flinders Microscopy and Microanalysis facilities and personnel.

Chapter 5 Electrochemical Investigation of Copper in CuAAC Assembled Monolayers

Abstract

Cu(I)-catalysed azide–alkyne cycloaddition reactions were used in Chapter 4 as an efficient and high yielding reaction to attach a diverse set of functionalities to a surface. Copper contamination of these surfaces was detected so a further study of this was warranted. Copper contamination was investigated on two types of surfaces: amine-terminated and ferrocene-terminated with 1,8-nonadiyne-derived monolayers as a copper-free control. Copper contamination was observed in varying amounts by cyclic voltammetry on ferrocene-terminated surfaces with higher surface concentrations on P-type surfaces. Surfaces were further characterised by electrochemical impedance methods, showing a greater rate of electron transfer on P-type surfaces. Open circuit potentiometry was also investigated as a potentially simple method of copper detection, however this could not be correlated with the presence of copper using solely electrochemical methods.

5.1 Introduction

The Cu(I)-catalysed azide–alkyne cycloaddition (CuAAC) reaction provides an ideal platform for the modification of silicon surfaces [29, 174]. It is a reliable reaction for the attachment of a diverse range of functionalities [34, 46]. One of particular interest is the ferrocene moiety, which can be used as a redox probe on Si, which it is facile to determine coverage and electron transfer kinetics [39].

Due to usage of copper as a catalyst in the CuAAC reaction, it is important to remove it due to adverse effects of copper on the electrical properties of a system [175, 176], in particular acting as recombination centres [177], which can adversely affect the output of a triboelectric nanogenerator. Copper ions can be trapped as a stable acetylide [178], by surface oxide on silicon [179] or coordinated to by 1,2,3-triazoles [42].

Copper is a redox active metal and can be detected electrochemically, so open circuit potentiometry is a logical tool to detect copper. Copper has been successfully detected by using open circuit potential (OCP) methods to examine the deposition of copper from hydrofluoric acid solutions on to silicon electrodes [180-182] down to a parts per billion scale. Under these conditions, copper metal deposits on to the silicon surface, which can be seen by AFM and SEM. Copper surface concentrations were determined by total x-ray reflection fluorescence (TXRF) spectroscopy which allows measurement of very low surface concentrations of copper. All of these studies focused on the reduction of Cu^{2+} to Cu metal on bare silicon, however the system examined in this chapter involves Cu^{+} generated by the reduction of Cu^{2+} in solution by sodium ascorbate.

This chapter report attempts to measure copper contamination by a range of electrochemical procedures with an emphasis on the surfaces studied in Chapter 4. A range of silicon dopings and types was explored in an attempt to establish a link between doping and copper surface concentration which was observed in Chapter 4.

5.2 Synthesis of Clicked Monolayers

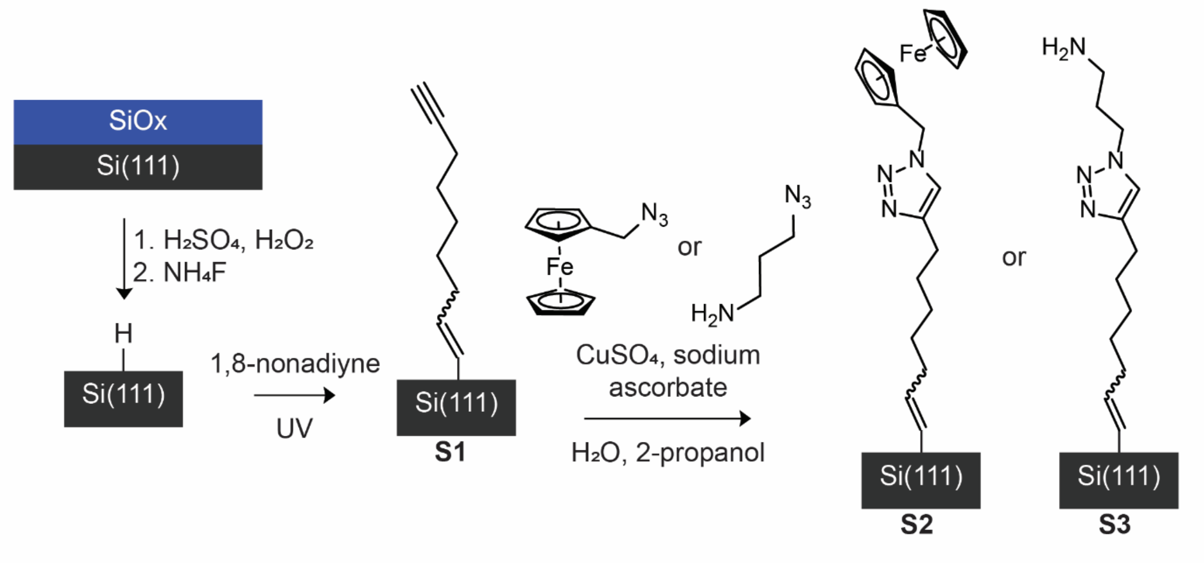

Figure 5.1: Synthesis of studied monolayers using typical methods to hydrogen-terminate the surface then a hydrosilylation and CuAAC strategy to assemble the monolayers of interest.

As shown in Figure 5.1, the native oxide on the silicon wafer is first cleaned by solvents and piranha solution and is then etched by ammonium fluoride to synthesise a hydrogen-terminated surface. The hydrogen-terminated surface is then reacted with 1,8-nonadiyne in a UV-catalysed hydrosilylation reaction to form the 1,8-nonadiyne modified **S1**. **S1** is then reacted in a CuAAC reaction with either azidomethylferrocene or 3-azidopropan-1-amine to form **S2** and **S3** respectively. These surfaces were cleaned with a range of solvents and 0.5 M hydrochloric acid in an attempt to remove all the Cu catalyst used in the CuAAC reaction .

S1 surfaces were chosen as a Cu-free platform for the further modification and electrochemical study. **S2** was selected as it contains a well-characterised redox probe [39]. **S3** was chosen as it was shown to trap the most copper in Chapter 4, so warranted further study to examine the possibility of determining the amount of copper on the surface electrochemically.

5.3 Cyclic Voltametric Studies of the Prepared Monolayers

Cyclic voltammetry was performed on all surfaces to examine their electrochemical properties. **S1** surfaces, as expected, showed no peaks in the studied range (0.2–0.7 V versus Ag/AgCl), an example of which is shown in Figure 5.2.

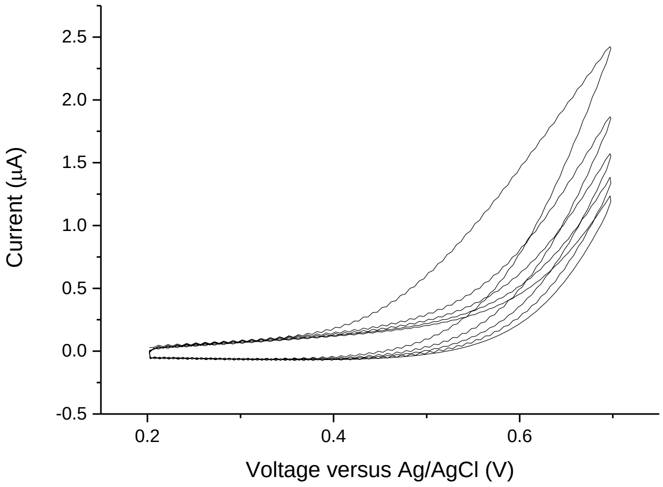

*Figure 5.2: Cyclic voltammogram of highly doped N-type **S1** surface at 100 mV/s scan rate (5 cycles)*

S3 surfaces however were expected to show peaks corresponding to the oxidation of Cu trapped on the surface after the CuAAC reaction, however this peak was only seen once on a lowly-doped P-type surface and never on other doped surfaces. Only an oxidation peak could be seen however at 0.60 V versus Ag/AgCl at 100 mV/s scan rate with no clear reduction peak observed as seen in Figure 5.3. Surface concentration was seen to decrease with each scan as shown in Figure 5.4, which is attributed to the solubilisation of Cu(II) or the interference of the oxidation of the surface.

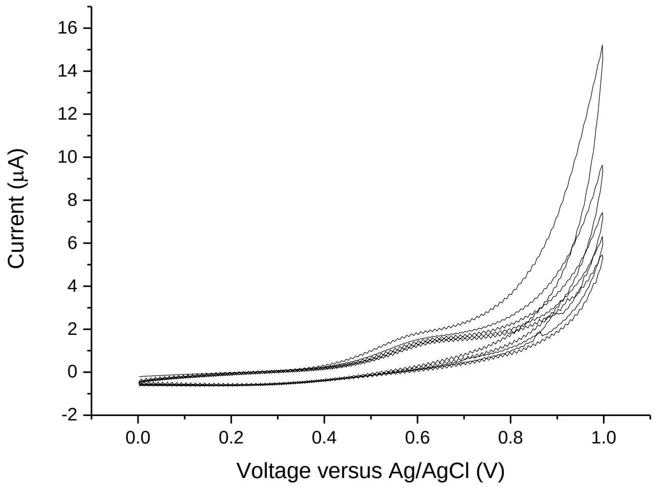

Figure 5.3: Cyclic voltammogram of lowly doped P-type S3 surface at 100 mV/s scan rate (5 cycles), showing the presence of copper

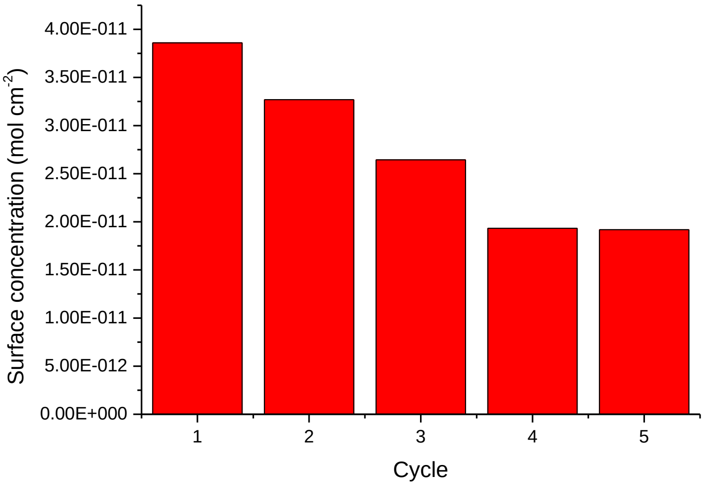

Figure 5.4: Surface concentration as determined from anodic peak of cyclic voltammogram in Figure 5.3

Cyclic voltammetry on **S2** surfaces proved to be of more interest however with a redox active ferrocene moiety tethered to the surface.

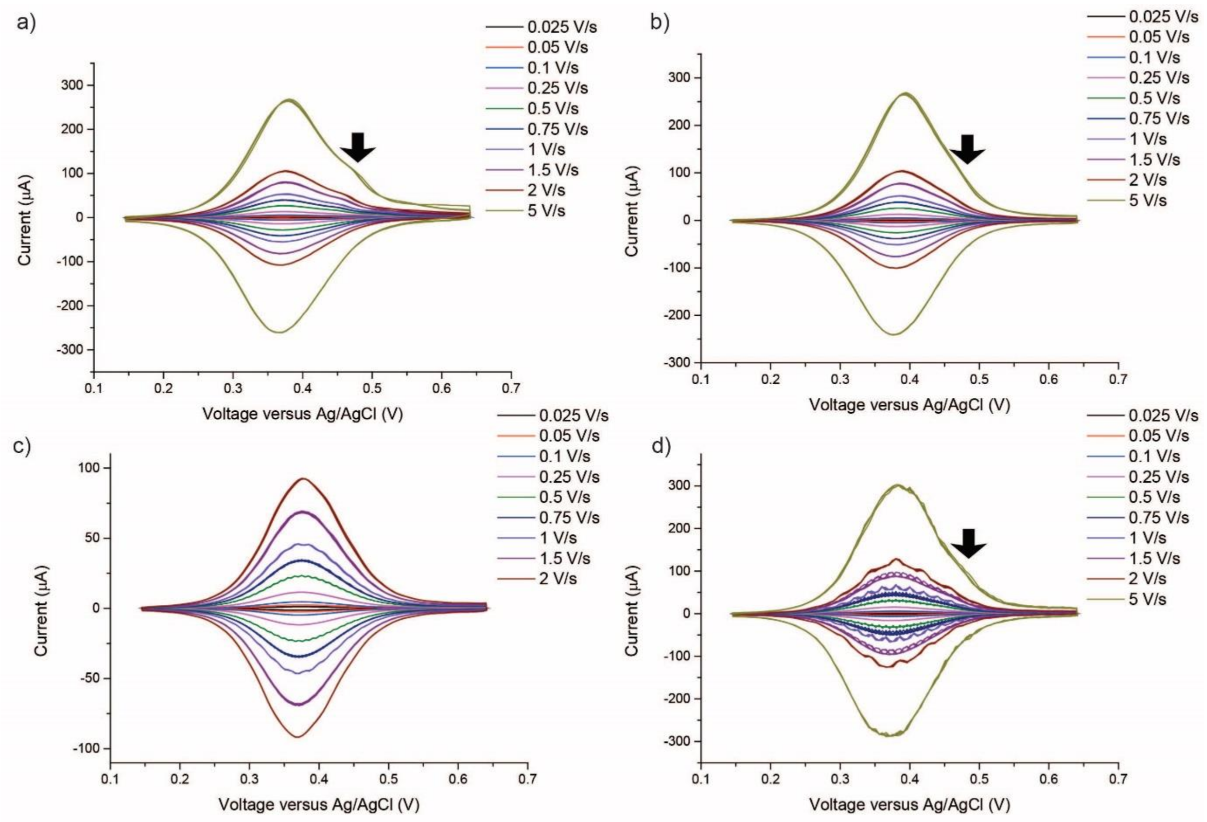

Figure 5.5: Cyclic voltammograms of four lowly doped P-type S2 surfaces at a range of scan rate with Cu shoulder peak annotated by an arrow. a) Sample 1, b) sample 2, c) sample 3, d) sample 4

Lowly doped P-type surfaces showed reproducible voltammetry with a consistent $E_{1/2}$ of 0.355 V across all samples as shown in Figure 5.5. This agrees with previous reports of the $E_{1/2}$ of ferrocene bound in this monolayer [163]. A small peak is seen in Figure 5.5 a) at 0.46 V in the oxidation peak which is attributed to Cu oxidation. This peak is also tentatively assigned in Figure 5.5 b) and d). No corresponding reduction peak could be observed for this however. Even with consistent sample preparation, differing amounts the peak attributed to Cu were observed, which shows that minor inconsistencies in sample preparation leads to significantly different amounts of Cu observed. It would also appear that ferrocene is required to see this Cu peak.

These ferrocene films exhibit CV waves with a full width at half maximum (hence fwhm) for both oxidation and reduction at 250 mV/s of a) 0.141 V, b) 0.124, c) 0.127, d) 0.126 V. This is greater than the ideal fwhm from the Langmuir isotherm for a Nernstian process of 90.6 mV. This can be explained by repulsive interactions between ferrocene moieties [183]. The fwhm is also affected by the peak attributed to Cu oxidation, increasing it by a small amount.

High coverage was observed for all surfaces with a coverage of 2.43×10^{-10} mol cm^{-2} corresponding to a fractional coverage of a complete monolayer of close packed ferrocenes of 0.54. This is comparable to previous reports [163], showing a high efficiency of the CuAAC reaction.

Extremely fast kinetics were observed for these surfaces with a maximum peak splitting of 9 mV at 5 V s^{-1}. This does not allow us to use Laviron’s formalism based on the peak splitting to determine the kinetics [184], however electrochemical impedance spectroscopy can be used in these cases and is further discussed later in Section 5.4.

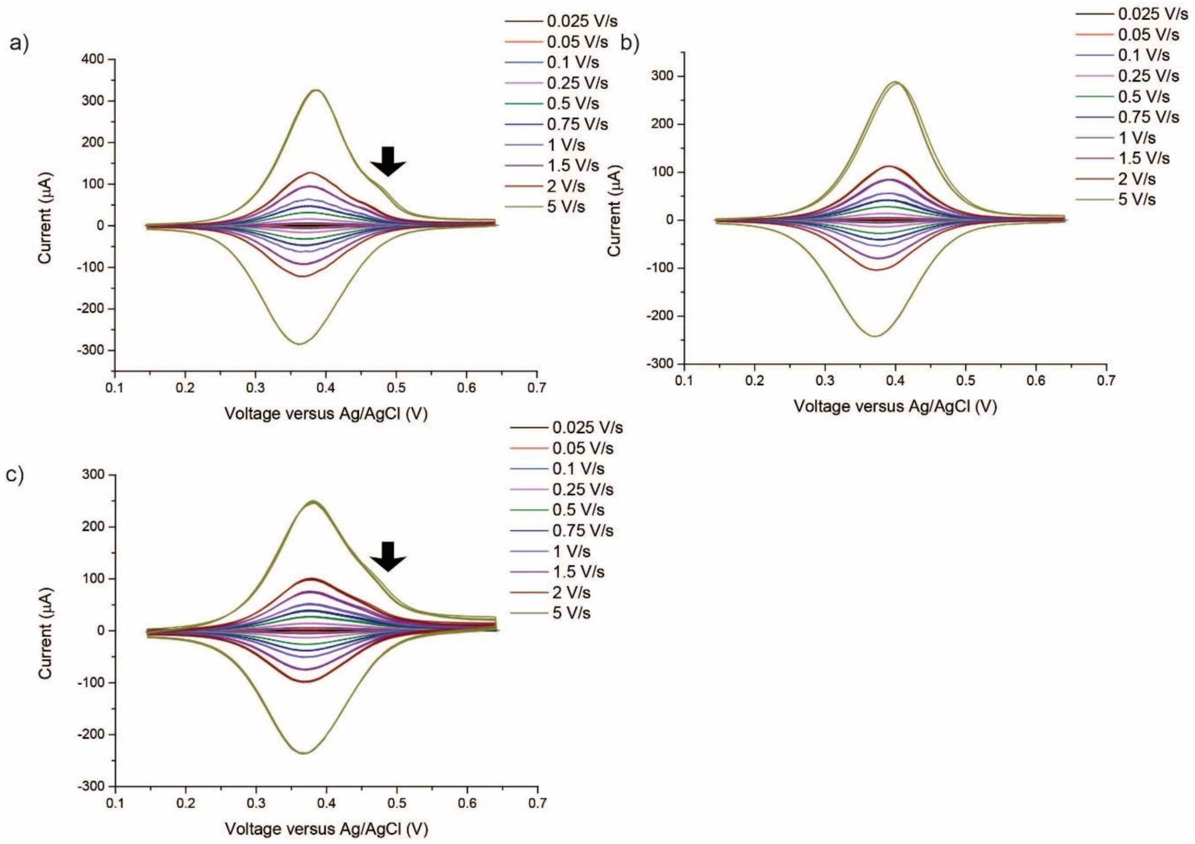

Figure 5.6: Cyclic voltammograms of three highly doped P-type S2 surfaces at a range of scan rate with Cu shoulder peak annotated by an arrow. a) Sample 1, b) sample 2, c) sample 3

Highly doped P-type surfaces showed similarly reproducible voltammetry with a consistent $E_{1/2}$ of 0.355 V, similar to lowly doped P-type. A similar peak attributed to copper oxidation at 0.46 V was seen in Figure 5.6 a) and is tentatively assigned in Figure 5.6 c). The fwhm of these peaks is reflective of similar interactions to those seen in Figure 5.5, with slightly larger than ideal fwhms. At 250 mV s^{-1}, the fwhm for a) were 0.117 V for the oxidation peak and 0.126 V for the reduction peak, for b) were 0.109 V for the oxidation peak and 0.110 V for the reduction peak and for c) were 0.131 V for the oxidation peak and 0.123 V for the reduction peak. The largest peak splitting was observed in b) with a splitting of 29 mV. It is also the peak with the smallest copper oxidation peak, suggesting that the copper may play a role in catalysing the oxidation and reduction of the ferrocene moieties as the peak splitting is reflective of the kinetics of this reaction. The mechanism by which this occurs is unclear and requires further investigation. Again, high coverages were observed with an average coverage of 2.43×10^{-10} mol cm^{-2} corresponding to a fractional coverage of a complete monolayer of close packed ferrocenes of 0.54.

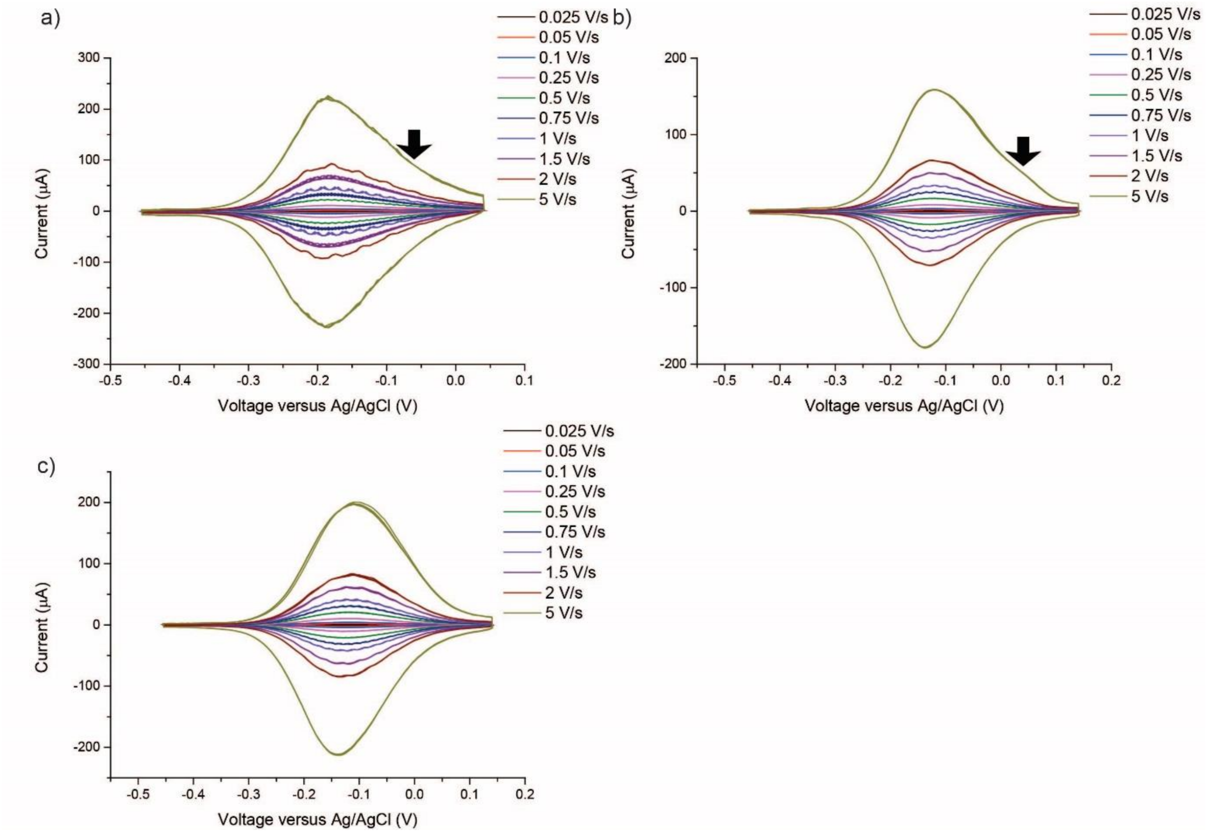

Figure 5.7: Cyclic voltammograms of three lowly doped N-type S2 surfaces at a range of scan rates under illumination. a) Sample 1, b) sample 2, c) sample 3

Lowly doped N-type **S2** surfaces were illuminated to ensure sufficient kinetics to determine the coverage and ensure close to ideal kinetics [87]. The $E_{1/2}$ of a) (−0.186 V) was substantially different for those determined for b) (−0.126 V) and c) (−0.128 V). This is attributed to a difference in light intensity, as an increase in light intensity shifts the peak to a more negative value. Noticeable asymmetry was seen in **Error! Reference source not found.** a) and b), which again is tentatively assigned to the oxidation of Cu. Greater fwhms were observed for these surfaces than the p-type surfaces, due to an increase in interactions between ferrocene moieties and the surface. At 250 mV s^{-1}, the fwhm for a) were 0.143 V for the oxidation peak and 0.173 V for the reduction peak, for b) were 0.175 V for the oxidation peak and 0.170 V for the reduction peak and for c) were 0.175 V for the oxidation peak and 0.170 V for the reduction peak. Small peak splittings were observed again, similar to lowly doped and highly doped P-type silicon. Again, high coverages were observed with an average coverage of 2.15×10^{-10} mol cm^{-2} corresponding to a fractional coverage of a complete monolayer of close packed ferrocenes of 0.48. This is somewhat lower than that observed for lowly doped and highly doped P-type.

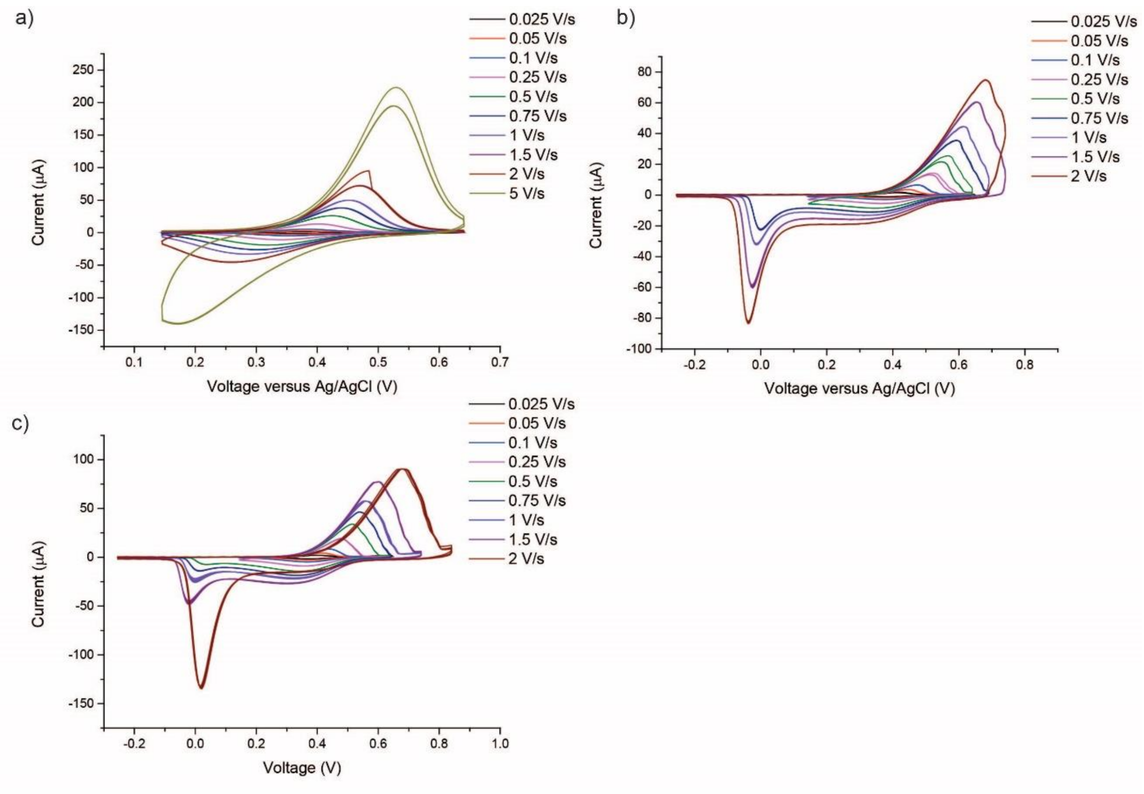

Figure 5.8: Cyclic voltammograms of highly doped N-type S2 surfaces at a range of scan rates. a) Sample 1, b) sample 2, c) sample 3

It is immediately apparent from the CV data that there is a distinct difference between highly doped N-type from the other studied dopings. There is a clear second reduction peak in Figure 5.8 b) and c). This corresponds to a pronounced stabilisation of the ferrocenium moiety at higher scan rates. We attribute this to ferrocene as the anodic and cathodic coverages are the same by integration and no clear peaks that could feasibly be attributed to copper can be seen. This peak was not observed in Figure 5.8 a) as the scan window was not wide enough to see these peaks, however there is a corresponding difference in the cathodic coverage versus the anodic coverage, suggesting the possible presence of it. In Figure 5.8 a), there is a difference between the fwhm of the peaks at 250 mV s^{-1} in the anodic (0.108 V) and cathodic (0.136 V) direction, suggesting a greater interaction of the oxidised ferrocenium moieties on the highly doped N-type than on other surfaces.

5.4 Electrochemical Impedance Spectroscopy

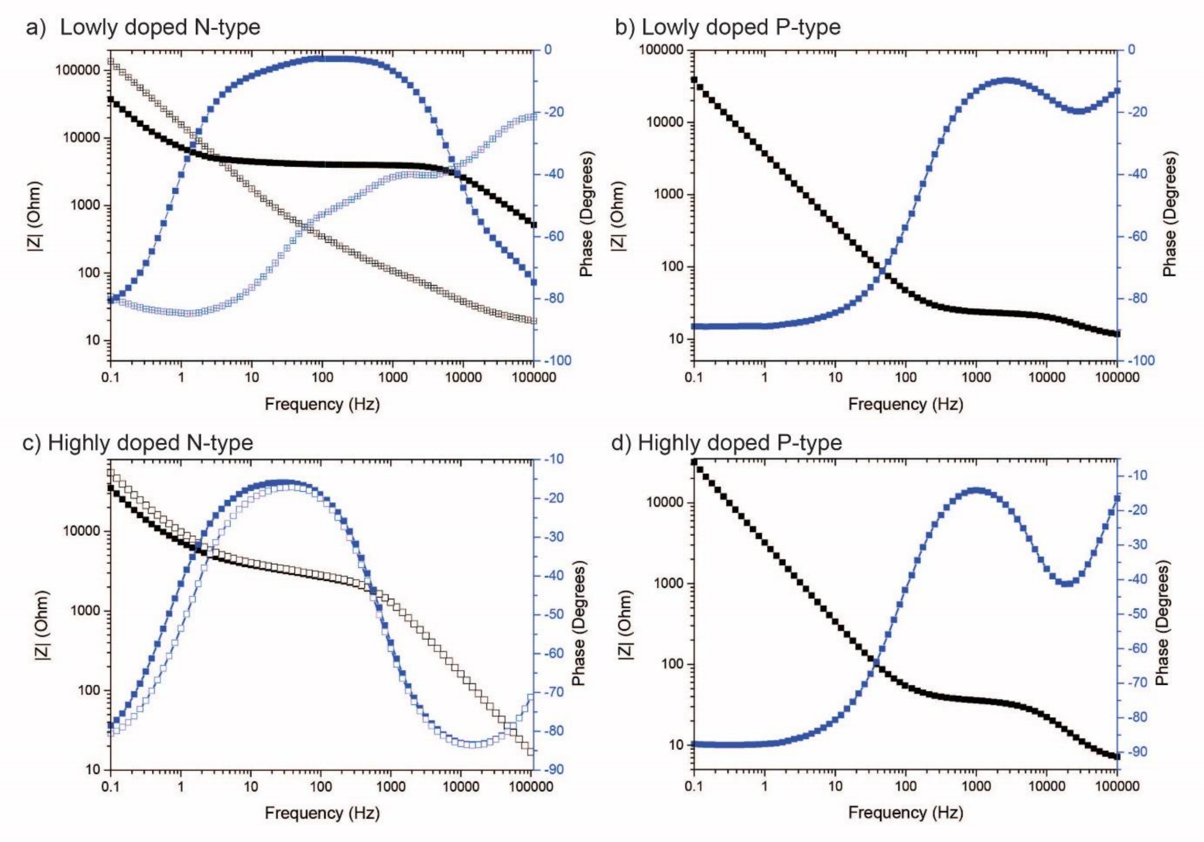

Figure 5.9: Bode plots of S2 surfaces on a) lowly-doped N-type silicon with filled squares for dark EIS and crossed squares for red illuminated EIS, b) lowly-doped P-type silicon, c) highly-doped N-type silicon with filled squares for initial EIS and empty squares for EIS after obtaining cyclic voltammograms, d) highly-doped P-type silicon.

Impedances can be measured over a broad range of frequencies to allow us to estimate individual elements of an electrical circuit to model the kinetics of the redox reaction of the ferrocene on **S2** surfaces. Bode plots, as Figure 5.9, show visually the electrochemical kinetics. As the AC frequency becomes close to the time constant of the redox reaction, the phase and the gradient of the |Z| versus frequency plot reach a minimum. It becomes readily apparent then that the doping has a significant effect on the kinetics of the redox reaction from **Error! Reference source not found.**. A quantitative treatment of the kinetics can be achieved by a fitting of the data to the model Randles circuit as shown in Figure 5.10. Capacitances are treated as constant phase elements due to inhomogeneity in the electrochemical system e.g. kinetic dispersion [185].

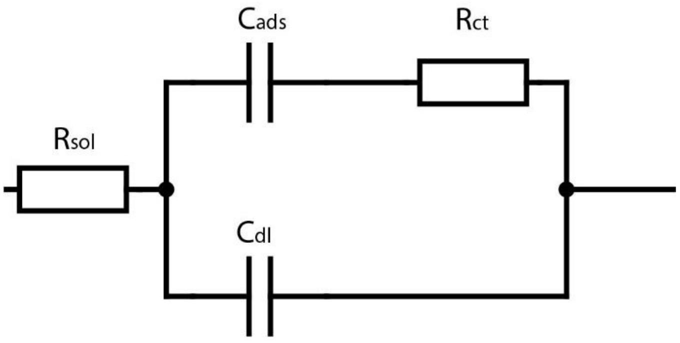

Figure 5.10: Model Randles circuit for EIS fitting. R_{sol} is the solution resistance, C_{ads} is the adsorption pseudo-capacitance, R_{ct} is the charge transfer resistance and C_{dl} is the double layer capacitance.

Table 5.1: EIS fitting data from Figure 5.9. Errors are determined from fitting

Doping and condition	R_{sol} (Ω)	C_{dl} (F)	C_{dl} phase (°)	R_{ct} (Ω)	C_{ads} (F)	C_{ads} phase (°)	k_{et} (s^{-1})	χ^2
Lowly doped N-type dark	0 ±11	1.6×10^{-8} $\pm0.2\times10^{-8}$	0.879 ±0.008	4.24×10^{3} $\pm0.03\times10^{3}$	4.05×10^{-5} $\pm0.05\times10^{-5}$	0.9112 ±0.006	2.91 ±0.06	0.0015
Lowly doped N-type illuminated	19.0 ±0.7	4×10^{-8} $\pm1\times10^{-8}$	0.82 ±0.02	2.1×10^{2} $\pm0.2\times10^{2}$	8×10^{-6} $\pm1\times10^{-6}$	0.94 ±0.02	3.1×10^{2} $\pm0.2\times10^{2}$	0.0065
Lowly doped P-type	10.4 ±0.2	2.7×10^{-6} $\pm0.5\times10^{-6}$	0.88 ±0.01	14.1±0.3	4.16×10^{-5} $\pm0.05\times10^{-5}$	0.989 ±0.001	8.5×10^{2} $\pm0.3\times10^{2}$	0.00026
Highly doped N-type pre-CV	3.3± 0.8	1.7×10^{-7} $\pm0.1\times10^{-7}$	0.949± 0.007	3.05×10^{3} $\pm0.06\times10^{3}$	4.3×10^{-5} $\pm0.1\times10^{-5}$	0.78 ±0.01	3.8±0.2	0.0052
Highly doped N-type post-CV	3.4± 0.7	1.7×10^{-7} $\pm0.1\times10^{-7}$	0.952± 0.006	3.19×10^{3} $\pm0.05\times10^{3}$	2.68×10^{-5} $\pm0.05\times10^{-5}$	0.818 ±0.008	5.9±0.2	0.0041
Highly doped P-type	6.44 ±0.09	1.5×10^{-6} $\pm0.1\times10^{-6}$	0.934± 0.007	31.5 ± 0.3	5.07×10^{-5} ± 0.03×10^{-5}	0.974 ±0.001	314±5	0.00042

.

Fitted data are displayed Table 5.1. High quality fits ($\chi^2 < 0.0005$) were obtained on both P-type surfaces however the fits on N-type surfaces were of lower quality ($\chi^2 < 0.0065$). EIS was used to determine the kinetics of the ferrocene/ferrocenium redox reaction via the formalism developed by Laviron [186, 187], that is $\frac{1}{2R_{ct}C_{ads}} = k$, where R_{ct} is the charge transfer resistance, C_{ads} is the adsorption pseudo-capacitance and k is the time constant of the redox reaction. The redox reaction was observed to be much faster on P-type surfaces than N-type, except where the lowly doped N-type surface was illuminated, bringing the kinetics much closer to those of the P-type surfaces. The P-type surfaces have a much lower charge transfer resistance than N-type, suggesting a greater difficulty in charge transfer from the ferrocene moiety to the N-type silicon attributed to these surfaces being in depletion.

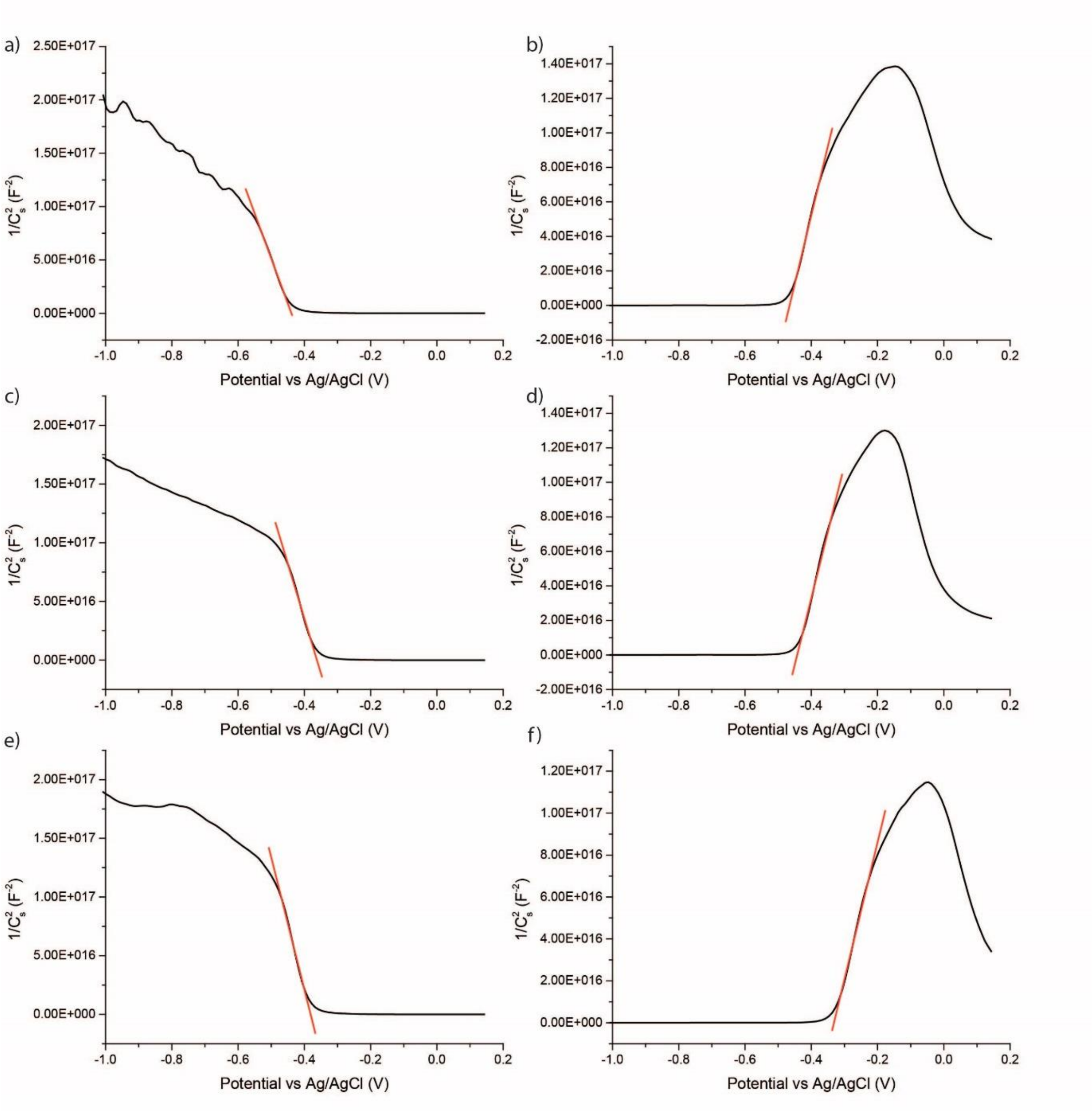

Figure 5.11: Mott-Schottky plots at 10 kHz of prepared surfaces (black) with linearly fit and extrapolated region (red) to determine the flat band potential. a) Lowly-doped P-type S1, b) lowly-doped N-type S1, c) lowly-doped P-type S2, d) lowly-doped N-type S2, e) lowly-doped P-type S3, f) lowly doped N-type S3.

The flat band potential is of interest as at it, there is no depletion layer in the junction between the silicon surface and the electrolyte. We can then use this flat band potential to determine whether the surface is in depletion or accumulation, which is of relevance as this affects the electron transfer kinetics.

Mott-Schottky plots, shown in Figure 5.11, are used to determine the flat band potential via the following equations [188] where C_s is the capacitance, ε_{Si} is the permittivity of Si, ε_0 is the permittivity of free space, q is the elementary charge, N_A is the number of acceptors or donors, V_s is the applied voltage, V_{fb} is the flat band potential, k_B is Boltzmann's constant and T is the temperature:

$$\frac{1}{C_S^2} = \left(\frac{2}{q\,\varepsilon_{Si}\varepsilon_0 N_A}\right)\left(\left|V_s - V_{fb}\right| - \frac{k_B T}{q}\right) \qquad \text{(Equation 5.1)}$$

$$V_S^{extrapolated} - \frac{k_B T}{q} = V_{fb} \qquad \text{(Equation 5.2)}$$

A linear fit is performed to the linear region to find the intercept with the x-axis, which is the $V_S^{\text{extrapolated}}$ and the flat band potential can be determined from this value. Values of flat band potentials determined from Figure 5.11 are shown in Figure 5.12.

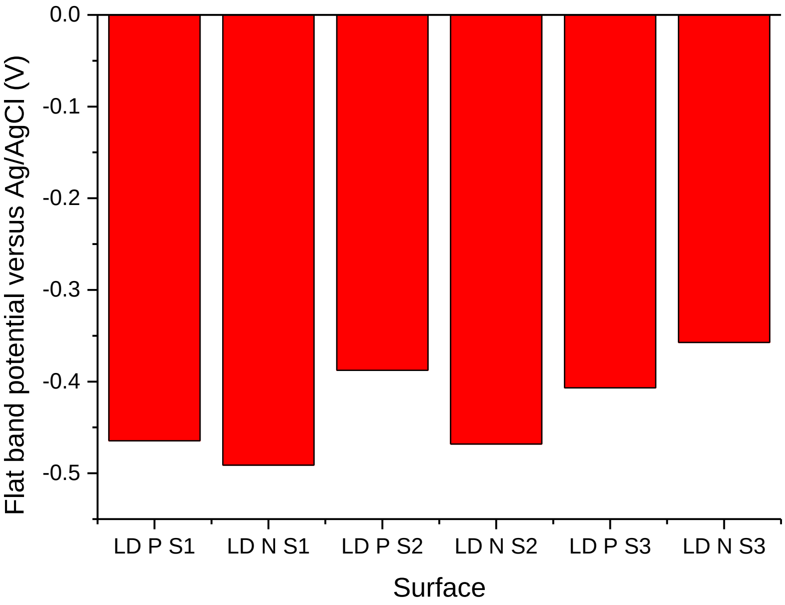

Figure 5.12: Flat band potential as determined from extrapolation of Mott-Schottky plots

5.5 Open Circuit Potentiometry

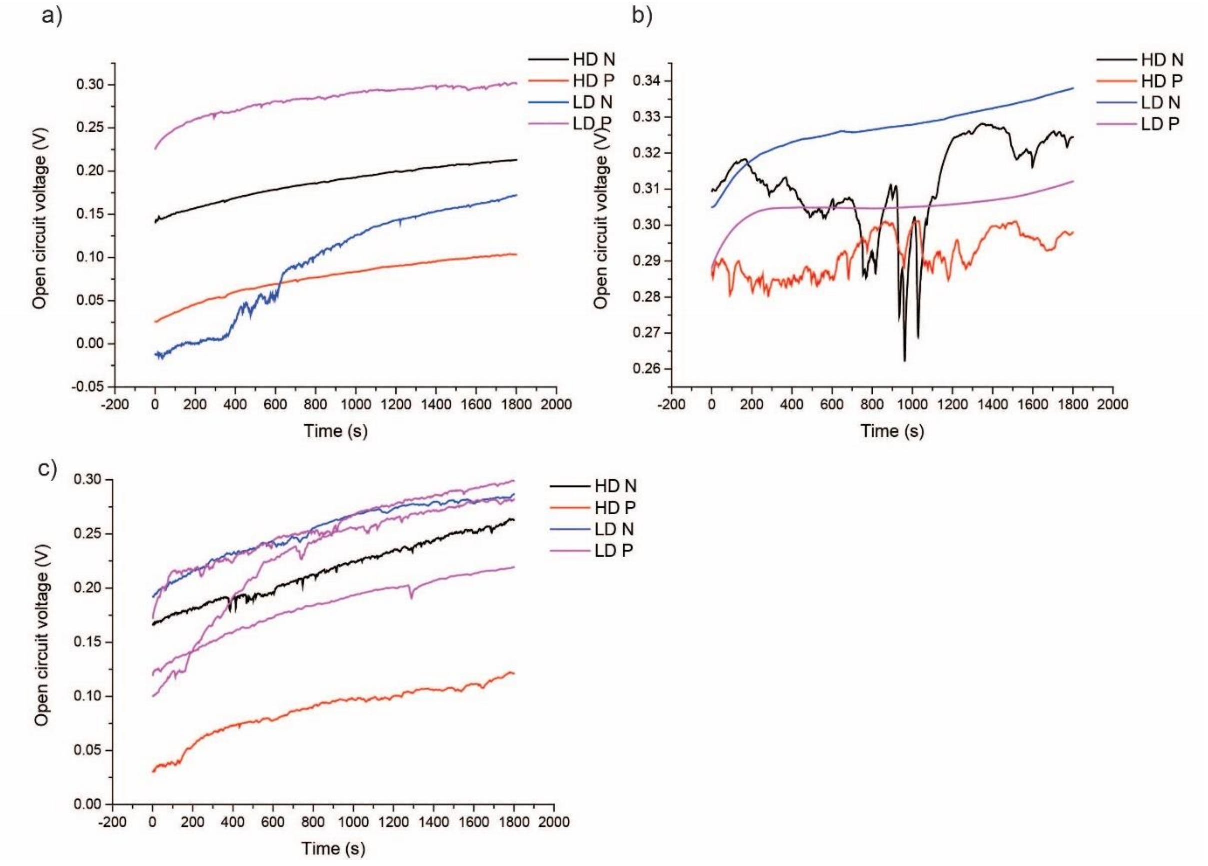

Figure 5.13: Open circuit voltages versus Ag/AgCl for a) ***S1*** *surfaces, b)* ***S2*** *surfaces and c)* ***S3*** *surfaces.*

Open circuit potential (OCP) measurement is a simple procedure to determine how difficult a surface is to oxidise and a measure of the rate of oxidation of the surface [189]. For **S1** surfaces in Figure 5.13 a), slight oxidation of the surfaces is seen by a small increase in the OCP over the studied time, with the greatest level of oxidation seen on lowly doped N-type silicon. It is apparent from the small change in OCP that the 1,8-nonadiyne-derived monolayer effectively protects the underlying silicon from oxidation. This was also used as a copper-free control surface.

For **S2** surfaces in Figure 5.13 b), the OCP was dominated by the presence of the unoxidised ferrocene moieties on the surface. Only small trends corresponding to oxidation of the surface were seen, however on highly doped surfaces, the OCP was much less stable, showing fluctuations of up to 40 mV. These sharp changes were seen to be reversible however and there is only a weak positive trend of the OCP. The lowly doped surfaces were seen to oxidise slightly however substantially less so than the **S1** surfaces.

For **S3** surfaces in Figure 5.13 c), similar trends to **S1** surfaces were observed, except for lowly doped N-type, which was seen to be more resistant to oxidation than the corresponding **S1** surface. These surfaces showed a greater change in OCP than the corresponding **S1** surface. This suggests an increase in the rate of oxidation of these **S3** surfaces. The amine of these surfaces is likely to be protonated as the electrolyte used is 1 M $HClO_4$, a strong acid, which could encourage oxidation by increasing the monolayer wettability, which increases the contact with water.

Lowly doped P-type was repeated three times to try to determine a correlation between the presence of copper and the OCP, however no copper could be detected by CV, so it was not possible to establish a correlation between the two. There are small differences in the OCP between each of the three trials, which may suggest a link between the OCP and the residual copper trapped in the monolayer, however this could also be attributed to small differences in the monolayer giving rise to a greater degree of accessible sites for oxidation.

5.6 Conclusions

Hydrosilylation and Cu(I)-catalysed azide–alkyne cycloaddition reactions were used to prepare a range of monolayers with a range of functionalities. Copper was attempted to be detected electrochemically and was observed in varying amounts on **S2** surfaces by cyclic voltammetry, with peaks attributed to copper on **S2** surfaces were seen more strongly on P-type surfaces. The kinetics of electron transfer to the ferrocene moiety on **S2** surfaces were observed to depend strongly on the doping of the underlying silicon, which may suggest a connection between the presence of copper in the monolayer and the kinetics of electron transfer. This raises the further question of whether these variations are due to varying amounts of Cu versus varying interactions between Cu and ferrocene moieties. Of interest would be determining the equilibrium constant for this process however this is beyond the scope of this thesis. Open circuit potential did not show a clear correlation between the presence of copper and the measured potential, however further work is needed to accurately quantify the presence of copper on these surfaces.

Chapter 6 Conclusions and Future Outlook

6.1 Conclusions

Chapter Three examined pyramidally textured surfaces with an emphasis on the zero-bias tribocurrent. We aimed to examine the effects of Si(100)/(111) junction on the tribocurrent output of a moving Pt/Si Schottky diode. Si(100) surfaces were etched with potassium hydroxide to generate pyramids with Si(111) faces and were then studied using the PF-TUNA AFM mode. The zero-bias tribocurrent was observed to peak at the boundary between the Si(100) of the wafer and the Si(111) of the pyramid surfaces. This was attributed to a thinning in the space charge layer at this concave boundary. On lowly doped N-type silicon, float zone process silicon was shown to give a greater zero-bias tribocurrent than Czochralski process silicon due to the longer hole lifetime and greater diffusion length. Lowly doped P-type and highly doped N-type silicon showed negligibly small currents under PF-TUNA conditions. Greater zero-bias tribocurrent was also seen for larger pyramids with a concomitant greater localisation at the edges of the pyramid. This work removes constraints to further miniaturisation of these devices by enhancing the localisation of the highest current outputs.

Chapter Four exploited a range of surface chemistries on Si(111) to examine the interaction of surface chemistry, friction and zero-bias tribocurrent of a moving Pt/Si Schottky diode. Si(111) surfaces of different doping types were modified with a range of terminal functionalities by a CuAAC reaction: alkyne, alcohol, amine and methyl. Characterisation of these surfaces by XPS, contact angle measurements, and cyclic voltammetry revealed minimal differences of the surfaces due to doping. Minimal oxidation was seen by XPS indicating the monolayers protect the underlying silicon from oxidation effectively. A considerable difference in work function was observed between the P-type and N-type silicon however, which was, in part, due to the presence of trapped copper in these monolayers which was greater on P-type silicon.

AFM was used to simultaneously observe the topography, zero-bias tribocurrent and friction on these surfaces. Friction was greater on the P-type and N-type surfaces with the polar functionalities: amine and alcohol. Friction coefficients on N-type silicon were much greater than those on P-type silicon with the same monolayer, even though minimal differences were observed in the other characterisation experiments. This effect was more pronounced on the monolayers containing the 1,2,3-triazole from the CuAAC reaction than the monolayer prepared without, suggesting that the 1,2,3-triazole in the backbone of the monolayer is non-innocent in the electronic contribution to friction. The greatest currents were seen on the surfaces with the greatest friction coefficients, highlighting the link between friction and zero-bias tribocurrent.

Chapter Five aimed to study the effects of copper trapped in monolayers on the electrochemical properties of these surfaces, with an view towards simple detection using open circuit potentiometry. The presence of copper was studied in two CuAAC-derived monolayers with a control of an unmodified 1,8-nonadiyne-derived monolayer. Copper was detected by cyclic voltammetry on the ferrocene-terminated monolayers on P-type surfaces in varying amounts suggesting the method used to remove copper, primarily 0.5 M hydrochloric acid, was insufficient, however this method was generally effective on amine-terminated monolayers. Electrochemical impedance methods were also used to study these monolayers and showed much faster electron transfer kinetics on P-type compared to N-type surfaces regardless of level of doping. Open circuit potentiometry was attempted to be used to study the presence of copper in these monolayers, however, as no copper oxidation peak was observed by cyclic voltammetry for these surfaces, the presence of copper could not be correlated with the change in open circuit potential.

6.2 Future Outlook

Triboelectric nanogenerators built from moving Schottky diodes based on silicon are a promising technology, however further work is needed before commercialisation is achievable.

Scaling up of these diodes to a macroscopic scale without the concomitant loss of power density as seen in Chapter 3 is an important goal. The use of surfaces that can conform to the pyramidally textured surfaces would hopefully lead to a capturing of the enhancement of current seen at the Si(111)/(100) boundaries. Soft contacts such as conductive polymers or liquid metals would be a platform worthy of study.

A study of the friction measured on these Si(111) pyramids would also be of interest. Adhesions on the pyramids versus off the pyramids were seen to be inconsistent in direction, with adhesions on the pyramids sometimes being higher than the surrounding flat surface and sometimes lower. A more detailed examination of the relationship between the static mechanical and electrical properties with a view towards the effects of flexoelectricity would be warranted to examine the effect on the triboelectricity.

As we contend that one of the factors increasing the current is the electronic contrast between the Si(111) and Si(100) surfaces, it is of interest to exploit this on a flat surface without having to worry about the difficulty of having a surface conform to the pyramidally textured surface. This could be achieved in a spatially controlled manner by using microcontact printing or dip pen nanolithography to attach monolayers using a CuAAC reaction to examine the effects of surface chemistry or by boron implantation into an N-type wafer to examine the effects of doping.

The long-term stability of the surfaces studied in Chapter 4 is of concern, so long term experiments should be undertaken to ascertain the stability. In the limited experiments on surfaces that were left exposed to the atmosphere for extended periods of time, unusual results were seen, such as negative friction coefficients, which were attributed to the water layer deposited on the surface wearing away or reorganising and very high current outputs that decreased exponentially with scanning under AFM, which were attributed to oxidation of the silicon underneath the monolayer.

For chapter 5, a more thorough determination of the surface concentration of copper is required. Total reflection x-ray fluorescence (TXRF) spectroscopy is an ideal choice of tool to determine this. A closer inspection of the oxidation state of the copper deposited on the surface is also of value as this can be determined by XPS. It is also suggested for further work with these types of monolayers that metal-free reactions are used to entirely avoid the issue of copper contamination.

Chapter 7 References

[1] Z.L. Wang, Entropy theory of distributed energy for internet of things, Nano Energy, 58 (2019) 669-672. https://doi.org/10.1016/j.nanoen.2019.02.012.

[2] X. Li, Z.-H. Lin, G. Cheng, X. Wen, Y. Liu, S. Niu, Z.L. Wang, 3D Fiber-Based Hybrid Nanogenerator for Energy Harvesting and as a Self-Powered Pressure Sensor, ACS Nano, 8 (2014) 10674-10681. https://doi.org/10.1021/nn504243j.

[3] K. Fujii, H. Bettin, P. Becker, E. Massa, O. Rienitz, A. Pramann, A. Nicolaus, N. Kuramoto, I. Busch, M. Borys, Realization of the kilogram by the XRCD method, Metrologia, 53 (2016) A19-A45. https://doi.org/10.1088/0026-1394/53/5/a19.

[4] W.R. Runyan, Growth of Large Diameter Silicon and Germanium Crystals by the Teal-Little Method, Review of Scientific Instruments, 30 (1959) 535-540. https://doi.org/10.1063/1.1716676.

[5] W. von Ammon, FZ and CZ crystal growth: Cost driving factors and new perspectives, physica status solidi (a), 211 (2014) 2461-2470. https://doi.org/10.1002/pssa.201400043.

[6] W.G. Pfann, Zone Melting, Science, 135 (1962) 1101-1109. https://doi.org/10.1126/science.135.3509.1101.

[7] C.-S. Tan, P.-L. Hsieh, L.-J. Chen, M.H. Huang, Silicon Wafers with Facet-Dependent Electrical Conductivity Properties, Angew. Chem. Int. Ed., 56 (2017) 15339-15343. https://doi.org/10.1002/anie.201709020.

[8] J.A. Dillon, H.E. Farnsworth, Work Function and Sorption Properties of Silicon Crystals, Journal of Applied Physics, 29 (1958) 1195-1202. https://doi.org/10.1063/1.1723401.

[9] C.-H. Kuo, C.-P. Liu, S.-H. Lee, H.-Y. Chang, W.-C. Lin, Y.-W. You, H.-Y. Liao, J.-J. Shyue, Effect of surface chemical composition on the work function of silicon substrates modified by binary self-assembled monolayers, Physical Chemistry Chemical Physics, 13 (2011) 15122-15126. https://doi.org/10.1039/C1CP20590K.

[10] A. Novikov, Experimental measurement of work function in doped silicon surfaces, Solid-State Electronics, 54 (2010) 8-13. https://doi.org/10.1016/j.sse.2009.09.005.

[11] O. Shimomura, S. Minomura, N. Sakai, K. Asaumi, K. Tamura, J. Fukushima, H. Endo, Pressure-induced semiconductor-metal transitions in amorphous Si and Ge, The Philosophical Magazine: A Journal of Theoretical Experimental and Applied Physics, 29 (1974) 547-558. https://doi.org/10.1080/14786437408213238.

[12] Y. Sun, S.E. Thompson, T. Nishida, Physics of strain effects in semiconductors and metal-oxide-semiconductor field-effect transistors, Journal of Applied Physics, 101 (2007) 104503. https://doi.org/10.1063/1.2730561.

[13] L. Sun, L. Zhu, C. Zhang, W. Chen, Z. Wang, Mechanical Manipulation of Silicon-based Schottky Diodes via Flexoelectricity, Nano Energy, 83 (2021) 105855. https://doi.org/10.1016/j.nanoen.2021.105855.

[14] A.K. Tagantsev, Piezoelectricity and flexoelectricity in crystalline dielectrics, Physical Review B, 34 (1986) 5883-5889. https://doi.org/10.1103/PhysRevB.34.5883.

[15] R.L. Sheridan, C.M. Ryan, W.C. Quinby, J. Blair, R.G. Tompkins, J.F. Burke, Emergency management of major hydrofluoric acid exposures, Burns, 21 (1995) 62-64. https://doi.org/10.1016/0305-4179(95)90785-X.

[16] G.S. Higashi, R.S. Becker, Y.J. Chabal, A.J. Becker, Comparison of Si(111) surfaces prepared using aqueous solutions of NH4F versus HF, Applied Physics Letters, 58 (1991) 1656-1658. https://doi.org/10.1063/1.105155.

[17] M. Niwano, Y. Takeda, Y. Ishibashi, K. Kurita, N. Miyamoto, Morphology of hydrofluoric acid and ammonium fluoride-treated silicon surfaces studied by surface infrared

spectroscopy, Journal of Applied Physics, 71 (1992) 5646-5649. https://doi.org/10.1063/1.350497.

[18] U. Neuwald, H.E. Hessel, A. Feltz, U. Memmert, R.J. Behm, Wet chemical etching of Si(100) surfaces in concentrated NH4F solution: formation of (2 × 1)H reconstructed Si(100) terraces versus (111) facetting, Surface Science, 296 (1993) L8-L14. https://doi.org/10.1016/0039-6028(93)90133-5.

[19] S. Rahpeima, E.M. Dief, S. Ciampi, C.L. Raston, N. Darwish, Impermeable Graphene Oxide Protects Silicon from Oxidation, ACS Applied Materials & Interfaces, 13 (2021) 38799-38807. https://doi.org/10.1021/acsami.1c06495.

[20] W. Kern, Chemical etching of silicon, germanium, gallium arsenide, and gallium phosphide, RCA Rev, 39 (1978) 278-308.

[21] M.J. Declercq, L. Gerzberg, J.D. Meindl, Optimization of the Hydrazine-Water Solution for Anisotropic Etching of Silicon in Integrated Circuit Technology, Journal of The Electrochemical Society, 122 (1975) 545-552. https://doi.org/10.1149/1.2134257.

[22] T. Song-Sheng, M. Reed, H. Hongtao, R. Boudreau, Morphology of etch hillock defects created during anisotropic etching of silicon, Journal of Micromechanics and Microengineering, 4 (1994) 147. https://doi.org/10.1088/0960-1317/4/3/008.

[23] R.A. Sinton, K. Young, J.Y. Gan, R.M. Swanson, 27.5-percent silicon concentrator solar cells, IEEE Electron Device Letters, 7 (1986) 567-569. https://doi.org/10.1109/EDL.1986.26476.

[24] G. Le Saux, A. Magenau, T. Böcking, K. Gaus, J.J. Gooding, The Relative Importance of Topography and RGD Ligand Density for Endothelial Cell Adhesion, PLOS ONE, 6 (2011) e21869. https://doi.org/10.1371/journal.pone.0021869.

[25] L. Wang, U.S. Schubert, S. Hoeppener, Surface chemical reactions on self-assembled silane based monolayers, Chemical Society Reviews, 50 (2021) 6507-6540. https://doi.org/10.1039/D0CS01220C.

[26] J.Y. Park, Y. Qi, P.D. Ashby, B.L.M. Hendriksen, M. Salmeron, Electrical transport and mechanical properties of alkylsilane self-assembled monolayers on silicon surfaces probed by atomic force microscopy, The Journal of Chemical Physics, 130 (2009) 114705. https://doi.org/10.1063/1.3089789.

[27] T. Ikeda, K. Tahara, T. Kadoya, H. Tajima, N. Toyoda, S. Yasuno, Y. Ozawa, M. Abe, Ferrocene on Insulator: Silane Coupling to a SiO2 Surface and Influence on Electrical Transport at a Buried Interface with an Organic Semiconductor Layer, Langmuir, 36 (2020) 5809-5819. https://doi.org/10.1021/acs.langmuir.0c00515.

[28] K. Deng, R.J. Collins, M. Mehregany, C.N. Sukenik, Performance Impact of Monolayer Coating of Polysilicon Micromotors, Journal of The Electrochemical Society, 142 (1995) 1278-1285. https://doi.org/10.1149/1.2044164.

[29] Y. Li, C. Cai, Click Chemistry-Based Functionalization on Non-Oxidized Silicon Substrates, Chemistry – An Asian Journal, 6 (2011) 2592-2605. https://doi.org/10.1002/asia.201100294.

[30] M.R. Linford, C.E.D. Chidsey, Alkyl monolayers covalently bonded to silicon surfaces, Journal of the American Chemical Society, 115 (1993) 12631-12632. https://doi.org/10.1021/ja00079a071.

[31] M.R. Linford, P. Fenter, P.M. Eisenberger, C.E.D. Chidsey, Alkyl Monolayers on Silicon Prepared from 1-Alkenes and Hydrogen-Terminated Silicon, Journal of the American Chemical Society, 117 (1995) 3145-3155. https://doi.org/10.1021/ja00116a019.

[32] P. Wagner, S. Nock, J.A. Spudich, W.D. Volkmuth, S. Chu, R.L. Cicero, C.P. Wade, M.R. Linford, C.E.D. Chidsey, Bioreactive Self-Assembled Monolayers on Hydrogen-Passivated Si(111) as a New Class of Atomically Flat Substrates for Biological Scanning Probe

Microscopy, Journal of Structural Biology, 119 (1997) 189-201. https://doi.org/10.1006/jsbi.1997.3881.

[33] C.J. Barrelet, D.B. Robinson, J. Cheng, T.P. Hunt, C.F. Quate, C.E.D. Chidsey, Surface Characterization and Electrochemical Properties of Alkyl, Fluorinated Alkyl, and Alkoxy Monolayers on Silicon, Langmuir, 17 (2001) 3460-3465. https://doi.org/10.1021/la010333p.

[34] S. Ciampi, T. Böcking, K.A. Kilian, M. James, J.B. Harper, J.J. Gooding, Functionalization of Acetylene-Terminated Monolayers on Si(100) Surfaces: A Click Chemistry Approach, Langmuir, 23 (2007) 9320-9329. https://doi.org/10.1021/la701035g.

[35] J. Terry, M.R. Linford, C. Wigren, R. Cao, P. Pianetta, C.E.D. Chidsey, Determination of the bonding of alkyl monolayers to the Si(111) surface using chemical-shift, scanned-energy photoelectron diffraction, Applied Physics Letters, 71 (1997) 1056-1058. https://doi.org/10.1063/1.119726.

[36] J.M. Buriak, Illuminating Silicon Surface Hydrosilylation: An Unexpected Plurality of Mechanisms, Chemistry of Materials, 26 (2014) 763-772. https://doi.org/10.1021/cm402120f.

[37] P. Thissen, O. Seitz, Y.J. Chabal, Wet chemical surface functionalization of oxide-free silicon, Progress in Surface Science, 87 (2012) 272-290. https://doi.org/10.1016/j.progsurf.2012.10.003.

[38] H.C. Kolb, M.G. Finn, K.B. Sharpless, Click Chemistry: Diverse Chemical Function from a Few Good Reactions, Angewandte Chemie International Edition, 40 (2001) 2004-2021. https://doi.org/10.1002/1521-3773(20010601)40:11<2004::AID-ANIE2004>3.0.CO;2-5.

[39] S. Ciampi, G. Le Saux, J.B. Harper, J.J. Gooding, Optimization of Click Chemistry of Ferrocene Derivatives on Acetylene-Functionalized Silicon(100) Surfaces, Electroanalysis, 20 (2008) 1513-1519. https://doi.org/10.1002/elan.200804241.

[40] R. Takizawa, T. Nakanishi, A. Ohsawa, Degradation of metal-oxide-semiconductor devices caused by iron impurities on the silicon wafer surface, Journal of Applied Physics, 62 (1987) 4933-4935. https://doi.org/10.1063/1.339822.

[41] L. Zhong, F. Shimura, Dependence of lifetime on surface concentration of copper and iron in silicon wafers, Applied Physics Letters, 61 (1992) 1078-1080. https://doi.org/10.1063/1.107696.

[42] T.U. Connell, C. Schieber, I.P. Silvestri, J.M. White, S.J. Williams, P.S. Donnelly, Copper and Silver Complexes of Tris(triazole)amine and Tris(benzimidazole)amine Ligands: Evidence that Catalysis of an Azide–Alkyne Cycloaddition (“Click”) Reaction by a Silver Tris(triazole)amine Complex Arises from Copper Impurities, Inorganic Chemistry, 53 (2014) 6503-6511. https://doi.org/10.1021/ic5008999.

[43] M.H. Choudhury, S. Ciampi, Y. Yang, R. Tavallaie, Y. Zhu, L. Zarei, V.R. Goncales, J.J. Gooding, Connecting electrodes with light: one wire, many electrodes, Chemical Science, 6 (2015) 6769-6776. https://doi.org/10.1039/C5SC03011K.

[44] Y. Zhu, B. Gupta, B. Guan, S. Ciampi, P.J. Reece, J.J. Gooding, Photolithographic Strategy for Patterning Preformed, Chemically Modified, Porous Silicon Photonic Crystal Using Click Chemistry, ACS Applied Materials & Interfaces, 5 (2013) 6514-6521. https://doi.org/10.1021/am4006012.

[45] F. Wu, D.-W. Zhang, J. Wang, M. Watkinson, S. Krause, Copper Contamination of Self-Assembled Organic Monolayer Modified Silicon Surfaces Following a “Click” Reaction Characterized with LAPS and SPIM, Langmuir, 33 (2017) 3170-3177. https://doi.org/10.1021/acs.langmuir.6b03831.

[46] M. James, S. Ciampi, T.A. Darwish, T.L. Hanley, S.O. Sylvester, J.J. Gooding, Nanoscale Water Condensation on Click-Functionalized Self-Assembled Monolayers, Langmuir, 27 (2011) 10753-10762. https://doi.org/10.1021/la202359c.

[47] M. James, T.A. Darwish, S. Ciampi, S.O. Sylvester, Z. Zhang, A. Ng, J.J. Gooding, T.L. Hanley, Nanoscale condensation of water on self-assembled monolayers, Soft Matter, 7 (2011) 5309-5318. https://doi.org/10.1039/C1SM05096F.

[48] S. Deng, R. Xu, W. Seh, J. Sun, W. Cai, J. Zou, Q. Zhang, Current degradation mechanism of tip contact metal-silicon Schottky nanogenerator, Nano Energy, 94 (2022) 106888. https://doi.org/10.1016/j.nanoen.2021.106888.

[49] V.R. Gonçales, Y. Wu, B. Gupta, S.G. Parker, Y. Yang, S. Ciampi, R. Tilley, J.J. Gooding, Stability of Chemically Passivated Silicon Electrodes in Aqueous Solutions: Interplay between Bias Voltage and Hydration of the Electrolyte, The Journal of Physical Chemistry C, 120 (2016) 15941-15948. https://doi.org/10.1021/acs.jpcc.5b12454.

[50] J.Y. Park, M. Salmeron, Fundamental Aspects of Energy Dissipation in Friction, Chemical Reviews, 114 (2014) 677-711. https://doi.org/10.1021/cr200431y.

[51] B.N.J. Persson, A.I. Volokitin, Electronic friction of physisorbed molecules, The Journal of Chemical Physics, 103 (1995) 8679-8683. https://doi.org/10.1063/1.470125.

[52] A. Dayo, W. Alnasrallah, J. Krim, Superconductivity-Dependent Sliding Friction, Physical Review Letters, 80 (1998) 1690-1693. https://doi.org/10.1103/PhysRevLett.80.1690.

[53] M. Highland, J. Krim, Superconductivity Dependent Friction of Water, Nitrogen, and Superheated He Films Adsorbed on Pb(111), Physical Review Letters, 96 (2006) 226107. https://doi.org/10.1103/PhysRevLett.96.226107.

[54] J.Y. Park, D.F. Ogletree, P.A. Thiel, M. Salmeron, Electronic Control of Friction in Silicon pn Junctions, Science, 313 (2006) 186. https://doi.org/10.1126/science.1125017.

[55] J.Y. Park, Y. Qi, D.F. Ogletree, P.A. Thiel, M. Salmeron, Influence of carrier density on the friction properties of silicon pn junctions, Physical Review B, 76 (2007) 064108. https://doi.org/10.1103/PhysRevB.76.064108.

[56] Y. Qi, J.Y. Park, B.L.M. Hendriksen, D.F. Ogletree, M. Salmeron, Electronic contribution to friction on GaAs: An atomic force microscope study, Physical Review B, 77 (2008) 184105. https://doi.org/10.1103/PhysRevB.77.184105.

[57] M. Akbulut, A.R. Godfrey Alig, J. Israelachvili, Triboelectrification between Smooth Metal Surfaces Coated with Self-Assembled Monolayers (SAMs), The Journal of Physical Chemistry B, 110 (2006) 22271-22278. https://doi.org/10.1021/jp063161j.

[58] N.J. Brewer, B.D. Beake, G.J. Leggett, Friction Force Microscopy of Self-Assembled Monolayers: Influence of Adsorbate Alkyl Chain Length, Terminal Group Chemistry, and Scan Velocity, Langmuir, 17 (2001) 1970-1974. https://doi.org/10.1021/la001568o.

[59] L. Zhang, L. Li, S. Chen, S. Jiang, Measurements of Friction and Adhesion for Alkyl Monolayers on Si(111) by Scanning Force Microscopy, Langmuir, 18 (2002) 5448-5456. https://doi.org/10.1021/la011718a.

[60] L. Li, S. Chen, S. Jiang, Nanoscale Frictional Properties of Mixed Alkanethiol Self-Assembled Monolayers on Au(111) by Scanning Force Microscopy: Humidity Effect, Langmuir, 19 (2003) 666-671. https://doi.org/10.1021/la026575m.

[61] F.-R. Fan, Z.-Q. Tian, Z.L. Wang, Flexible triboelectric generator, Nano Energy, 1 (2012) 328-334. https://doi.org/10.1016/j.nanoen.2012.01.004.

[62] J. Zhao, G. Zhen, G. Liu, T. Bu, W. Liu, X. Fu, P. Zhang, C. Zhang, Z.L. Wang, Remarkable merits of triboelectric nanogenerator than electromagnetic generator for harvesting small-amplitude mechanical energy, Nano Energy, 61 (2019) 111-118. https://doi.org/10.1016/j.nanoen.2019.04.047.

[63] D. Liu, X. Yin, H. Guo, L. Zhou, X. Li, C. Zhang, J. Wang, Z.L. Wang, A constant current triboelectric nanogenerator arising from electrostatic breakdown, Science Advances, 5 (2019) eaav6437. https://doi.org/10.1126/sciadv.aav6437.

[64] C. Zhang, T. Zhou, W. Tang, C. Han, L. Zhang, Z.L. Wang, Rotating-Disk-Based Direct-Current Triboelectric Nanogenerator, Advanced Energy Materials, 4 (2014) 1301798. https://doi.org/10.1002/aenm.201301798.

[65] F.-C. Kao, H.-H. Ho, P.-Y. Chiu, M.-K. Hsieh, J.C. Liao, P.-L. Lai, Y.-F. Huang, M.-Y. Dong, T.-T. Tsai, Z.-H. Lin, Self-assisted wound healing using piezoelectric and triboelectric nanogenerators, Science and Technology of Advanced Materials, 23 (2022) 1-16. https://doi.org/10.1080/14686996.2021.2015249.

[66] X. Li, J. Luo, K. Han, X. Shi, Z. Ren, Y. Xi, Y. Ying, J. Ping, Z.L. Wang, Stimulation of ambient energy generated electric field on crop plant growth, Nature Food, (2022). https://doi.org/10.1038/s43016-021-00449-9.

[67] R. Xu, Q. Zhang, J.Y. Wang, D. Liu, J. Wang, Z.L. Wang, Direct current triboelectric cell by sliding an n-type semiconductor on a p-type semiconductor, Nano Energy, 66 (2019) 104185. https://doi.org/10.1016/j.nanoen.2019.104185.

[68] Y. Lu, Z. Hao, S. Feng, R. Shen, Y. Yan, S. Lin, Direct-Current Generator Based on Dynamic PN Junctions with the Designed Voltage Output, iScience, 22 (2019) 58-69. https://doi.org/10.1016/j.isci.2019.11.004.

[69] H. Shao, J. Fang, H. Wang, L. Dai, T. Lin, Polymer–Metal Schottky Contact with Direct-Current Outputs, Advanced Materials, 28 (2016) 1461-1466. https://doi.org/10.1002/adma.201504778.

[70] H. Shao, J. Fang, H. Wang, H. Zhou, H. Niu, F. Chen, G. Yan, S. Fu, Y. Cao, T. Lin, Doping Effect on Conducting Polymer-Metal Schottky DC Generators, Advanced Electronic Materials, 5 (2019) 1800675. https://doi.org/10.1002/aelm.201800675.

[71] J. Liu, A. Goswami, K. Jiang, F. Khan, S. Kim, R. McGee, Z. Li, Z. Hu, J. Lee, T. Thundat, Direct-current triboelectricity generation by a sliding Schottky nanocontact on MoS2 multilayers, Nature Nanotechnology, 13 (2018) 112-116. https://doi.org/10.1038/s41565-017-0019-5.

[72] J. Liu, F. Liu, R. Bao, K. Jiang, F. Khan, Z. Li, H. Peng, J. Chen, A. Alodhayb, T. Thundat, Scaled-up Direct-Current Generation in MoS2 Multilayer-Based Moving Heterojunctions, ACS Applied Materials & Interfaces, 11 (2019) 35404-35409. https://doi.org/10.1021/acsami.9b09851.

[73] J. Liu, M. Miao, K. Jiang, F. Khan, A. Goswami, R. McGee, Z. Li, L. Nguyen, Z. Hu, J. Lee, K. Cadien, T. Thundat, Sustained electron tunneling at unbiased metal-insulator-semiconductor triboelectric contacts, Nano Energy, 48 (2018) 320-326. https://doi.org/10.1016/j.nanoen.2018.03.068.

[74] J. Liu, K. Jiang, L. Nguyen, Z. Li, T. Thundat, Interfacial friction-induced electronic excitation mechanism for tribo-tunneling current generation, Materials Horizons, 6 (2019) 1020-1026. https://doi.org/10.1039/C8MH01259H.

[75] J. Liu, M.I. Cheikh, R. Bao, H. Peng, F. Liu, Z. Li, K. Jiang, J. Chen, T. Thundat, Tribo-Tunneling DC Generator with Carbon Aerogel/Silicon Multi-Nanocontacts, Advanced Electronic Materials, 5 (2019) 1900464. https://doi.org/10.1002/aelm.201900464.

[76] W.-G. Kim, D.-W. Kim, I.-W. Tcho, J.-K. Kim, M.-S. Kim, Y.-K. Choi, Triboelectric Nanogenerator: Structure, Mechanism, and Applications, ACS Nano, 15 (2021) 258-287. https://doi.org/10.1021/acsnano.0c09803.

[77] S. Niu, Y. Liu, S. Wang, L. Lin, Y.S. Zhou, Y. Hu, Z.L. Wang, Theory of Sliding-Mode Triboelectric Nanogenerators, Advanced Materials, 25 (2013) 6184-6193. https://doi.org/10.1002/adma.201302808.

[78] Z.L. Wang, A.C. Wang, On the origin of contact-electrification, Materials Today, 30 (2019) 34-51. https://doi.org/10.1016/j.mattod.2019.05.016.

[79] L. Ren, A. Yu, W. Wang, D. Guo, M. Jia, P. Guo, Y. Zhang, Z.L. Wang, J. Zhai, p-n Junction Based Direct-Current Triboelectric Nanogenerator by Conjunction of Tribovoltaic

Effect and Photovoltaic Effect, Nano Letters, 21 (2021) 10099-10106. https://doi.org/10.1021/acs.nanolett.1c03922.
[80] M. Zheng, S. Lin, L. Xu, L. Zhu, Z.L. Wang, Scanning Probing of the Tribovoltaic Effect at the Sliding Interface of Two Semiconductors, Advanced Materials, 32 (2020) 2000928. https://doi.org/10.1002/adma.202000928.
[81] S. Lin, X. Chen, Z.L. Wang, The tribovoltaic effect and electron transfer at a liquid-semiconductor interface, Nano Energy, 76 (2020) 105070. https://doi.org/10.1016/j.nanoen.2020.105070.
[82] M. Zheng, S. Lin, Z. Tang, Y. Feng, Z.L. Wang, Photovoltaic effect and tribovoltaic effect at liquid-semiconductor interface, Nano Energy, 83 (2021) 105810. https://doi.org/10.1016/j.nanoen.2021.105810.
[83] M. Zheng, S. Lin, L. Zhu, Z. Tang, Z.L. Wang, Effects of Temperature on the Tribovoltaic Effect at Liquid-Solid Interfaces, Advanced Materials Interfaces, 9 (2022) 2101757. https://doi.org/10.1002/admi.202101757.
[84] X. Huang, X. Xiang, J. Nie, D. Peng, F. Yang, Z. Wu, H. Jiang, Z. Xu, Q. Zheng, Microscale Schottky superlubric generator with high direct-current density and ultralong life, Nature Communications, 12 (2021) 2268. https://doi.org/10.1038/s41467-021-22371-1.
[85] S. Ciampi, T. Böcking, K.A. Kilian, M. James, J.B. Harper, J.J. Gooding, Functionalization of Acetylene-Terminated Monolayers on Si(100) Surfaces: A Click Chemistry Approach, Langmuir, 23 (2007) 9320–9329. https://doi.org/10.1021/la701035g.
[86] J.M. Casas-Solvas, A. Vargas-Berenguel, L.F. Capitán-Vallvey, F. Santoyo-González, Convenient Methods for the Synthesis of Ferrocene−Carbohydrate Conjugates, Org. Lett., 6 (2004) 3687-3690. https://doi.org/10.1021/ol048665j.
[87] Y. Yang, S. Ciampi, J.J. Gooding, Coupled Thermodynamic and Kinetic Changes in the Electrochemistry of Ferrocenyl Monolayers Induced by Light, Langmuir, 33 (2017) 2497-2503. https://doi.org/10.1021/acs.langmuir.6b04106.
[88] A.R.J. Nelson, S.W. Prescott, refnx: neutron and X-ray reflectometry analysis in Python, J. Appl. Crystallogr., 52 (2019) 193-200. https://doi.org/10.1107/S1600576718017296.
[89] G. Daniel, Electron Mean Free Path in Elemental Metals, J. Appl. Phys., 119 (2016) 085101. https://doi.org/10.1063/1.4942216.
[90] Z.L. Wang, J. Song, Piezoelectric nanogenerators based on zinc oxide nanowire arrays, Science, 312 (2006) 242–246. https://doi.org/10.1126/science.1124005.
[91] A. Li, Y. Zi, H. Guo, Z.L. Wang, F.M. Fernández, Triboelectric nanogenerators for sensitive nano-coulomb molecular mass spectrometry, Nat. Nanotechnol., 12 (2017) 481–487. https://doi.org/10.1038/nnano.2017.17.
[92] F.-R. Fan, Z.-Q. Tian, Z.L. Wang, Flexible triboelectric generator, Nano Energy, 1 (2012) 328–334. https://doi.org/10.1016/j.nanoen.2012.01.004.
[93] D. Liu, X. Yin, H. Guo, L. Zhou, X. Li, C. Zhang, J. Wang, Z.L. Wang, A constant current triboelectric nanogenerator arising from electrostatic breakdown, Sci. Adv., 5 (2019) eaav6437. https://doi.org/10.1126/sciadv.aav6437.
[94] Z.L. Wang, Triboelectric nanogenerators as new energy technology for self-powered systems and as active mechanical and chemical sensors, ACS Nano, 7 (2013) 9533–9557. https://doi.org/10.1021/nn404614z.
[95] J. Liu, K. Jiang, L. Nguyen, Z. Li, T. Thundat, Interfacial friction-induced electronic excitation mechanism for tribo-tunneling current generation, Mater. Horiz., 6 (2019) 1020–1026. https://doi.org/10.1039/C8MH01259H.
[96] J. Liu, A. Goswami, K. Jiang, F. Khan, S. Kim, R. McGee, Z. Li, Z. Hu, J. Lee, T. Thundat, Direct-current triboelectricity generation by a sliding Schottky nanocontact on MoS_2 multilayers, Nat. Nanotechnol., 13 (2018) 112–116. https://doi.org/10.1038/s41565-017-0019-5.

[97] M. Zheng, S. Lin, L. Xu, L. Zhu, Z.L. Wang, Scanning probing of the tribovoltaic effect at the sliding interface of two semiconductors, Adv. Mater., 32 (2020) 2000928. https://doi.org/10.1002/adma.202000928.

[98] K. Nakayama, H. Hashimoto, Triboemission from various materials in atmosphere, Wear, 147 (1991) 335–343. https://doi.org/10.1016/0043-1648(91)90190-6.

[99] S. Lin, Y. Lu, S. Feng, Z. Hao, Y. Yan, A High Current Density Direct-Current Generator Based on a Moving van der Waals Schottky Diode, Adv. Mater., 31 (2018) 1804398. https://doi.org/10.1002/adma.201804398.

[100] J. Liu, M. Miao, K. Jiang, F. Khan, A. Goswami, R. McGee, Z. Li, L. Nguyen, Z. Hu, J. Lee, K. Cadien, T. Thundat, Sustained electron tunneling at unbiased metal-insulator-semiconductor triboelectric contacts, Nano Energy, 48 (2018) 320–326. https://doi.org/10.1016/j.nanoen.2018.03.068.

[101] S. Lin, R. Shen, T. Yao, Y. Lu, S. Feng, Z. Hao, H. Zheng, Y. Yan, E. Li, Surface states enhanced dynamic Schottky diode generator with extremely high power density over 1000 W m−2, Adv. Science, 6 (2019) 1901925. https://doi.org/10.1002/advs.201901925.

[102] Z. Zhang, D. Jiang, J. Zhao, G. Liu, T. Bu, C. Zhang, Z.L. Wang, Tribovoltaic effect on metal–semiconductor interface for direct-current low-impedance triboelectric nanogenerators, Adv. Energy Mater., 10 (2020) 1903713. https://doi.org/10.1002/aenm.201903713.

[103] Z. Hao, T. Jiang, Y. Lu, S. Feng, R. Shen, T. Yao, Y. Yan, Y. Yang, Y. Lu, S. Lin, Co-harvesting Light and Mechanical Energy Based on Dynamic Metal/Perovskite Schottky Junction, Matter, 1 (2019) 639-649. https://doi.org/10.1016/j.matt.2019.05.003.

[104] C.-S. Tan, P.-L. Hsieh, L.-J. Chen, M.H. Huang, Silicon wafers with facet-dependent electrical conductivity properties, Angew. Chem., Int. Ed., 56 (2017) 15339–15343. https://doi.org/10.1002/anie.201709020.

[105] Y.B. Vogel, J. Zhang, N. Darwish, S. Ciampi, Switching of Current Rectification Ratios within a Single Nanocrystal by Facet-Resolved Electrical Wiring, ACS Nano, 12 (2018) 8071-8080. https://doi.org/10.1021/acsnano.8b02934.

[106] Y.B. Vogel, L. Zhang, N. Darwish, V.R. Gonçales, A. Le Brun, J.J. Gooding, A. Molina, G.G. Wallace, M.L. Coote, J. Gonzalez, S. Ciampi, Reproducible flaws unveil electrostatic aspects of semiconductor electrochemistry, Nat. Commun., 8 (2017) 2066. https://doi.org/10.1038/s41467-017-02091-1.

[107] J.T. Dickinson, E.E. Donaldson, M.K. Park, The emission of electrons and positive ions from fracture of materials, J. Mater. Sci., 16 (1981) 2897–2908. https://doi.org/10.1007/BF00552976.

[108] A. Böttcher, R. Grobecker, R. Imbeck, A. Morgante, G. Ertl, Exoelectron emission during oxidation of Cs films, J. Chem. Phys., 95 (1991) 3756–3766. https://doi.org/10.1063/1.460826.

[109] S.A.A. Ahmad, S. Ciampi, S.G. Parker, V.R. Gonçales, J.J. Gooding, Forming Ferrocenyl Self-Assembled Monolayers on Si(100) Electrodes with Different Alkyl Chain Lengths for Electron Transfer Studies, ChemElectroChem, 6 (2019) 211-220. https://doi.org/10.1002/celc.201800717.

[110] S. Minomura, H.G. Drickamer, Pressure induced phase transitions in silicon, germanium and some III–V compounds, J. Phys. Chem. Solids, 23 (1962) 451–456. https://doi.org/10.1016/0022-3697(62)90085-9.

[111] B. Sujak, A. Gieroszbski, K. Gieroszinska, Energy distribution of exoelectrons emitted into vacuum from plastically deformed, oxide covered aluminum at low temperatures, Acta Phys. Pol., A46 (1974) 3–17.

[112] K. Nakayama, N. Suzuki, H. Hashimoto, Triboemission of charged particles and photons from solid surfaces during frictional damage, J. Phys. D: Appl. Phys., 25 (1992) 303–308. https://doi.org/10.1088/0022-3727/25/2/027.

[113] P. Lazić, B.N.J. Persson, Surface-roughness–induced electric-field enhancement and triboluminescence, EPL, 91 (2010) 46003–46007. https://doi.org/10.1209/0295-5075/91/46003.
[114] R. Budakian, S.J. Putterman, Correlation between charge transfer and stick-slip friction at a metal-insulator interface, Phys. Rev. Lett., 85 (2000) 1000–1003. https://doi.org/10.1103/PhysRevLett.85.1000.
[115] Y. Qi, J.Y. Park, B.L.M. Hendriksen, D.F. Ogletree, M. Salmeron, Electronic contribution to friction on GaAs: An atomic force microscope study, Phys. Rev. B, 77 (2008) 184105. https://doi.org/10.1103/PhysRevB.77.184105.
[116] B.N.J. Persson, A.I. Volokitin, Electronic friction of physisorbed molecules, J. Chem. Phys., 103 (1995) 8679-8683. https://doi.org/10.1063/1.470125.
[117] G. Witte, K. Weiss, P. Jakob, J. Braun, K.L. Kostov, C. Wöll, Damping of molecular motion on a solid substrate: evidence for electron-hole pair creation, Phys. Rev. Lett., 80 (1998) 121-124. https://doi.org/10.1103/PhysRevLett.80.121.
[118] M. James, S. Ciampi, T.A. Darwish, T.L. Hanley, S.O. Sylvester, J.J. Gooding, Nanoscale water condensation on click-functionalized self-assembled monolayers, Langmuir, 27 (2011) 10753–10762. https://doi.org/10.1021/la202359c.
[119] A. Dayo, W. Alnasrallah, J. Krim, Superconductivity-dependent sliding friction, Phys. Rev. Lett., 80 (1998) 1690-1693. https://doi.org/10.1103/PhysRevLett.80.1690.
[120] M.V. Fischetti, S.E. Laux, Band structure, deformation potentials, and carrier mobility in strained Si, Ge, and SiGe alloys, J. Appl. Phys., 80 (1996) 2234–2252. https://doi.org/10.1063/1.363052.
[121] M.H. Liao, P.S. Kuo, S.R. Jan, S.T. Chang, C.W. Liu, Strained Pt Schottky diodes on n-type Si and Ge, Appl. Phys. Lett., 88 (2006) 143509. https://doi.org/10.1063/1.2191831.
[122] X.G. Zhang, Mechanism of pore formation on n-type silicon, J. Electrochem. Soc., 138 (1991) 3750–3756. https://doi.org/10.1149/1.2085494.
[123] X.G. Zhang, S.D. Collins, R.L. Smith, Porous silicon formation and electropolishing of silicon by anodic polarization in HF solution, J. Electrochem. Soc., 136 (1989) 1561-1565. https://doi.org/10.1149/1.2096961.
[124] J.R. Rumble, D.R. Lide, T.J. Bruno, CRC handbook of chemistry and physics : a ready-reference book of chemical and physical data, 98th edition. / editor-in-chief John R. Rumble

associate editors, David R. Lide, Thomas J. Bruno.. ed.: Boca Raton : CRC Press; 2017.
[125] Hole mobility, diffusion and lifetime in c-Si in: R. Hull (Ed.) Properties of Crystalline Silicon, Institution of Engineering and Technology, London, United Kingdom, 1999.
[126] M.H. Huang, M. Madasu, Facet-dependent and interfacial plane-related photocatalytic behaviors of semiconductor nanocrystals and heterostructures, Nano Today, 28 (2019) 100768. https://doi.org/10.1016/j.nantod.2019.100768.
[127] Y. Song, N. Wang, Y. Wang, R. Zhang, H. Olin, Y. Yang, Direct Current Triboelectric Nanogenerators, Adv. Energy Mater., 10 (2020) 2002756. https://doi.org/10.1002/aenm.202002756.
[128] B. Seo, Y. Cha, S. Kim, W. Choi, Tunable current duration in triboelectric generators via capacitive air gaps, International Journal of Energy Research, n/a. https://doi.org/10.1002/er.6188.
[129] H. Zhang, P. Zhang, W. Zhang, A high-output performance mortise and tenon structure triboelectric nanogenerator for human motion sensing, Nano Energy, 84 (2021) 105933. https://doi.org/10.1016/j.nanoen.2021.105933.
[130] Z. Zhang, D. Jiang, J. Zhao, G. Liu, T. Bu, C. Zhang, Z.L. Wang, Tribovoltaic Effect on Metal–Semiconductor Interface for Direct-Current Low-Impedance Triboelectric

Nanogenerators, Advanced Energy Materials, 10 (2020) 1903713. https://doi.org/10.1002/aenm.201903713.

[131] C. Shan, W. Liu, Z. Wang, X. Pu, W. He, Q. Tang, S. Fu, G. Li, L. Long, H. Guo, J. Sun, A. Liu, C. Hu, An inverting TENG to realize the AC mode based on the coupling of triboelectrification and air-breakdown, Energy & Environmental Science, 14 (2021) 5395-5405. https://doi.org/10.1039/D1EE01641E.

[132] S. Fu, W. He, Q. Tang, Z. Wang, W. Liu, Q. Li, C. Shan, L. Long, C. Hu, H. Liu, An Ultrarobust and High-Performance Rotational Hydrodynamic Triboelectric Nanogenerator Enabled by Automatic Mode Switching and Charge Excitation, Advanced Materials, n/a (2021) 2105882. https://doi.org/10.1002/adma.202105882.

[133] W. He, W. Liu, J. Chen, Z. Wang, Y. Liu, X. Pu, H. Yang, Q. Tang, H. Yang, H. Guo, C. Hu, Boosting output performance of sliding mode triboelectric nanogenerator by charge space-accumulation effect, Nature Communications, 11 (2020) 4277. https://doi.org/10.1038/s41467-020-18086-4.

[134] A.C. Aragonès, N. Darwish, S. Ciampi, F. Sanz, J.J. Gooding, I. Díez-Pérez, Single-molecule electrical contacts on silicon electrodes under ambient conditions, Nat. Commun., 8 (2017) 15056. https://doi.org/10.1038/ncomms15056.

[135] R. Cohen, L. Kronik, A. Shanzer, D. Cahen, A. Liu, Y. Rosenwaks, J.K. Lorenz, A.B. Ellis, Molecular Control over Semiconductor Surface Electronic Properties: Dicarboxylic Acids on CdTe, CdSe, GaAs, and InP, J. Am. Chem. Soc., 121 (1999) 10545-10553. https://doi.org/10.1021/ja9906150.

[136] G. Ashkenasy, D. Cahen, R. Cohen, A. Shanzer, A. Vilan, Molecular Engineering of Semiconductor Surfaces and Devices, Acc. Chem. Res., 35 (2002) 121-128. https://doi.org/10.1021/ar990047t.

[137] S. Ciampi, J.B. Harper, J.J. Gooding, Wet Chemical Routes to the Assembly of Organic Monolayers on Silicon Surfaces via the Formation of Si−C Bonds: Surface Preparation, Passivation and Functionalization, Chem. Soc. Rev., 39 (2010) 2158-2183. https://doi.org/10.1039/B923890P.

[138] J.J. Gooding, S. Ciampi, The Molecular Level Modification of Surfaces: From Self-Assembled Monolayers to Complex Molecular Assemblies, Chem. Soc. Rev., 40 (2011) 2704-2718. https://doi.org/10.1039/C0CS00139B.

[139] J.Y. Park, Y. Qi, D.F. Ogletree, P.A. Thiel, M. Salmeron, Influence of carrier density on the friction properties of silicon pn junctions, Phys. Rev. B, 76 (2007) 064108. https://doi.org/10.1103/PhysRevB.76.064108.

[140] J. Liu, K. Jiang, L. Nguyen, Z. Li, T. Thundat, Interfacial friction-induced electronic excitation mechanism for tribo-tunneling current generation, Mater. Horiz., 6 (2019) 1020-1026. https://doi.org/10.1039/C8MH01259H.

[141] Z. Zhang, T. He, J. Zhao, G. Liu, Z.L. Wang, C. Zhang, Tribo-thermoelectric and tribovoltaic coupling effect at metal-semiconductor interface, Mater. Today Phys., 16 (2021) 100295. https://doi.org/10.1016/j.mtphys.2020.100295.

[142] H. Mishina, Friction and wear of semiconductors in sliding contact with pure metals, Tribol. Int., 21 (1988) 76-82. https://doi.org/10.1016/0301-679X(88)90078-3.

[143] A. Mukherjee, A.D. Craciun, J.L. Gallani, M.V. Rastei, Nanoscale adhesion and sliding on biased semiconductors, Faraday Discuss., 199 (2017) 323-334. https://doi.org/10.1039/C6FD00254D.

[144] J. Zhang, S. Ferrie, S. Zhang, Y.B. Vogel, C.R. Peiris, N. Darwish, S. Ciampi, Single-Electrode Electrochemistry: Chemically Engineering Surface Adhesion and Hardness To Maximize Redox Work Extracted from Tribocharged Silicon, ACS Appl. Nano Mater., 2 (2019) 7230-7236. https://doi.org/10.1021/acsanm.9b01726.

[145] Y.B. Vogel, N. Darwish, S. Ciampi, Spatiotemporal Control of Electrochemiluminescence Guided by a Visible Light Stimulus, Cell Rep. Phys. Sci., 3 (2020) 615-616. https://doi.org/10.1016/j.xcrp.2020.100107.

[146] M.K. Chaudhury, Adhesion and friction of self-assembled organic monolayers, Curr. Opin. Colloid Interface Sci., 2 (1997) 65-69. https://doi.org/10.1016/S1359-0294(97)80009-X.

[147] J.Y. Park, Y. Qi, P.D. Ashby, B.L.M. Hendriksen, M. Salmeron, Electrical transport and mechanical properties of alkylsilane self-assembled monolayers on silicon surfaces probed by atomic force microscopy, J. Chem. Phys., 130 (2009) 114705. https://doi.org/10.1063/1.3089789.

[148] K. Deng, R.J. Collins, M. Mehregany, C.N. Sukenik, Performance Impact of Monolayer Coating of Polysilicon Micromotors, J. Electrochem. Soc., 142 (1995) 1278-1285. https://doi.org/10.1149/1.2044164.

[149] M. Akbulut, A.R. Godfrey Alig, J. Israelachvili, Triboelectrification between Smooth Metal Surfaces Coated with Self-Assembled Monolayers (SAMs), J. Phys. Chem. B, 110 (2006) 22271-22278. https://doi.org/10.1021/jp063161j.

[150] S. Ferrie, N. Darwish, J.J. Gooding, S. Ciampi, Harnessing silicon facet-dependent conductivity to enhance the direct-current produced by a sliding Schottky diode triboelectric nanogenerator, Nano Energy, 78 (2020) 105210. https://doi.org/10.1016/j.nanoen.2020.105210.

[151] S. Ciampi, P.K. Eggers, G. Le Saux, M. James, J.B. Harper, J.J. Gooding, Silicon (100) Electrodes Resistant to Oxidation in Aqueous Solutions: An Unexpected Benefit of Surface Acetylene Moieties, Langmuir, 25 (2009) 2530-2539. https://doi.org/10.1021/la803710d.

[152] B. Fabre, Functionalization of Oxide-Free Silicon Surfaces with Redox-Active Assemblies, Chem. Rev., 116 (2016) 4808-4849. https://doi.org/10.1021/acs.chemrev.5b00595.

[153] S. Zhang, S. Ferrie, C.R. Peiris, X. Lyu, Y.B. Vogel, N. Darwish, S. Ciampi, Common Background Signals in Voltammograms of Crystalline Silicon Electrodes are Reversible Silica–Silicon Redox Chemistry at Highly Conductive Surface Sites, J. Am. Chem. Soc., 143 (2021) 1267-1272. https://doi.org/10.1021/jacs.0c10713.

[154] F. Himo, T. Lovell, R. Hilgraf, V.V. Rostovtsev, L. Noodleman, K.B. Sharpless, V.V. Fokin, Copper(I)-Catalyzed Synthesis of Azoles. DFT Study Predicts Unprecedented Reactivity and Intermediates, Journal of the American Chemical Society, 127 (2005) 210-216. https://doi.org/10.1021/ja0471525.

[155] B.T. Worrell, J.A. Malik, V.V. Fokin, Direct Evidence of a Dinuclear Copper Intermediate in Cu(I)-Catalyzed Azide-Alkyne Cycloadditions, Science, 340 (2013) 457-460. https://doi.org/10.1126/science.1229506.

[156] J. Zhao, K. Uosaki, Electron Transfer through Organic Monolayers Directly Bonded to Silicon Probed by Current Sensing Atomic Force Microscopy: Effect of Chain Length and Applied Force, J. Phys. Chem. B, 108 (2004) 17129-17135. https://doi.org/10.1021/jp049719+.

[157] A.B. Sieval, R. Opitz, H.P.A. Maas, M.G. Schoeman, G. Meijer, F.J. Vergeldt, H. Zuilhof, E.J.R. Sudhölter, Monolayers of 1-alkynes on the H-terminated Si(100) surface, Langmuir, 16 (2000) 10359-10368. https://doi.org/10.1021/la001109n.

[158] J. Grobelny, N. Pradeep, D.I. Kim, Z.C. Ying, Quantification of the meniscus effect in adhesion force measurements, Appl. Phys. Lett., 88 (2006) 091906. https://doi.org/10.1063/1.2181200.

[159] T.H. Rhee, M.W. Shin, H. Jang, Effects of humidity and substrate hydrophilicity on nanoscale friction, Tribol. Int., 94 (2016) 234-239. https://doi.org/10.1016/j.triboint.2015.08.042.

[160] J. Zhang, M.L. Coote, S. Ciampi, Electrostatics and Electrochemistry: Mechanism and Scope of Charge-Transfer Reactions on the Surface of Tribocharged Insulators, J. Am. Chem. Soc., 143 (2021) 3019-3032. https://doi.org/10.1021/jacs.0c11006.

[161] P. Allongue, C. Henry de Villeneuve, J. Pinson, Structural characterization of organic monolayers on Si〈111〉 from capacitance measurements, Electrochim. Acta, 45 (2000) 3241-3248. https://doi.org/10.1016/S0013-4686(00)00428-X.

[162] C.E.D. Chidsey, C.R. Bertozzi, T.M. Putvinski, A.M. Mujsce, Coadsorption of ferrocene-terminated and unsubstituted alkanethiols on gold: electroactive self-assembled monolayers, J. Am. Chem. Soc., 112 (1990) 4301-4306. https://doi.org/10.1021/ja00167a028.

[163] S. Ciampi, M.H. Choudhury, S.A.B.A. Ahmad, N. Darwish, A.L. Brun, J.J. Gooding, The Impact of Surface Coverage on the Kinetics of Electron Transfer through Redox Monolayers on a Silicon Electrode Surface, Electrochim. Acta, 186 (2015) 216-222. https://doi.org/10.1016/j.electacta.2015.10.125.

[164] O. Yaffe, L. Scheres, L. Segev, A. Biller, I. Ron, E. Salomon, M. Giesbers, A. Kahn, L. Kronik, H. Zuilhof, A. Vilan, D. Cahen, Hg/Molecular Monolayer−Si Junctions: Electrical Interplay between Monolayer Properties and Semiconductor Doping Density, J. Phys. Chem. C, 114 (2010) 10270-10279. https://doi.org/10.1021/jp101656t.

[165] X. Wallart, C.H. de Villeneuve, P. Allongue, Truly Quantitative XPS Characterization of Organic Monolayers on Silicon: Study of Alkyl and Alkoxy Monolayers on H-Si(111), J. Am. Chem. Soc. , 127 (2005) 7871-7878. https://doi.org/10.1021/ja0430797.

[166] L. Scheres, A. Arafat, H. Zuilhof, Self-Assembly of High-Quality Covalently Bound Organic Monolayers onto Silicon, Langmuir, 23 (2007) 8343-8346. https://doi.org/10.1021/la701359k.

[167] E. Ito, H. Oji, T. Araki, K. Oichi, H. Ishii, Y. Ouchi, T. Ohta, N. Kosugi, Y. Maruyama, T. Naito, T. Inabe, K. Seki, Soft X-ray Absorption and X-ray Photoelectron Spectroscopic Study of Tautomerism in Intramolecular Hydrogen Bonds of N-Salicylideneaniline Derivatives, J. Am. Chem. Soc., 119 (1997) 6336-6344. https://doi.org/10.1021/ja9641362.

[168] A. Devadoss, C.E.D. Chidsey, Azide-Modified Graphitic Surfaces for Covalent Attachment of Alkyne-Terminated Molecules by "Click" Chemistry, J. Am. Chem. Soc., 129 (2007) 5370-5371. https://doi.org/10.1021/ja071291f.

[169] M.H. Choudhury, S. Ciampi, Y. Yang, R. Tavallaie, Y. Zhu, L. Zarei, V.R. Goncales, J.J. Gooding, Connecting electrodes with light: one wire, many electrodes, Chem. Sci., 6 (2015) 6769-6776. https://doi.org/10.1039/C5SC03011K.

[170] J.Y. Park, M. Salmeron, Fundamental Aspects of Energy Dissipation in Friction, Chem. Rev., 114 (2014) 677-711. https://doi.org/10.1021/cr200431y.

[171] H. Ledbetter, S. Kim, Monocrystal elastic constants and derived properties of the cubic and the hexagonal elements, in: M. Levy, H.E. Bass, R.R. Stern, L. Furr, V. Keppens (Eds.), Handbook of elastic properties of solids, liquids and gases, Academic Press, San Diego, 2001, pp. 97-106.

[172] H.J. Lee, A.C. Jamison, T.R. Lee, Surface Dipoles: A Growing Body of Evidence Supports Their Impact and Importance, Acc. Chem. Res., 48 (2015) 3007-3015. https://doi.org/10.1021/acs.accounts.5b00307.

[173] A. Gankin, R. Sfez, E. Mervinetsky, J. Buchwald, A. Dianat, L. Medrano Sandonas, R. Gutierrez, G. Cuniberti, S. Yitzchaik, Molecular and Ionic Dipole Effects on the Electronic Properties of Si-/SiO_2-Grafted Alkylamine Monolayers, ACS Appl. Mater. Interfaces, 9 (2017) 44873-44879. https://doi.org/10.1021/acsami.7b12218.

[174] L. Zhang, Y.B. Vogel, B.B. Noble, V.R. Gonçales, N. Darwish, A.L. Brun, J.J. Gooding, G.G. Wallace, M.L. Coote, S. Ciampi, TEMPO Monolayers on Si(100) Electrodes: Electrostatic Effects by the Electrolyte and Semiconductor Space-Charge on the Electroactivity

of a Persistent Radical, Journal of the American Chemical Society, 138 (2016) 9611-9619. https://doi.org/10.1021/jacs.6b04788.

[175] G. Zoth, W. Bergholz, A fast, preparation-free method to detect iron in silicon, Journal of Applied Physics, 67 (1990) 6764-6771. https://doi.org/10.1063/1.345063.

[176] R.R. Kola, G.A. Rozgonyi, J. Li, W.B. Rogers, T.Y. Tan, K.E. Bean, K. Lindberg, Transition metal silicide precipitation in silicon induced by rapid thermal processing and free-surface gettering, Applied Physics Letters, 55 (1989) 2108-2110. https://doi.org/10.1063/1.102342.

[177] L. Mouche, F. Tardif, J. Derrien, Mechanisms of Metallic Impurity Deposition on Silicon Substrates Dipped in Cleaning Solution, Journal of The Electrochemical Society, 142 (1995) 2395-2401. https://doi.org/10.1149/1.2044308.

[178] G. Evano, K. Jouvin, C. Theunissen, C. Guissart, A. Laouiti, C. Tresse, J. Heimburger, Y. Bouhoute, R. Veillard, M. Lecomte, A. Nitelet, S. Schweizer, N. Blanchard, C. Alayrac, A.C. Gaumont, Turning unreactive copper acetylides into remarkably powerful and mild alkyne transfer reagents by oxidative umpolung, Chemical Communications, 50 (2014) 10008-10018. https://doi.org/10.1039/C4CC03198A.

[179] P.W. Schindler, B. Fürst, R. Dick, P.U. Wolf, Ligand properties of surface silanol groups. I. surface complex formation with Fe3+, Cu2+, Cd2+, and Pb2+, Journal of Colloid and Interface Science, 55 (1976) 469-475. https://doi.org/10.1016/0021-9797(76)90057-6.

[180] J.S. Jeon, S. Raghavan, H.G. Parks, J.K. Lowell, I. Ali, Electrochemical Investigation of Copper Contamination on Silicon Wafers from HF Solutions, Journal of The Electrochemical Society, 143 (1996) 2870-2875. https://doi.org/10.1149/1.1837120.

[181] V. Bertagna, F. Rouelle, G. Revel, M. Chemla, Electrochemical and Radiochemical Study of Copper Contamination Mechanism from HF Solutions onto Silicon Substrates, Journal of The Electrochemical Society, 144 (1997) 4175-4182. https://doi.org/10.1149/1.1838162.

[182] V. Bertagna, F. Rouelle, M. Chemla, Influence of O2 and H2O2 on the metallic contamination process of silicon wafers in dilute HF solutions, Semiconductor Science and Technology, 13 (1998) 444-452. https://doi.org/10.1088/0268-1242/13/4/016.

[183] Y.B. Vogel, A. Molina, J. Gonzalez, S. Ciampi, Quantitative Analysis of Cyclic Voltammetry of Redox Monolayers Adsorbed on Semiconductors: Isolating Electrode Kinetics, Lateral Interactions, and Diode Currents, Analytical Chemistry, 91 (2019) 5929-5937. https://doi.org/10.1021/acs.analchem.9b00336.

[184] E. Laviron, General expression of the linear potential sweep voltammogram in the case of diffusionless electrochemical systems, Journal of Electroanalytical Chemistry and Interfacial Electrochemistry, 101 (1979) 19-28. https://doi.org/10.1016/S0022-0728(79)80075-3.

[185] D.A. Brevnov, H.O. Finklea, H. Van Ryswyk, Ac voltammetry studies of electron transfer kinetics for a redox couple attached via short alkanethiols to a gold electrode, Journal of Electroanalytical Chemistry, 500 (2001) 100-107. https://doi.org/10.1016/S0022-0728(00)00316-8.

[186] E. Laviron, A.C. polarography and faradaic impedance of strongly adsorbed electroactive species: Part I. Theoretical and experimental study of a quasi-reversible reaction in the case of a Langmuir isotherm, Journal of Electroanalytical Chemistry and Interfacial Electrochemistry, 97 (1979) 135-149. https://doi.org/10.1016/S0022-0728(79)80057-1.

[187] E. Laviron, A.C. Polarography and faradaic impedance of strongly adsorbed electroactive species: Part III. Theoretical complex plane analysis for a surface redox reaction, Journal of Electroanalytical Chemistry and Interfacial Electrochemistry, 105 (1979) 35-42. https://doi.org/10.1016/S0022-0728(79)80337-X.

[188] E. Mahé, F. Rouelle, I. Darolles, D. Devilliers, Electrochemical characterization of silicon electrodes: Part 1: Capacitance-Voltage Method, J. New Mat. Electrochem. Sys., 9 (2006) 257.
[189] H.F. Okorn-Schmidt, Characterization of silicon surface preparation processes for advanced gate dielectrics, IBM Journal of Research and Development, 43 (1999) 351-326. https://doi.org/10.1147/rd.433.0351.

Every reasonable effort has been made to acknowledge the owners of copyright material. I would be pleased to hear from any copyright owner who has been omitted or incorrectly acknowledged.

Appendix A. Attribution statement for "Harnessing silicon facet-dependent conductivity to enhance the direct-current produced by a sliding Schottky diode triboelectric nanogenerator"

I, Stuart Paul Ferrie, as the primary author of "Harnessing silicon facet-dependent conductivity to enhance the direct-current produced by a sliding Schottky diode triboelectric nanogenerator" conducted all experimental work and data analysis, preparation of figures, writing and editing the manuscript.

Contribution of co-authors is as follows:

Nadim Darwish contributed by supervision and manuscript editing. J. Justin Gooding contributed by manuscript editing. Simone Ciampi contributed by supervision and manuscript editing.

Signed

Nadim Darwish

J. Justin Gooding

Simone Ciampi

Appendix B. Attribution statement for “Sliding Silicon-based Schottky diodes: Maximizing Triboelectricity with Surface Chemistry”

I, Stuart Paul Ferrie, as the primary author of “Sliding silicon based Schottky diodes: Maximizing triboelectricity with surface chemistry”, conducted all experimental work and data analysis, except where noted below; preparation of figures; writing and editing the manuscript.

Contribution of co-authors is as follows:

Anton P. Le Brun performed X-ray reflectometry and associated data analysis. Gowri Krishnan performed X-ray photoelectron spectroscopy for Cu, ultraviolet photoelectron spectroscopy and associated data analysis. Gunther G. Andersson contributed by supervision and manuscript editing. Nadim Darwish contributed by supervision and manuscript editing. Simone Ciampi contributed by supervision and manuscript editing.

Signed

Anton P. Le Brun

Gowri Krishnan (on maternity leave in June 2022)

Gunther G. Andersson

Nadim Darwish

Simone Ciampi

Appendix C: Copyright Permissions

Figure 1.1

Content from this work may be used under the terms of the Creative Commons Attribution 3.0 licence. Any further distribution of this work must maintain attribution to the author(s) and the title of the work, journal citation and DOI.

Figure 1.2

License Details

This Agreement between Mr. Stuart Ferrie ("You") and John Wiley and Sons ("John Wiley and Sons") consists of your license detai
conditions provided by John Wiley and Sons and Copyright Clearance Center.

License Number	5305200921054
License date	May 10, 2022
Licensed Content Publisher	John Wiley and Sons
Licensed Content Publication	Angewandte Chemie International Edition
Licensed Content Title	Silicon Wafers with Facet-Dependent Electrical Conductivity Properties
Licensed Content Author	Michael H. Huang, Lih-Juann Chen, Pei-Lun Hsieh, et al
Licensed Content Date	Nov 2, 2017
Licensed Content Volume	56
Licensed Content Issue	48
Licensed Content Pages	5
Type of Use	Dissertation/Thesis
Requestor type	University/Academic
Format	Print and electronic
Portion	Figure/table
Number of figures/tables	1
Will you be translating?	No
Title	Harnessing Direct Current Triboelectricity with Dynamic Schottky Diodes on Silicon
Institution name	Curtin University
Expected presentation date	Jul 2022
Portions	Figure 3
Requestor Location	Mr. Stuart Ferrie U 44 53 LEONARD ST VICTORIA PARK, WA 6100

	Australia Attn: Stuart Ferrie
Publisher Tax ID	EU826007151
Total	**0.00 USD**

Figure 1.3

License Details

This Agreement between Mr. Stuart Ferrie ("You") and Elsevier ("Elsevier") consists of your license details and the terms and condi
Elsevier and Copyright Clearance Center.

License Number	5305200657751
License date	May 10, 2022
Licensed Content Publisher	Elsevier
Licensed Content Publication	Nano Energy
Licensed Content Title	Mechanical Manipulation of Silicon-based Schottky Diodes via Flexoelectricity
Licensed Content Author	Liang Sun,Lifeng Zhu,Chunli Zhang,Weiqiu Chen,Zhonglin Wang
Licensed Content Date	May 1, 2021
Licensed Content Volume	83
Licensed Content Issue	n/a
Licensed Content Pages	1
Type of Use	reuse in a thesis/dissertation
Portion	figures/tables/illustrations
Number of figures/tables/illustrations	1
Format	both print and electronic
Are you the author of this Elsevier article?	No
Will you be translating?	No
Title	Harnessing Direct Current Triboelectricity with Dynamic Schottky Diodes on Silicon
Institution name	Curtin University
Expected presentation date	Jul 2022
Portions	Figure 3
Requestor Location	Mr. Stuart Ferrie U 44 53 LEONARD ST VICTORIA PARK, WA 6100 Australia Attn: Stuart Ferrie
Publisher Tax ID	GB 494 6272 12

Total	**0.00 USD**

Figure 1.4

License Details

This Agreement between Mr. Stuart Ferrie ("You") and Elsevier ("Elsevier") consists of your license details and the terms and condi
Elsevier and Copyright Clearance Center.

License Number	5305210705997
License date	May 10, 2022
Licensed Content Publisher	Elsevier
Licensed Content Publication	Surface Science
Licensed Content Title	Wet chemical etching of Si(100) surfaces in concentrated NH4F solution: formation of (2 × 1)H reconstructed Si(100) terraces versus (111) facetting
Licensed Content Author	U. Neuwald,H.E. Hessel,A. Feltz,U. Memmert,R.J. Behm
Licensed Content Date	Oct 10, 1993
Licensed Content Volume	296
Licensed Content Issue	1
Licensed Content Pages	7
Type of Use	reuse in a thesis/dissertation
Portion	figures/tables/illustrations
Number of figures/tables/illustrations	1
Format	both print and electronic
Are you the author of this Elsevier article?	No
Will you be translating?	No
Title	Harnessing Direct Current Triboelectricity with Dynamic Schottky Diodes on Silicon
Institution name	Curtin University
Expected presentation date	Jul 2022
Portions	figure 1
Requestor Location	Mr. Stuart Ferrie U 44 53 LEONARD ST VICTORIA PARK, WA 6100 Australia Attn: Stuart Ferrie
Publisher Tax ID	GB 494 6272 12
Total	**0.00 USD**

Figure 1.7

Can I use AAAS material in a thesis or dissertation?

Yes, different criteria apply depending upon whether you are the author of the AAAS article being reproduced.

Others:

AAAS permits the use of content published in its journals *Science*, *Science Immunology*, *Science Robotics*, *Science Signaling*, and *Science Translational Medicine* to be used in a thesis or dissertation, but only provided the following criteria are met:

1. If you are using figure(s)/table(s), permission is granted for use in print and electronic versions of your dissertation or thesis.
2. A full-text article may be used only in print versions of a dissertation or thesis. AAAS does not permit the reproduction of full-text articles in electronic versions of theses or dissertations.
3. The following credit line must be printed along with the AAAS material: “From [Full Reference Citation]. Reprinted with permission from AAAS.”
4. All required credit lines and notices must be visible any time a user accesses any part of the AAAS material and must appear on any printed copies that an authorized user might make.
5. The AAAS material may not be modified or altered, with the exception that figures and tables may be modified with permission from the author. Author permission for any such changes must be secured prior to your use.
6. AAAS must publish the full paper prior to your use of any of its text or figures.
7. If the AAAS material covered by this permission was published in *Science* during the years 1974–1994, you must also obtain permission from the author, who may grant or withhold permission, and who may or may not charge a fee if permission is granted. See original article for author’s address. This condition does not apply to news articles.
8. If you are an original author of the AAAS article being reproduced, please refer to your License to Publish for rules on reproducing your paper in a dissertation or thesis.
9. Permission covers the distribution of your dissertation or thesis on demand by a third-party distributor (e.g., ProQuest/UMI), provided the AAAS material covered by this permission remains in situ and is not distributed by that third party outside of the context of your thesis/dissertation.
10. Permission does not apply to figures/photos/artwork or any other content or materials included in your work that are credited to non-AAAS sources. If the requested material is sourced to or references non-AAAS sources, you must obtain authorization from that source

as well before using that material. You agree to hold harmless and indemnify AAAS against any claims arising from your use of any content in your work that is credited to non-AAAS sources.

11. By using the AAAS material identified in your request, you agree to abide by all the terms and conditions herein.
12. AAAS makes no representations or warranties as to the accuracy of any information contained in the AAAS material covered by this permission, including any warranties of merchantability or fitness for a particular purpose.

Figure 1.8

License Details

This Agreement between Mr. Stuart Ferrie ("You") and Elsevier ("Elsevier") consists of your license details and the terms and condi
Elsevier and Copyright Clearance Center.

License Number	5341820446001
License date	Jul 04, 2022
Licensed Content Publisher	Elsevier
Licensed Content Publication	Nano Energy
Licensed Content Title	Flexible triboelectric generator
Licensed Content Author	Feng-Ru Fan,Zhong-Qun Tian,Zhong Lin Wang
Licensed Content Date	Mar 1, 2012
Licensed Content Volume	1
Licensed Content Issue	2
Licensed Content Pages	7
Type of Use	reuse in a thesis/dissertation
Portion	figures/tables/illustrations
Number of figures/tables/illustrations	1
Format	both print and electronic
Are you the author of this Elsevier article?	No
Will you be translating?	No
Title	Harnessing Direct Current Triboelectricity with Dynamic Schottky Diodes on Silicon
Institution name	Curtin University
Expected presentation date	Jul 2022
Portions	Figure 1
Requestor Location	Mr. Stuart Ferrie U 44 53 LEONARD ST VICTORIA PARK, WA 6100

	Australia Attn: Stuart Ferrie
Publisher Tax ID	GB 494 6272 12
Total	**0.00 USD**

Figure 1.9

License Details

This Agreement between Mr. Stuart Ferrie ("You") and Springer Nature ("Springer Nature") consists of your license details and the t
provided by Springer Nature and Copyright Clearance Center.

License Number	5296831118383
License date	Apr 26, 2022
Licensed Content Publisher	Springer Nature
Licensed Content Publication	Nature Nanotechnology
Licensed Content Title	Direct-current triboelectricity generation by a sliding Schottky nanocontact on MoS2 multilayers
Licensed Content Author	Jun Liu et al
Licensed Content Date	Dec 11, 2017
Type of Use	Thesis/Dissertation
Requestor type	academic/university or research institute
Format	print and electronic
Portion	figures/tables/illustrations
Number of figures/tables/illustrations	1
High-res required	no
Will you be translating?	no
Circulation/distribution	1 - 29
Author of this Springer Nature content	no
Title	Harnessing Direct Current Triboelectricity with Dynamic Schottky Diodes on Silicon
Institution name	Curtin University
Expected presentation date	Jul 2022
Portions	Figure 2
Requestor Location	Mr. Stuart Ferrie U 44 53 LEONARD ST VICTORIA PARK, WA 6100 Australia Attn: Stuart Ferrie

Figure 1.10

1. Materials Horizons

Article: Interfacial friction-induced electronic excitation mechanism for tribo-tunneling current generation

Billing Status: Open

Print License

Order License ID

1217017-1

Order detail status

Completed

ISSN

2051-6347

Type of use

Republish in a thesis/dissertation

Publisher

Royal Society of Chemistry

Portion

Image/photo/illustration

Hide Details

0.00 AUD

Republication Permission

LICENSED CONTENT

Publication Title

Materials Horizons

Article Title

Interfacial friction-induced electronic excitation mechanism for tribo-tunneling current generation

Date

01/01/2014

Language

English

Country

United Kingdom of Great Britain and Northern Ireland

Rightsholder

Royal Society of Chemistry

Publication Type

Journal

Start Page

1020

End Page

1026

Issue

5

Volume

6

REQUEST DETAILS

Portion Type

Image/photo/illustration

Number of images / photos / illustrations

1

Format (select all that apply)

Print, Electronic

Who will republish the content?

Academic institution

Duration of Use

Life of current edition

Lifetime Unit Quantity

Up to 499

Rights Requested

Main product

Distribution

U.K. and Commonwealth (excluding Canada)

Translation

Original language of publication

Copies for the disabled?

No

Minor editing privileges?

No

Incidental promotional use?

No

Currency

AUD

NEW WORK DETAILS

Title

Harnessing Direct Current Triboelectricity with Dynamic Schottky Diodes on Silicon

Instructor name

Simone Ciampi

Institution name

Curtin University of Technology

Expected presentation date

2022-07-01

ADDITIONAL DETAILS

The requesting person / organization to appear on the license

Stuart Ferrie

REUSE CONTENT DETAILS

Title, description or numeric reference of the portion(s)

Fig 4

Editor of portion(s)

Jiang, Keren; Li, Zhi; Liu, Jun; Nguyen, Lan; Thundat, Thomas

Volume of serial or monograph

6

Page or page range of portion

1020-1026

Title of the article/chapter the portion is from

Interfacial friction-induced electronic excitation mechanism for tribo-tunneling current generation

Author of portion(s)

Jiang, Keren; Li, Zhi; Liu, Jun; Nguyen, Lan; Thundat, Thomas

Issue, if republishing an article from a serial

5

Publication date of portion

2019-01-01

Figure 1.11

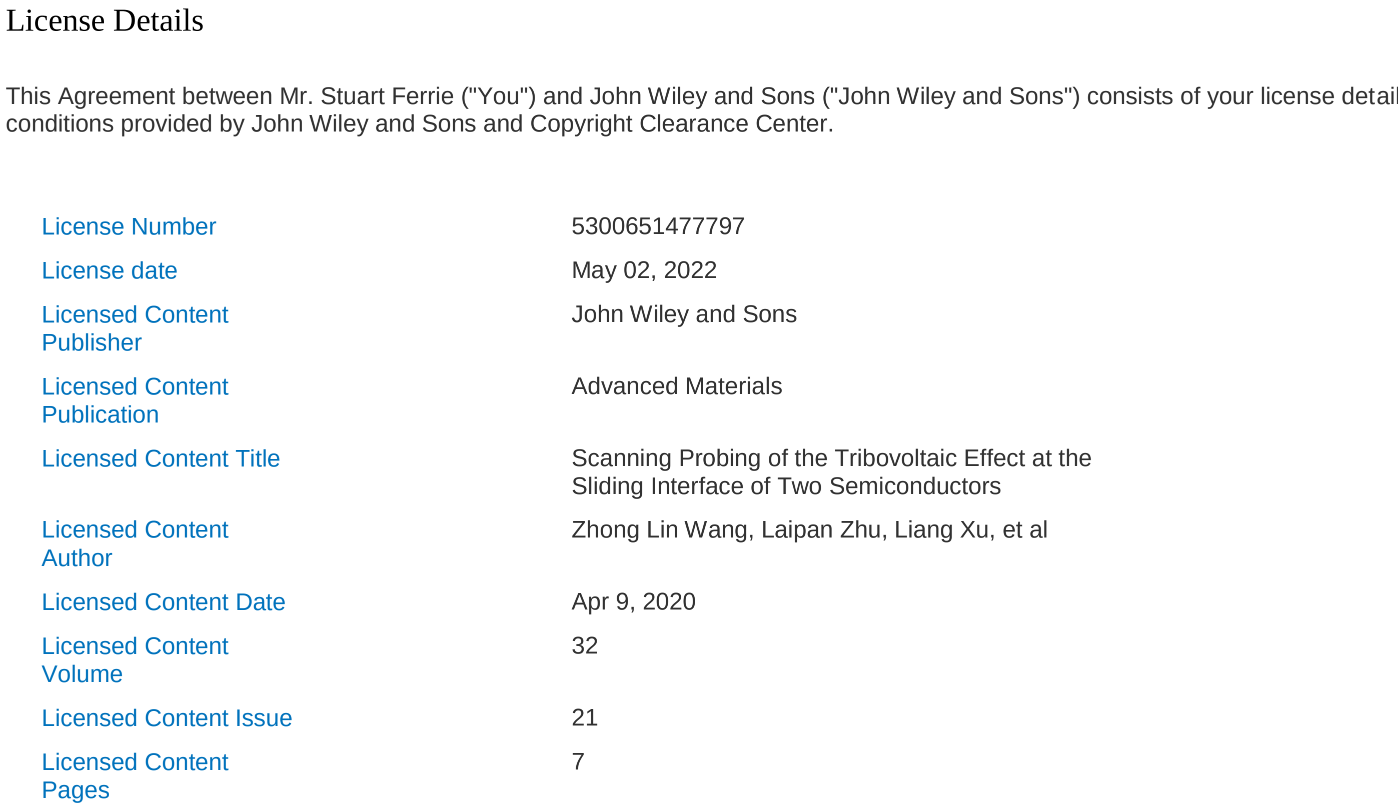

License Details

This Agreement between Mr. Stuart Ferrie ("You") and John Wiley and Sons ("John Wiley and Sons") consists of your license detai conditions provided by John Wiley and Sons and Copyright Clearance Center.

License Number	5300651477797
License date	May 02, 2022
Licensed Content Publisher	John Wiley and Sons
Licensed Content Publication	Advanced Materials
Licensed Content Title	Scanning Probing of the Tribovoltaic Effect at the Sliding Interface of Two Semiconductors
Licensed Content Author	Zhong Lin Wang, Laipan Zhu, Liang Xu, et al
Licensed Content Date	Apr 9, 2020
Licensed Content Volume	32
Licensed Content Issue	21
Licensed Content Pages	7

Type of Use	Dissertation/Thesis
Requestor type	University/Academic
Format	Print and electronic
Portion	Figure/table
Number of figures/tables	1
Will you be translating?	No
Title	Harnessing Direct Current Triboelectricity with Dynamic Schottky Diodes on Silicon
Institution name	Curtin University
Expected presentation date	Jul 2022
Portions	Figure 4
Requestor Location	Mr. Stuart Ferrie U 44 53 LEONARD ST VICTORIA PARK, WA 6100 Australia Attn: Stuart Ferrie
Publisher Tax ID	EU826007151
Total	**0.00 AUD**

Figure 1.12

License Details

This Agreement between Mr. Stuart Ferrie ("You") and Elsevier ("Elsevier") consists of your license details and the terms and condi
Elsevier and Copyright Clearance Center.

License Number	5296830776545
License date	Apr 26, 2022
Licensed Content Publisher	Elsevier
Licensed Content Publication	Nano Energy
Licensed Content Title	The tribovoltaic effect and electron transfer at a liquid-semiconductor interface
Licensed Content Author	Shiquan Lin,Xiangyu Chen,Zhong Lin Wang
Licensed Content Date	Oct 1, 2020
Licensed Content Volume	76
Licensed Content Issue	n/a
Licensed Content Pages	1
Type of Use	reuse in a thesis/dissertation
Portion	figures/tables/illustrations
Number of figures/tables/illustrations	1

Format	both print and electronic
Are you the author of this Elsevier article?	No
Will you be translating?	No
Title	Harnessing Direct Current Triboelectricity with Dynamic Schottky Diodes on Silicon
Institution name	Curtin University
Expected presentation date	Jul 2022
Portions	Figure 1
Requestor Location	Mr. Stuart Ferrie U 44 53 LEONARD ST VICTORIA PARK, WA 6100 Australia Attn: Stuart Ferrie
Publisher Tax ID	GB 494 6272 12
Total	**0.00 USD**

Figure 1.13

Open Access This article is licensed under a Creative Commons Attribution 4.0 International License, which permits use, sharing, adaptation, distribution and reproduction in any medium or format, as long as you give appropriate credit to the original author(s) and the source, provide a link to the Creative Commons license, and indicate if changes were made. The images or other third party material in this article are included in the article's Creative Commons license, unless indicated otherwise in a credit line to the material. If material is not included in the article's Creative Commons license and your intended use is not permitted by statutory regulation or exceeds the permitted use, you will need to obtain permission directly from the copyright holder. To view a copy of this license, visit http://creativecommons.org/licenses/by/4.0/.

Chapter 3

Rights are retained to reuse in a thesis by the authors.

Chapter 4

Rights are retained to reuse in a thesis by the authors.